

An Iwasawa-Taniguchi Effect for Compton-thick Active Galactic Nuclei

Peter G. Boorman,¹[★] Poshak Gandhi,¹ Mislav Baloković,^{2,3} Murray Brightman,² Fiona Harrison,² Claudio Ricci^{4,5,6,7} and Daniel Stern⁸

¹*Department of Physics & Astronomy, Faculty of Physical Sciences and Engineering, University of Southampton, Southampton, SO17 1BJ, UK*

²*Cahill Center for Astronomy and Astrophysics, California Institute of Technology, Pasadena, CA 91125, USA*

³*Harvard-Smithsonian Center for Astrophysics, 60 Garden Street, Cambridge, MA 02138, USA*

⁴*Instituto de Astrofísica, Facultad de Física, Pontificia Universidad Católica de Chile, Casilla 306, Santiago 22, Chile*

⁵*Núcleo de Astronomía de la Facultad de Ingeniería, Universidad Diego Portales, Av. Ejército Libertador 441, Santiago, Chile*

⁶*Kavli Institute for Astronomy and Astrophysics, Peking University, Beijing 100871, China*

⁷*Chinese Academy of Sciences South America Center for Astronomy and China-Chile Joint Center for Astronomy, Camino El Observatorio 1515, Las Condes, Santiago, Chile*

⁸*Jet Propulsion Laboratory, California Institute of Technology, Pasadena, CA 91109, USA*

Accepted 2018 March 29. Received 2018 March 29; in original form 2017 September 28

ABSTRACT

We present the first study of an Iwasawa-Taniguchi/‘X-ray Baldwin’ effect for Compton-thick active galactic nuclei (AGN). We report a statistically significant anti-correlation between the rest-frame equivalent width (EW) of the narrow core of the neutral Fe K α fluorescence emission line, ubiquitously observed in the reflection spectra of obscured AGN, and the mid-infrared 12 μ m continuum luminosity (taken as a proxy for the bolometric AGN luminosity). Our sample consists of 72 Compton-thick AGN selected from pointed and deep-field observations covering a redshift range of $z \sim 0.0014 - 3.7$. We employ a Monte Carlo-based fitting method, which returns a Spearman’s Rank correlation coefficient of $\rho = -0.28 \pm 0.12$, significant to 98.7% confidence. The best fit found is $\log(\text{EW}_{\text{Fe K}\alpha}) \propto -0.08 \pm 0.04 \log(L_{12\mu\text{m}})$, which is consistent with multiple studies of the X-ray Baldwin effect for unobscured and mildly obscured AGN. This is an unexpected result, as the Fe K α line is conventionally thought to originate from the same region as the underlying reflection continuum, which together constitute the reflection spectrum. We discuss the implications this could have if confirmed on larger samples, including a systematic underestimation of the line of sight X-ray obscuring column density and hence the intrinsic luminosities and growth rates for the most luminous AGN.

Key words: galaxies: active, X-rays: galaxies — galaxies: emission lines — infrared: galaxies

1 INTRODUCTION

X-ray continuum emission from active galactic nuclei (AGN) typically takes the form of a broadband powerlaw with a high-energy cut-off around 300 keV (Ballantyne 2014; Malizia et al. 2014), and originates from Comptonization of ultraviolet accretion disc photons in a hot X-ray corona (Haardt & Maraschi 1991, 1993). Line of sight opacity alters this emission via photoelectric absorption and Compton scattering.

If properly accounted for, this can be used to predict the intrinsic spectral energy distribution of an AGN and thus indirectly study the circumnuclear environment of AGN. Many studies have revealed that the vast majority of AGN are intrinsically obscured with hydrogen column densities (N_{H}) greater than the Galactic value (Risaliti et al. 1999; Burlon et al. 2011; Ricci et al. 2015, $N_{\text{H}} \gtrsim 10^{22} \text{ cm}^{-2}$). For $N_{\text{H}} \lesssim 10^{24} \text{ cm}^{-2}$, the intrinsic power law typically dominates over any other spectral features in the X-ray band. As the column increases to $N_{\text{H}} > 1.5 \times 10^{24} \text{ cm}^{-2}$, the obscuring material becomes optically thick in X-rays to Compton

[★] P.G.Boorman@soton.ac.uk

scattering, in the *Compton-thick* regime. Here, the soft X-ray ($E \lesssim 10$ keV) spectrum is depleted and flattened due to the interplay of photoelectric absorption and Compton downscattering. Depending on the orientation, geometry and column of the Compton-thick obscurer, the hard X-ray spectrum ($E \gtrsim 10$ keV) can either be dominated by the direct intrinsic powerlaw component, absorbed along the line of sight (transmission-dominated Compton-thick AGN); or by a Compton-scattered reflection component, from intrinsic flux reprocessed by the obscurer into the line of sight (reflection-dominated Compton-thick AGN).

The geometrical configuration of the X-ray obscuring and reprocessing medium is typically assumed to be roughly axisymmetric but anisotropic (Murphy & Yaqoob 2009; Ikeda et al. 2009; Brightman & Nandra 2011; Baloković et al. 2018). This is analogous to the putative torus in the Unified Model of AGN (Antonucci 1993; Urry & Padovani 1995; Netzer 2015) invoked to explain the infrared and optical emission observed from different classes of AGN as intrinsically a single class observed at different orientation angles. The X-ray obscurer in Compton-thick AGN is what defines the spectral shape of the reprocessed reflection spectrum, which typically features two key components (Lightman & White 1988; Reynolds 1999):

- (i) A narrow Fe $K\alpha$ fluorescence emission line arising from neutral (and hence cold) iron, with a characteristic energy of 6.4 keV in the rest frame of the source. This emission line is typically the most prominent in the X-ray spectra of AGN, due to a combination of the fluorescence yield and relative abundances of the gas located within the torus.
- (ii) An underlying (flat) Compton scattered continuum with a broad ‘Compton hump’ peaking at ~ 30 keV formed from the combination of photoelectric absorption at $E \lesssim 10$ keV and Compton downscattering from higher energies.

Modelling the strength and shape of the neutral Fe $K\alpha$ fluorescence line together with the Compton hump can yield the line of sight obscuring column to a source. This requires an observed X-ray spectrum spanning the Compton hump at ~ 30 keV and the soft X-ray emission $\lesssim 10$ keV, to provide constraints on the continuum and reflection components. However, many previous X-ray observations of AGN have typically been restricted to the $E \lesssim 10$ keV energy region (*Suzaku* XIS, *Chandra*, XMM-*Newton*), completely missing the Compton hump for local sources. This typically means that any attempt to fit AGN X-ray spectra in this energy region with the objective of constraining the line of sight N_H depends heavily on the Fe $K\alpha$ fluorescence line alone, and can be uncertain.

Despite being an indicator of high obscuring columns, the equivalent width (EW) of the narrow core of the neutral Fe $K\alpha$ fluorescence line has been observed to anti-correlate with the underlying intrinsic X-ray continuum luminosity in samples of transmission-dominated AGN. This effect was first reported by Iwasawa & Taniguchi (1993) for a sample of 37 largely unobscured AGN, observed by the *Ginga* satellite. The best fit linear relation derived was of the form $\log(\text{EW}_{\text{Fe } K\alpha}) \propto -0.20 \pm 0.03 \log(L_{2-10\text{keV}})$. This is sometimes referred to as the ‘X-ray Baldwin’ effect due to the similarity with the study by Baldwin (1977) on the anti-correlation between the EW of the C IV 1549 ultraviolet emission line and

AGN continuum. Here we refer to the X-ray Baldwin effect as the ‘Iwasawa-Taniguchi’ effect.

The Iwasawa-Taniguchi effect has been explored in further detail for different AGN classes. For example, Page et al. (2004) reported an Iwasawa-Taniguchi effect of $\log(\text{EW}_{\text{Fe } K\alpha}) \propto -0.17 \pm 0.08 \log(L_{2-10\text{keV}})$ for a sample of 53 type 1 AGN observed by XMM-*Newton*, with the slope being consistent with that of Iwasawa & Taniguchi. However, Jiang et al. (2006) later reported a much shallower anti-correlation of $\log(\text{EW}_{\text{Fe } K\alpha}) \propto -0.10 \pm 0.05 \log(L_{2-10\text{keV}})$ for a sample of 75 radio-quiet AGN observed by XMM-*Newton* and *Chandra*. The authors attribute the reduction in slope of the anti-correlation to radio-loud contamination of previous AGN samples, proposing that radio-loud AGN could have an enhanced continuum contribution from a relativistic jet. The authors further postulated that short-term variability of the primary X-ray source could, in part, contribute to the anti-correlation. Despite the shallower gradient found, two measurements of the same gradient would be expected to differ by the separation between Iwasawa & Taniguchi and Jiang et al. $\sim 8\%$ of the time¹, and are thus not strongly inconsistent with each other. Bianchi et al. (2007) later studied the Iwasawa-Taniguchi effect for a sample of 157 radio-quiet unobscured type 1 AGN, including narrow line Seyfert 1s (which share some spectral characteristics with obscured AGN). In contrast to Jiang et al. (2006), the authors found a somewhat steeper anti-correlation of $\log(\text{EW}_{\text{Fe } K\alpha}) \propto -0.17 \pm 0.03 \log(L_{2-10\text{keV}})$, fully consistent with the original Iwasawa-Taniguchi effect and Page et al. (2004). Bianchi et al. further suggest an additional strong anti-correlation between the Fe $K\alpha$ fluorescence line EW and Eddington ratio. Indeed, Ricci et al. (2013a) tested the positive relation between the photon index and Eddington ratio found for AGN (Lu & Yu 1999; Shemmer et al. 2006; Risaliti et al. 2009; Brightman et al. 2013; Trakhtenbrot et al. 2017), even into the Compton-thick regime (Brightman et al. 2016), finding that this could contribute to the Iwasawa-Taniguchi effect. This is because a lower Eddington ratio (and thus photon index, resulting in a flatter spectrum) would lead to more photons at the energy required to generate iron $K\alpha$ fluorescence, giving a larger EW.

Individual source variability has been shown to considerably affect the strength of the anti-correlation, with Shu et al. (2012) finding a reduction in the observed slope from $\log(\text{EW}_{\text{Fe } K\alpha}) \propto -0.22 \log(L_{2-10\text{keV}})$ to $\log(\text{EW}_{\text{Fe } K\alpha}) \propto -0.13 \log(L_{2-10\text{keV}})$, after accounting for the time-averaged Fe $K\alpha$ strength in a sample of 32 AGN with $N_H \lesssim 10^{23} \text{ cm}^{-2}$, observed multiple times by the *Chandra* high-energy grating (HEG).

The conventional Iwasawa-Taniguchi effect describes the strength of the Fe $K\alpha$ line relative to the intrinsic continuum (readily available for unobscured AGN), but a difficulty is introduced when trying to study the effect for obscured sources, which by definition start to lack a prominent transmitted intrinsic component in the iron line flux, to measure the EW against. Ricci et al. (2014) report a significant detection of the Iwasawa-Taniguchi effect for two separate samples of Seyfert 1s and 2s, consistently of

¹ <https://ned.ipac.caltech.edu/level5/Sept01/0rear/frames.html>

$\log(L_{\text{FeK}\alpha}/L_{10-50\text{keV}}) \propto -0.11 \pm 0.01 \log(L_{10-50\text{keV}})$. Type 2 Seyferts are typically observed to be obscured in the optical and often X-rays also (e.g., Koss et al. 2017). Thus the work of Ricci et al. was the first study into the effect for obscured sources, in which the higher 10 – 50 keV energy range was used to describe the intrinsic continuum and FeK α EW since photoelectric absorption is minimised for photons at harder energies. Interestingly, the authors postulate that the consistency of slopes between Seyfert 1s and 2s could indicate that the physical mechanism responsible for the Iwasawa-Taniguchi effect is unaffected by orientation under Unification schemes. For a breakdown of the results into the Iwasawa-Taniguchi effect from the different works mentioned above, see Table 1 of Ricci et al. (2013b).

Numerous physical scenarios have been considered to explain the observed Iwasawa-Taniguchi effect, with one of the most favoured being an intrinsic luminosity-dependent covering factor of neutral obscuring gas surrounding the AGN. This effect was first suggested in Lawrence & Elvis (1982) & Lawrence (1991), dubbed the ‘receding torus’, and has been observed in various large AGN samples. This idea is strengthened by the results from multiple studies reporting an increased number density of obscured AGN at lower X-ray luminosities (Ueda et al. 2011; Lusso et al. 2013; Merloni et al. 2014; Georgakakis et al. 2017). Simulations of torus reprocessing of X-ray emission have also shown that the FeK α line EW can be dramatically enhanced when the observer is exposed to less intrinsic flux than the reprocessor (Krolik et al. 1994), which is physically attained with higher covering factors of the central engine.

A receding torus model provides a possible explanation for the Iwasawa-Taniguchi effect in which the observed spectrum contains a dominant unscattered component, as is the case for transmission-dominated obscured systems. The prominence of the direct transmitted component would scale with intrinsic luminosity, resulting in the narrow FeK α line (arising from the reflection component) being diminished by the brightened intrinsic power law. To illustrate the contribution to the observed flux from the transmitted component vs. the reflected component from an anisotropic X-ray reprocessor, Figure 1 shows the relative contribution to the total line flux (approximated here to 6 – 7.9 keV) from the transmitted component (blue) and reflected component (red). This was simulated with the `borus02_v170709a` (`borus02`)² model (Baloković et al. 2018), in which the obscurer is spherically distributed with polar cutouts. For each column density, we plot the average flux ratio for a series of covering factor/inclination angle combinations, and sources are predicted to become reflection-dominated in the FeK α line for $\log N_{\text{H}} \gtrsim 23.6 \text{ cm}^{-2}$.

Recent dedicated studies into specific X-ray-obscured AGN appear to show a trend of decreased neutral FeK α line EW, with increasing luminosity. Here we highlight three Compton-thick case studies for comparison; also illustrated in Figure 2:

1. Local low luminosity Compton-thick Seyferts typically show prominent lines. One of the strongest observed FeK α line EWs found to date was for IC 3639 (Boorman et al.

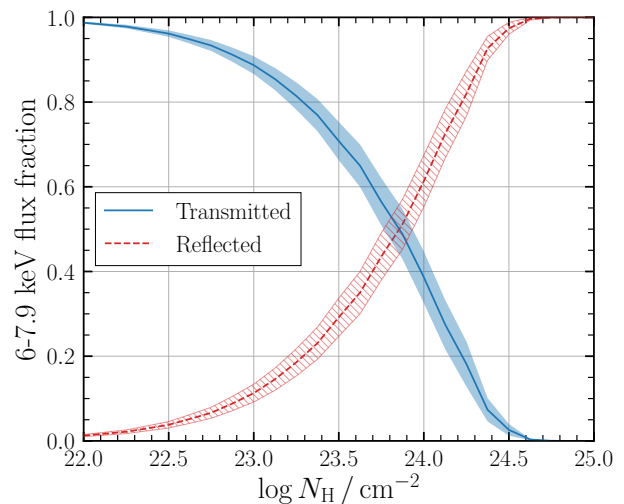


Figure 1. The contribution to the total observed flux in the iron line region (approximated to 6 – 7.9 keV) from the direct transmitted component (blue) and Compton-scattered reflected component (red). This was simulated using the `borus02` X-ray reprocessor model (Baloković et al. 2018), for a spherically distributed obscurer with polar cutouts. For each column density, the average flux ratio for a series of covering factor/inclination angle combinations is plotted with the confidence region showing the range between the minimum and maximum found around the average.

2016); a reflection-dominated Compton-thick AGN with infrared bolometric luminosity (in the 8 – 1000 μm wavelength range) of $\log(L_{8-1000\mu\text{m}}[L_{\odot}]) \sim 10.9$ and $\text{EW}_{\text{FeK}\alpha} \sim 3 \text{ keV}$, relative to the observed underlying reflection continuum.

2. On the other hand, NGC 7674 (Gandhi et al. 2017) is a heavily Compton-thick Seyfert 2, with a higher infrared bolometric luminosity of $\log(L_{8-1000\mu\text{m}}[L_{\odot}]) \sim 11.6$. Yet the source has an observed EW of the neutral line of $\text{EW}_{\text{FeK}\alpha} \sim 0.4 \text{ keV}$: the lowest constrained EW of the FeK α line detected for any bona-fide Compton-thick AGN to date.

3. At the highest luminosities, Gilli et al. (2011, 2014, LESS J033229.4-275619) is the most distant ($z \sim 4.75$) Compton-thick AGN classified to date, with infrared bolometric luminosity $\log(L_{8-1000\mu\text{m}}[L_{\odot}]) \sim 12.8$. Interestingly, the neutral FeK α fluorescence line is not detected in the observed X-ray spectrum obtained from the 4Ms *Chandra* Deep Field South observation, yet with a prominent ionised Hydrogen-like iron line at $\sim 6.9 \text{ keV}$ to $\sim 2\sigma$ confidence, with rest-frame $\text{EW} = 2.8^{+1.7}_{-1.4} \text{ keV}$. In fact, there is increasing observational evidence for prominent ionised iron lines in luminous infrared galaxies (LIRGs: $\log(L_{8-1000\mu\text{m}}[L_{\odot}]) > 11$) (Iwasawa et al. 2009).

We note that although the contribution to the infrared flux from star formation will increase with bolometric flux, the AGN contribution also increases. This means a higher infrared flux should indicate a more intrinsically luminous AGN. These three case study sources are illustrated in Figure 2, in which we plot the data/model ratio for each source after fitting a powerlaw to the observed spectrum. Although NGC 7674 appears to show a large component to the observed flux around 6 – 6.5 keV, the narrow core of the neu-

² available at <http://www.astro.caltech.edu/~mislavb/download/index.html>

tral Fe $K\alpha$ line is considerably weaker. The panels have been binned for clarity.

This paper presents the first study into an Iwasawa-Taniguchi effect for Compton-thick AGN, with Fe $K\alpha$ EWs measured relative to the observed continuum vs. rest-frame mid-infrared $12\mu\text{m}$ luminosity ($L_{12\mu\text{m}}$; taken as a proxy for the intrinsic AGN bolometric luminosity). The cosmology adopted for computing luminosity distances is $H_0 = 67.3\text{ km s}^{-1}\text{ Mpc}^{-1}$, $\Omega_\Lambda = 0.685$ and $\Omega_M = 0.315$ (Planck Collaboration 2014)³ The paper is organised as follows: Section 2 describes our source selection and the sample used in our statistical analysis. Section 3 then describes our method for clarifying candidate Compton-thick AGN, as well as for determining the $L_{12\mu\text{m}}$ and Fe $K\alpha$ EW values. We then discuss our fitting procedure. Section 4 comprises our main results, followed by the discussion and implications of the effect if confirmed on future larger Compton-thick AGN samples, in Section 5. We summarise our findings in Section 6.

2 THE SAMPLE

Our primary goal whilst collating Compton-thick candidates from the literature was to cover a broad redshift (and hence luminosity) range. Furthermore, X-ray spectra encompassing the observed frame neutral Fe $K\alpha$ fluorescence line, seen at $6.4/(1+z)\text{ keV}$ in the rest-frame, were required. In order to robustly quantify the EW required a detection of the underlying observed continuum, neighbouring the line centroid. Below we include details of the high and low redshift sub-samples we include in our work.

2.1 High redshift

For higher redshift (or fainter) sources, *Chandra* observations were ideal due to low background and optimal sensitivities in the $0.5\text{--}8.0\text{ keV}$ energy range. At high redshift, the k-corrected Compton hump also shifts to the observed *Chandra* energy range. A considerable contribution to our sample thus includes the Brightman et al. (2014) compilation of Compton-thick AGN candidates collated from archival deep *Chandra* surveys. The original sample includes ~ 100 Compton-thick candidates. A source was only retained for our study if it met the following criteria:

- (i) > 50 total X-ray counts detected in the *Chandra* energy band.
- (ii) A spectroscopic redshift.
- (iii) A line of sight column density of $N_H \geq 1.5 \times 10^{24}\text{ cm}^{-2}$ at 90% confidence, determined by Brightman et al. (2014).
- (iv) Infrared detection by the *Wide-field Infrared Survey Explorer* (WISE)⁴ or *Spitzer Space Telescope* to enable a reliable $L_{12\mu\text{m}}$ estimate.

³ Redshift-dependent distances are used for consistency across the full sample. Only a handful of the closest AGN have redshift-independent distances which scatter around our adopted luminosity distances.

⁴ A ‘reliable’ WISE detection corresponds to a detection with $S/N > 5$. See http://wise2.ipac.caltech.edu/docs/release/allsky/expsup/sec5_3.html for further details.

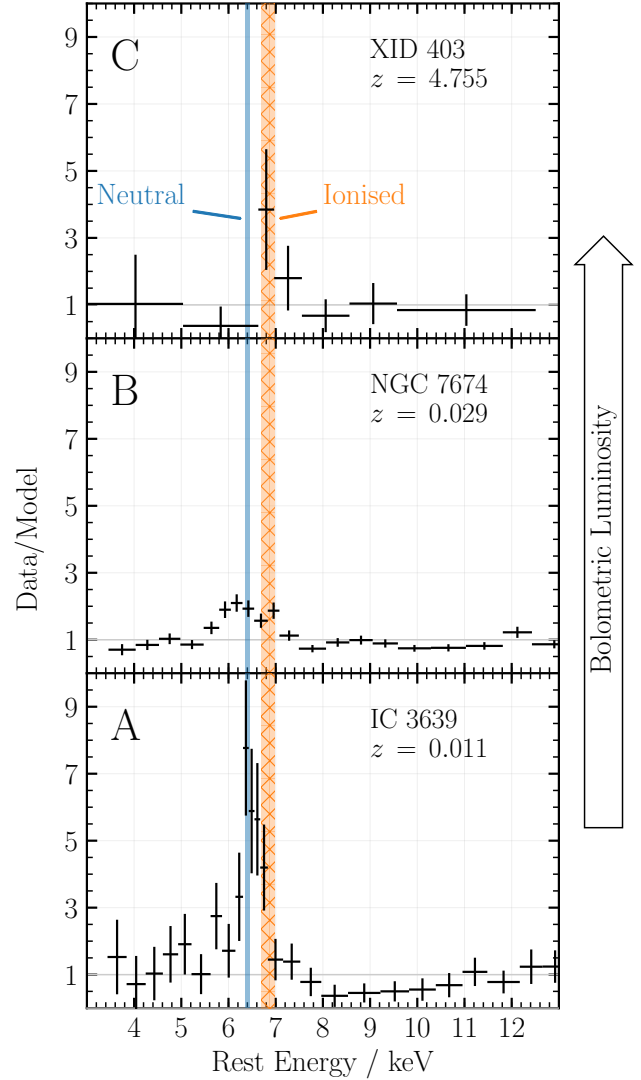


Figure 2. Three Compton-thick case studies illustrating the motivation for the studying a Compton-thick Iwasawa-Taniguchi effect. Panel A: IC 3639 (Boorman et al. 2016): a local Compton-thick AGN at $z = 0.011$ with bolometric infrared luminosity, $\log(L_{8-1000\mu\text{m}}[L_\odot]) \sim 10.9$, and one of the strongest neutral Fe $K\alpha$ lines reported in the literature. Panel B: NGC 7674 (Gandhi et al. 2017): a local Compton-thick AGN, and luminous infrared galaxy with bolometric infrared luminosity, $\log(L_{8-1000\mu\text{m}}[L_\odot]) \sim 11.6$. Contrastingly, this source has the lowest neutral Fe $K\alpha$ EW reported for local Compton-thick AGN. Furthermore, the spectrum clearly shows a contribution to the residuals in the ionised energy region. Panel C: LESS J033229.4-275619 (Gilli et al. 2014): the highest redshift Compton-thick AGN currently known, with $\log(L_{8-1000\mu\text{m}}[L_\odot]) \sim 12.8$. The spectrum plotted is from a 7 Ms observation of *Chandra* Deep Field South (CDFS). The neutral emission is not detected, yet a considerable flux contribution can be seen in the ionised emission line energy region. Each source was fitted with a redshifted powerlaw in *xspec*, and the resulting data/model ratio is shown. For all panels, the narrow core of the neutral line is shown with the orange region for $E = 6.35 - 6.45\text{ keV}$, and the ionised line region is shown in blue hatch for the $E = 6.69 - 6.98\text{ keV}$ region (to encompass the 6.7 and 6.97 keV ionised lines).

Of the resulting candidates, a further two were excluded due to a disagreement with our Compton-thick classification (COSMOS 0661 & COSMOS 1517: Section 3), leaving a total of 27 sources from Brightman et al. (2014). An additional five high redshift sources come from further Compton-thick studies by Feruglio et al. (2011); Corral et al. (2016, BzK 4892), Georgantopoulos et al. (2013, XMMID 324), Lanzuisi et al. (2015, XMMID 2608, XMMID 60152) and Hlavacek-Larrondo et al. (2017, IRAS F15307+3252). In total, 32 sources make up our high redshift subsample of Compton-thick candidates.

2.2 Low redshift

A major contribution to our low redshift subsample comes from Ricci et al. (2015). The sample consists of 55 Compton-thick AGN candidates selected from the *Neil Gehrels Swift*/Burst Alert Telescope (BAT) 70-month catalogue, all within the local Universe (average $z = 0.055$). Of these 55, we rejected 19 sources without publicly available *NuSTAR* observations. *NuSTAR* (Harrison et al. 2013) is the first true hard X-ray imaging instrument in the 3 – 79 keV energy range, encompassing the full underlying reflection continuum for low redshift AGN, and thus ideal for studying Compton-thick candidates. By combining with soft X-ray observations, many works have constrained the N_{H} values for numerous obscured, Compton-thick and changing-look AGN to date (e.g. Arévalo et al. 2014, Circinus Galaxy; Baloković et al. 2014, NGC 424, NGC 1320, IC 2560; Gandhi et al. 2014, Mrk 34; Teng et al. 2014, Mrk 231; Annuar et al. 2015, NGC 5643; Bauer et al. 2015, NGC 1068; Ptak et al. 2015, Arp 299; Boorman et al. 2016, IC 3639; Megamaser sample; Masini et al. 2016b, Mrk 1210; Ricci et al. 2016, IC 751; Ricci et al. 2017, WISE J1036 +0449; Annuar et al. 2017, NGC 1448; Gandhi et al. 2017, NGC 7674), hence our preference for *NuSTAR* availability.

An additional three sources from the Ricci et al. (2015) sample were excluded due to a disagreement with our mid-infrared diagnostic Compton-thick classification (2MASX J09235371-3141305; MCG -02-12-017; NGC 6232, Section 3).

The last contribution to our low redshift subsample comes from the Gandhi et al. (2014) compilation of bona-fide Compton-thick AGN, updated to include IC 3639 (Boorman et al. 2016), NGC 1448 (Annuar et al. 2017) and NGC 7674 (Gandhi et al. 2017), whilst excluding changing-look candidates: Mrk 3 (Ricci et al. 2015, find a Compton-thin column density to 90% confidence), NGC 4102, NGC 4939⁵, NGC 4785 (Gandhi et al. 2015a; Marchesi et al. 2017) and NGC 7582 (Rivers et al. 2015). In total, 40 sources make up our low redshift subsample of Compton-thick candidates. Full details of the 72 (low + high redshift) Compton-thick candidates in our sample are included in Table 1.

⁵ Our own analysis of the archival XMM-Newton EPIC/PN spectrum as compared to the more recent *NuSTAR* FPMA & FPMB spectra strongly indicate a changing-look AGN for these sources.

3 METHOD

3.1 Infrared luminosities

In selecting a suitable proxy for the bolometric luminosity of each source, we adhered to the following criteria: (1) the bolometric luminosity could not be derived from the spectral energy region responsible for the neutral Fe K α line nor from the continuum surrounding the line that would be used to derive an EW, and (2) the proxy should be prominent and well detected for Compton-thick AGN.

We used the infrared contribution to the broadband spectra of our AGN sample, which is considered to have sizeable contributions in this wavelength range due to reprocessing of the primary intrinsic AGN emission. Since typical AGN contributions to composite galaxy spectra dominate at $\sim 6 - 20 \mu\text{m}$ (Mullaney et al. 2011), we used the rest-frame $12 \mu\text{m}$ luminosity of each source.

To determine the rest-frame $12 \mu\text{m}$ luminosity, we utilised the infrared spectral template of Mullaney et al. (2011) to interpolate the rest-frame $12 \mu\text{m}$ flux from *observed-frame* flux measurements as close to $12 \mu\text{m}$ as possible. For high-quality infrared observations, we use the *WISE* and *Spitzer* Multiband Imaging Photometer (MIPS). *WISE* had four imaging channels onboard (W1, W2, W3 & W4) corresponding to $\lambda = 3.35 \mu\text{m}$, $4.60 \mu\text{m}$, $11.56 \mu\text{m}$, $22.09 \mu\text{m}$, respectively (Wright et al. 2010), whereas *Spitzer*/MIPS was capable of imaging in spectral bands centered on $\lambda = 24 \mu\text{m}$, $70 \mu\text{m}$, $160 \mu\text{m}$. For $z \lesssim 0.84$ a robust interpolation could be made from W3 and W4 observations. However, for higher redshift sources in which the k-correction shifts the rest-frame $12 \mu\text{m}$ luminosity to wavelengths beyond W4 (or for poorly constrained/faint observations from *WISE*), we use *Spitzer*/MIPS.

For archival *WISE* observations, we use the AllWISE Source Catalog⁶ to get profile-fitted magnitudes and the NASA Extragalactic Database (NED)⁷ to search for archival *Spitzer*/MIPS observations.

To test how representative the Mullaney et al. (2011) template was for predicting the $12 \mu\text{m}$ luminosity for the AGN in our sample with $L_{2-10\text{keV}} < 10^{42} \text{erg s}^{-1}$ or $L_{2-10\text{keV}} > 10^{44} \text{erg s}^{-1}$, we compared the interpolated luminosities with those predicted from the type 2 AGN template from Polletta et al. (2007), which were derived over a wider range of luminosities. On average, the offset between the interpolated luminosities from the two templates was only ~ 0.06 dex.

3.2 Compton-thick confirmation of sample

Strong correlations between mid-infrared and intrinsic X-ray emission have been found with ground-based high angular resolution observations of AGN, around $12 \mu\text{m}$ (Horst et al. 2008; Levenson et al. 2009; Gandhi et al. 2009; Asmus et al. 2015). A similar correlation has been found as a function of large aperture $6 \mu\text{m}$ luminosity, with akin results (Lutz et al. 2004; Mateos et al. 2015; Stern 2015; Chen et al. 2017), and at $5.8 \mu\text{m}$ (Lanzuisi et al. 2009). The $12 \mu\text{m}$ luminosity correlation has been used with considerable success

⁶ <http://irsa.ipac.caltech.edu/cgi-bin/Gator/nph-dd>

⁷ <http://ned.ipac.caltech.edu>

for identifying candidate Compton-thick AGN. Correcting X-ray absorption in Compton-thick sources acts to increase the observed X-ray luminosity to values consistent with the relation. We refer the reader to [Boorman et al. \(2016\)](#) for the effects of absorption correction on X-ray luminosities relative to their observed mid-infrared luminosities for the [Gandhi et al. \(2014\)](#) compilation of bona fide Compton-thick AGN. Here we use the study of the X-ray vs. $12\,\mu\text{m}$ correlation reported in [Asmus et al. \(2015\)](#) to classify our sample as candidate Compton-thick.

The rest-frame observed (i.e. absorbed) $2-10\,\text{keV}$ luminosity was computed from a fit to the available X-ray spectra within `xspec` (for objects without a reported observed X-ray flux), and plotted against the rest-frame $12\,\mu\text{m}$ luminosity, interpolated from the [Mullaney et al. \(2011\)](#) AGN spectral template. These observed fluxes are plotted in Figure 3 (grey points), with a 30% and 15% uncertainty on the X-ray and $12\,\mu\text{m}$ luminosities, respectively. The original correlation found by [Asmus et al. \(2015\)](#) is shown with a solid (green) line for clarity, together with the $1-\sigma$ scatter. On average, the sample displays a mean ratio of observed X-ray to mid-infrared flux of -2.0 ± 0.7 dex, and this is shown over plotted with a dashed (grey) line and shading. An average deviation of greater than two orders of magnitude from the relation is indicative of Compton-thick levels of obscuration found in previous works. However, from this relation, 2MASX J09235371-3141305, MCG -02-12-017, NGC 6232, COSMOS 0661 and COSMOS 1517 displayed mid-infrared fluxes that agreed with the observed X-ray flux within the uncertainties found by [Asmus et al. \(2015\)](#). This could suggest that the observed X-ray flux has a major contribution from the transmitted component, i.e. is only partially obscured and thus were excluded from our Compton-thick sample.

3.2.1 Star Formation Contamination of $L_{12\mu\text{m}}$

To test for infrared star formation contamination, we first used the $12\,\mu\text{m}$ observations from [Asmus et al. \(2014\)](#). This work minimised star-formation contamination in measuring mid-infrared fluxes of local sources by using high-angular resolution ($\lesssim 0''.4$) imaging with ground-based 8m class telescopes. Such contamination would not be excluded from *WISE*-based measurements, that were used in our sample for these sources, due to the larger angular resolution (FWHM) of $6''.1$, $6''.4$, $6''.5$ and $12''.0$ for W1, W2, W3 and W4, respectively. 16 of our sample of 72 sources have measured fluxes in [Asmus et al. \(2014\)](#). The average X-ray to mid-infrared flux ratio for these 16 sources was consistent with the equivalent ratio for the full sample. To fully account for this in the remainder of our sample without high angular resolution measurements, we conservatively use the average change in flux between *WISE* and [Asmus et al. \(2014\)](#) (0.29 dex) added in quadrature to the original 15% uncertainty assigned to the template interpolated flux as the lower error bar for all sources lacking a mid-infrared observation from [Asmus et al. \(2014\)](#), giving 0.30 dex. For the 16 sources with measured fluxes from [Asmus et al.](#), we use the quoted rest-frame $12\,\mu\text{m}$ luminosities and uncertainties therein.

3.3 Rest-frame Fe K α line EWs

Due to the complexity associated with NGC 1068 ([Bauer et al. 2015](#)), NGC 4945 ([Puccetti et al. 2014](#)) and the Circinus Galaxy ([Arévalo et al. 2014](#)), our simplified phenomenological model could not provide a reasonable description of the data for these sources. For this reason, we use the EWs quoted in [Ricci et al. \(2015\)](#), converted to the rest-frame for the corresponding sources. Additionally, we did not have access to the spectral files for 4 high-redshift sources. The source of the EWs we use for our analysis are included in Table 1, column (12). In total, we computed the rest-frame neutral Fe K α fluorescence line EW for 65/72 sources, as follows:

(i) Any counts with $E < 3\,\text{keV}$ in the source rest-frame were ignored for *Chandra* (or $E < 4\,\text{keV}$ for *NuSTAR*) observations, in order to remove as much soft X-ray contamination from non-primary AGN sources as possible. Such sources include intrinsic AGN emission scattered into the line of sight, a relativistic jet, X-ray binaries present in the host or photoionised gas. Furthermore, all counts above $7\,\text{keV}$ in the observed frame were excluded to account for the instrument-based sensitivities of *Chandra*. The corresponding upper limit for *NuSTAR* was $\sim 14-15\,\text{keV}$ in the observed frame, optimising the measurement of the continuum over the most sensitive *NuSTAR* energy range.

(ii) In the low counts regime, we used Cash-statistics ([Cash 1979](#), C-stat) during fitting. Spectra were either grouped to allow a minimum number of counts, or a minimum signal-to-noise (S/N) ratio per bin, while retaining enough spectral resolution for the Fe K α line. We generally favoured fitting with C-stat unless sources had enough counts or high enough S/N to warrant the use of χ^2 statistics on a correspondingly S/N-binned spectrum. We experimented with different binning strategies within the sources fitted with C-stat, and found consistent outcomes.

(iii) Next we fitted each spectrum with a simplified phenomenological model consisting of photoelectric absorption acting on a composite power law plus a narrow Gaussian of $\text{FWHM} \approx 2\,\text{eV}$ ($\sigma = 1\,\text{eV}$), modelling the observed continuum plus the narrow core of the Fe K α fluorescence line. This model was used only to constrain the shape of the observed spectrum, and the EW of the Fe K α line. If a given source had an observed excess of emission in the softer energy band ($E \lesssim 4\,\text{keV}$) an `apex` component was additionally included in the model to account for this. In `xspec`, this baseline model takes the form:

$$\begin{aligned} \text{MODEL} = & \text{GAL_PHABS} \times (\text{APEX} + \\ & \text{ZPHABS} \times (\text{ZPOWERLAW}[\Gamma = 1.4] + \\ & \text{ZGAUSS}[E_L = 6.4\,\text{keV}])) \end{aligned} \quad (1)$$

`GAL_PHABS` refers to an additional minor contribution to the absorption from the Galaxy. Items in square brackets refer to fixed parameters. Although many studies suggest the intrinsic power law of AGN have average photon indices of ~ 1.9 , we fit the spectra with a flatter (lower) photon index of 1.4, as this is closer to the value found for the flat ($< 10\,\text{keV}$) reflection spectra typically observed for Compton-thick AGN, and we required our model to provide a reasonable fit to the observed spectrum.

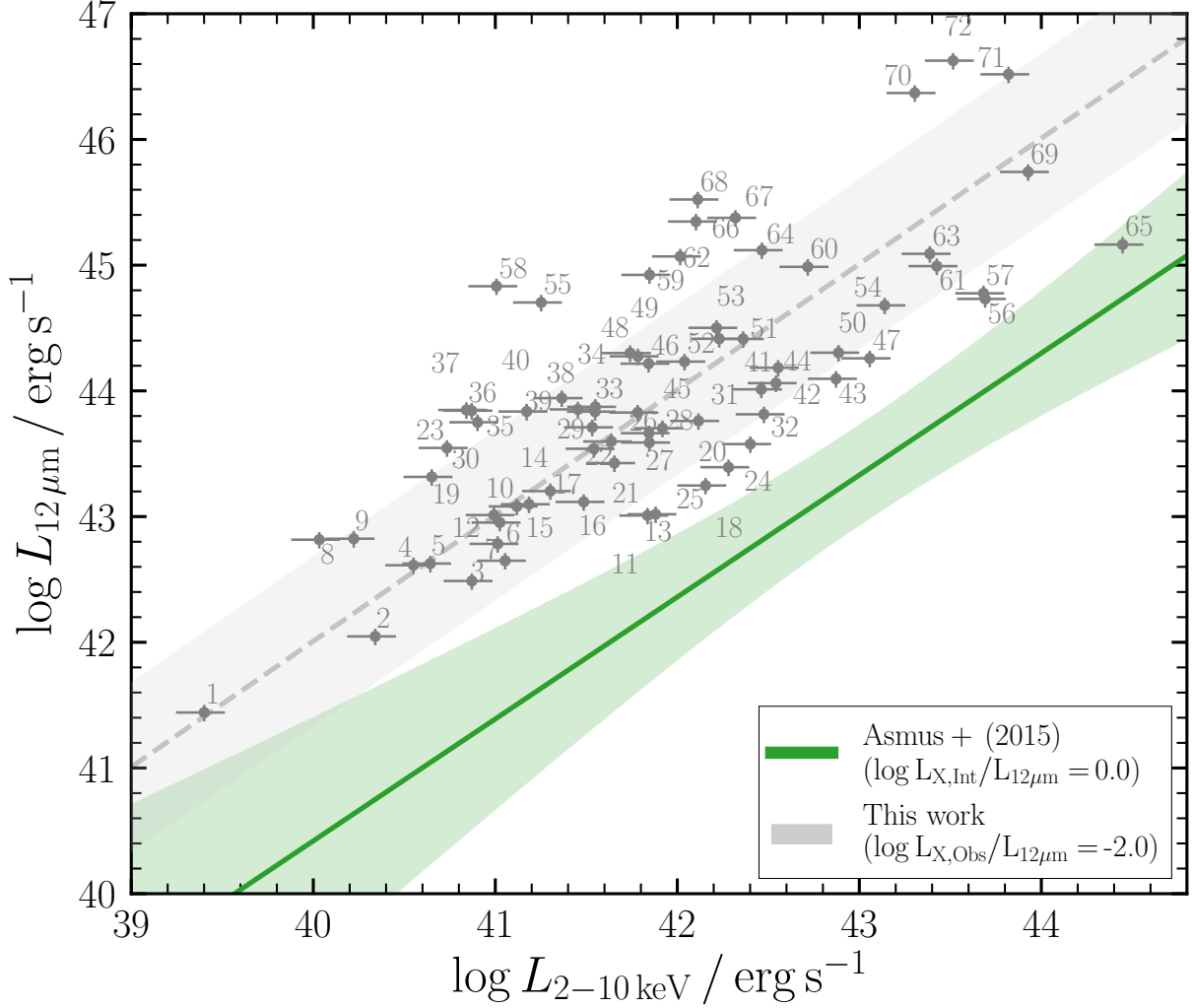


Figure 3. Predicted rest-frame $12\mu\text{m}$ source luminosity (interpolated from the Mullaney et al. (2011) infrared AGN spectral template) vs. the rest-frame observed $2-10\text{keV}$ luminosity of our sample of Compton-thick AGN. The solid (green) line is the best fit correlation from Asmus et al. (2015), together with the $1-\sigma$ scatter in light green shading. All sources were assigned a 30% and 15% uncertainty to the X-ray and $12\mu\text{m}$ luminosities, respectively. The sample shows diminished X-ray emission relative to $12\mu\text{m}$ emission by a factor of greater than 2 orders of magnitude on average, indicative of Compton-thick obscuration. The average observed correlation is shown with a grey dotted line and shaded standard deviation. Labels refer to the ID column in Table 1.

(iv) We then computed two-dimensional confidence contours over the ZPOWERLAW and ZGAUSSIAN model component normalisations (whilst leaving N_{H} and, if required to describe the soft region of the observed spectrum, the *apex* normalisation, free).

(v) These contours were translated to confidence on the Fe $K\alpha$ EW, and plotted as a function of the statistical test difference from the best fit acquired (chi-squared or Cash-statistics depending on the source). This enables us to determine the minimum, and hence presumed best fit rest-frame EW, together with the $1-\sigma$ uncertainty. Irrespective of using chi-squared or Cash-statistic, we use a delta statistic of

+2.30 to represent the $1-\sigma$ (68%) confidence level for two interesting parameters⁸.

(vi) For sources in which the normalisation of the Fe $K\alpha$ line could not be constrained in the fit, we use the limit derived by *xspect* on this parameter to calculate an upper bound on the EW. For any sources that yielded an unphysical EW $> 5\text{keV}$, we set the limit to this value. This is applicable to 3 sources: CDFS 443, CDFS 454 & COSMOS 2180, with EW $\lesssim 12\text{keV}$, EW $\lesssim 48\text{keV}$ and EW $\lesssim 11\text{keV}$, respectively. We defer the reader to the Appendix for the grouped spectrum used for each source.

⁸ <https://heasarc.gsfc.nasa.gov/xanadu/xspec/manual/XSappendixStatistics.html>

3.4 Fitting procedure

Our final sample consists of 72 sources, including 18 upper limits on the EW. All sources without quoted luminosities in [Asmus et al. \(2014\)](#) were assigned the same lower uncertainty of 0.3 dex on $12\,\mu\text{m}$ luminosity specified in Section 3.2. We then fitted a linear regression to the EW vs. rest-frame $12\,\mu\text{m}$ luminosity. To account for all the uncertainties present in our sample whilst determining a fit, our fitting procedure was as follows⁹:

(i) The dataset was bootstrapped by randomly sampling data points from the original whilst allowing repeats. The new dataset was the same size as the parent sample.

(ii) Each point in the bootstrapped dataset was randomly resampled depending on the uncertainty of each point, as follows:

(a) *Non-detections/upper limits*: new points were randomly drawn from a uniform distribution in the interval $[\log 100\,\text{eV}, \log \text{limit} [\text{eV}]]$,

(b) *Detections*: A new value was generated from a Gaussian distribution with standard deviation given by the $1\text{-}\sigma$ error being considered for that point.

To avoid strongly unphysical values from biasing the simulations, we truncated the randomised EWs to between 100 eV and 5 keV.

(iii) A linear least-squares regression was carried out on the Monte Carlo simulated dataset using the `scipy.linregress` Python package. The Spearman's Rank Correlation Coefficient (ρ) was then found using the `scipy.spearmanr` package for each fit.

(iv) Steps (i) – (iii) were repeated in order to obtain a distribution of gradients, y-intercepts and ρ values for the original dataset.

4 RESULTS

Table 1 includes details of each source used in our final sample, and the Appendix contains the best fit spectrum and EW contour for each source used, as well as the sources ruled out in our analysis. After carrying out 20,000 iterations, we obtain a best fit linear regression to the data of:

$$\begin{aligned} \log(\text{EW}_{\text{Fe K}\alpha}/\text{keV}) = \\ -(0.08 \pm 0.04) \log(L_{12\,\mu\text{m}}/10^{44} \text{ erg s}^{-1}) + 2.87 \pm 0.05 \end{aligned} \quad (2)$$

Figure 4 shows all rest-frame $12\,\mu\text{m}$ luminosities vs. rest-frame neutral Fe K α fluorescence line EWs. Blue arrows represent upper limits. As a comparison to previous studies into the Iwasawa-Taniguchi effect, we further include the gradients of previous works: [Iwasawa & Taniguchi \(1993\)](#), [Page et al. \(2004\)](#), [Bianchi et al. \(2007\)](#) and [Ricci et al. \(2014\)](#), normalised to the same y-intercept at $10^{44} \text{ erg s}^{-1}$. We make this normalisation since the EWs we report for our sample are measured relative to the observed spectrum, which for Compton-thick obscuration is drastically different to the observed spectrum for unobscured AGN, not to mention our

proxy for the bolometric luminosity is different to that previously used by other studies.

To test the significance of the fit, we computed the Spearman's Rank Correlation Coefficient (ρ) of the correlation for our sample, excluding upper limits. Upper limits were excluded since ρ tests the strength of a monotonic relationship between variables, which can be dramatically effected by the large range of values/orders of variables attainable with the inclusion of limits in our Monte-Carlo based fitting method. This left 54 sources, and gave a value of $\rho = -0.28 \pm 0.12$. Figure 5 shows the corresponding distribution in ρ found, indicating a negative correlation to 98.7% confidence.

Our best fit gradient is fully consistent with [Ricci et al. \(2014\)](#) within $1\text{-}\sigma$ errors, who attempted to take into account time-averaging of the spectra for determining EWs - see Section 5 for further discussion on this result. The gradient found here is also flatter than the [Bianchi et al. \(2007\)](#) best fit gradient, but consistent within 90% confidence. We include the distributions of our best linear fit gradients and y-intercepts in Figures 6a and 6b, respectively for the 20,000 iterations (including upper limits).

⁹ Similar in method to [Bianchi et al. \(2007\)](#)

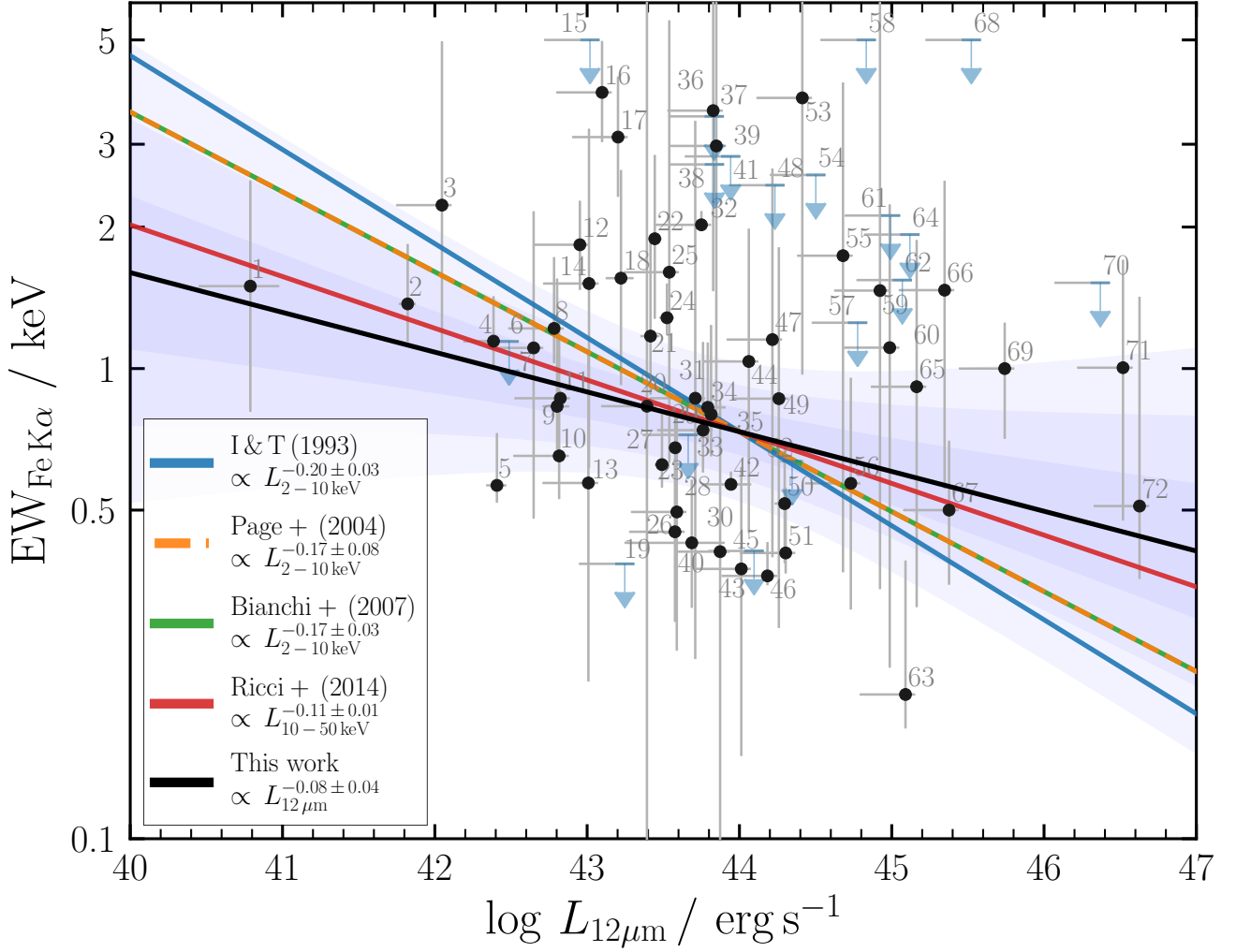


Figure 4. Plot of $L_{12\mu\text{m}}$ vs. (rest-frame) neutral FeK α fluorescence line EWs. Blue arrows represent upper limits. As a comparison to previous studies into the Iwasawa-Taniguchi effect, we further include the gradients of previous works [Iwasawa & Taniguchi \(1993, I & T \(1993\)\)](#), [Page et al. \(2004, Page+ \(2004\)\)](#), [Bianchi et al. \(2007, Bianchi+ \(2007\)\)](#) and [Ricci et al. \(2014, Ricci+ \(2014\)\)](#). These correlations have all been renormalised to match our best fit y-intercept at $10^{44}\text{ erg s}^{-1}$ for comparison, since we are using the 12 μ m luminosity, which is different from the intrinsic luminosity proxies used by other Iwasawa-Taniguchi effect studies. The blue shaded region represents the standard deviation from the mean of our best fit, with lighter shading corresponding to incrementally lower numbers of standard deviation.

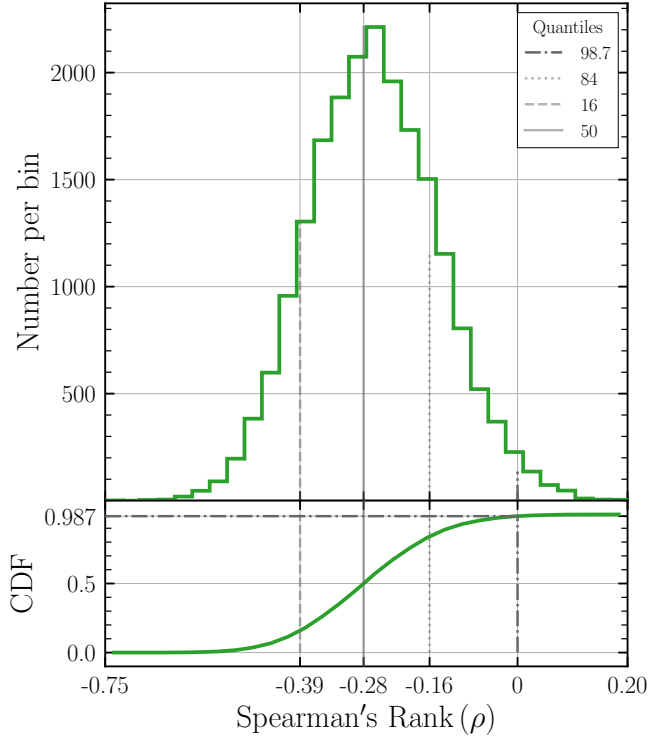


Figure 5. Distribution of Spearman's Rank Correlation Coefficients (ρ) generated from 20,000 iterations of steps (1) - (3) of our fitting procedure, outlined in Section 3.4, for a dataset excluding all upper limits (54 in total). The 16th, 50th and 84th quantiles are shown with dashed, solid and dotted lines, respectively. The dotted (purple) line additionally shows the correlation to be negative to 98.7% confidence.

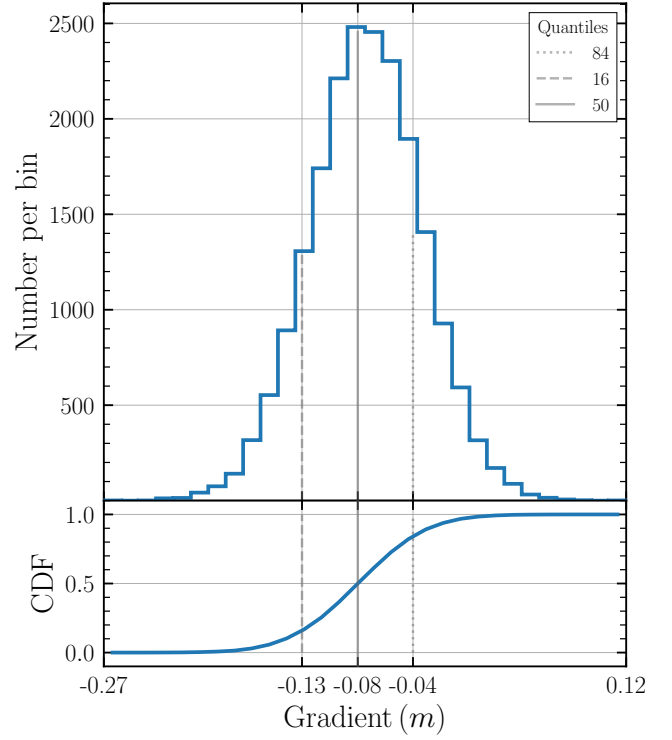


Figure 6a. Distribution of linear regression gradients generated from 20,000 iterations of steps (1) - (3) of our fitting procedure (Section 3.4). The 16th, 50th and 84th quantiles are shown with dashed, solid and dotted lines, respectively.

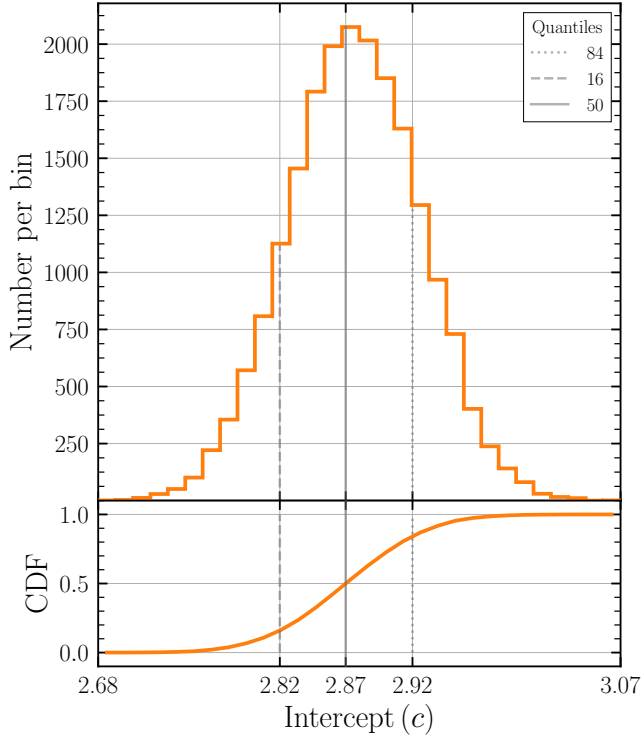


Figure 6b. Distribution of linear regression y-intercepts generated from 20,000 iterations of steps (1) - (3) of our fitting procedure, outlined in Section 3.4. The 16th, 50th and 84th quantiles are shown with the same line styles as in Figure 6a.

ID (1)	Identifier (2)	z (3)	RA (4)	DEC (5)	source ref. (6)	$\log L_{2-10\text{keV}}^{\text{obs}}$ (7)	$\log L_{12\mu\text{m}}$ (8)	EW (9)	+EW (10)	-EW (11)	EW ref. (12)
1	NGC 5194	0.002	202.4696	47.1953	Gou12	39.4	40.8	1.50	1.01	0.69	Bool18
2	ESO 005-G004	0.006	91.4233	-86.6319	Ric15	40.6	41.8	1.37	0.47	0.23	Bool18
3	NGC 1448	0.004	56.1329	-44.6447	Ann17	40.3	42.0	2.23	2.73	1.13	Bool18
4	NGC 5643	0.004	218.1696	-44.1744	Ric15	40.6	42.4	1.14	0.28	0.13	Bool18
5	NGC 5728	0.009	220.5996	-17.2531	Ric15	41.5	42.4	0.56	0.16	0.05	Bool18
6	CDFS 345	0.123	53.1028	-27.9120	Bri14	40.9	42.5	1.14	0	-1	Bool18
7	NGC 4180	0.007	183.2627	7.0388	Ric15	41.1	42.6	1.11	1.05	0.63	Bool18
8	ESO 137-G034	0.009	248.8088	-58.0800	Ric15	41.0	42.8	1.22	0.51	0.19	Bool18
9	NGC 3393	0.012	162.0975	-25.1619	Ric15	41.1	42.8	0.83	0.72	0.16	Bool18
10	NGC 3079	0.004	150.4908	55.6797	Ric15	40.0	42.8	0.65	0.61	0.12	Bool18
11	NGC 4945	0.002	196.3646	-49.4683	Ric15	40.2	42.8	0.86	0.03	0.03	Ric15
12	NGC 2273	0.006	102.5358	60.8458	Mas16	41.0	43.0	1.83	0.44	0.36	Bool18
13	NGC 6921	0.014	307.1202	25.7234	Ric15	41.8	43.0	0.57	0.52	0.35	Bool18
14	2MFGC02280	0.015	42.6775	54.7049	Ric15	41.0	43.0	1.52	1.71	0.90	Bool18
15	CDFS 443	0.895	53.1335	-27.7478	Bri14	41.9	43.0	5.00	0	-1	Bool18
16	IC 2560	0.010	154.0779	-33.5639	Ball14	41.2	43.1	3.87	1.10	0.83	Bool18
17	NGC 1320	0.009	51.2029	-3.0422	Ball14	41.3	43.2	3.11	1.06	0.78	Bool18
18	NGC 7130	0.016	327.0812	-34.9511	Ric15	40.9	43.2	1.56	1.08	0.63	Bool18
19	ESO 464-G016	0.036	315.5991	-28.1748	Ric15	42.2	43.2	0.38	0	-1	Bool18
20	CDFS 296	0.518	53.2734	-27.8709	Bri14	42.3	43.4	0.83	5.74	0.74	Bool18
21	NGC 7479	0.008	346.2358	12.3228	Ric15	40.7	43.4	1.17	0.68	0.29	Bool18
22	IC 3639	0.011	190.2200	-36.7558	Bool16	40.7	43.4	1.89	0.95	0.61	Bool18
23	NGC 1194	0.014	45.9546	-1.1036	Ric15	41.7	43.5	0.62	0.17	0.07	Bool18
24	NGC 3281	0.011	157.9671	-34.8536	Gou12	41.9	43.5	1.28	0.23	0.10	Bool18
25	CDFS 114	0.310	53.0356	-27.7800	Bri14	41.5	43.5	1.60	3.89	0.97	Bool18
26	MCG +08-03-018	0.020	20.6434	50.0550	Ric15	42.4	43.6	0.45	0.19	0.16	Bool18
27	ESO 138-G001	0.009	252.8338	-59.2347	Ric15	41.6	43.6	0.68	0.11	0.04	Bool18
28	MCG +06-16-028	0.016	108.5162	35.2793	Ric15	41.8	43.6	0.50	0.29	0.24	Bool18
29	CGCG 164-019	0.030	221.4033	27.0347	Ric15	41.8	43.7	0.72	0	-1	Bool18
30	Arp 299B	0.010	172.1292	58.5614	Pta15	41.8	43.7	0.43	0.15	0.12	Bool18
31	CDFS 273	0.229	53.0825	-27.6897	Bri14	41.5	43.7	0.86	2.49	0.62	Bool18
32	Circinus Galaxy	0.001	213.2912	-65.3392	Ric15	40.9	43.8	2.02	0.14	0.01	Ric15
33	ESO 201-IG004	0.036	57.5954	-50.3025	Ric15	42.1	43.8	0.74	0.40	0.14	Bool18
34	NGC 424	0.012	17.8650	-38.0833	Ric15	41.5	43.8	0.83	0.31	0.13	Bool18
35	NGC 7212NED02	0.027	331.7583	10.2335	Ric15	42.5	43.8	0.80	0.44	0.15	Bool18
36	CDFS 065	0.664	53.0673	-27.8282	Bri14	41.8	43.8	3.54	5.66	2.07	Bool18
37	CDFS 421	0.738	53.0770	-27.7656	Bri14	41.5	43.8	3.44	0	-1	Bool18
38	CDFS 347	0.280	53.1458	-27.9035	Bri14	41.2	43.8	2.72	0	-1	Bool18
39	CDFS 384	0.150	53.1750	-27.6639	Bri14	40.8	43.8	2.98	7.92	2.20	Bool18
40	ESO 406-G004	0.029	340.6390	-37.1853	Ric15	41.5	43.9	0.41	0.45	0.33	Bool18
41	CDFS 063	0.670	53.0751	-27.8315	Bri14	41.4	43.9	2.83	0	-1	Bool18
42	NGC 1068	0.004	40.6696	-0.0133	Ric15	41.3	43.9	0.57	0.04	0.01	Ric15
43	NGC 1229	0.036	47.0451	-22.9601	Ric15	42.5	44.0	0.37	0.24	0.22	Bool18

Table 1 : *cont.*

ID	Identifier	z	RA	DEC	source ref.	$\log L_{2-10\text{ keV}}^{\text{obs}}$	$\log L_{12\mu\text{m}}$	EW	+EW	-EW	EW ref.
(1)	(2)	(3)	(4)	(5)	(6)	(7)	(8)	(9)	(10)	(11)	(12)
44	CDFS 400	1.090	53.1049	-27.9138	Bri14	42.5	44.1	1.04	0.94	0.59	Boo18
45	IGR J14175-4641	0.077	214.2652	-46.6948	Ric15	42.9	44.1	0.41	0	-1	Boo18
46	CGCG 420-015	0.029	73.3571	4.0617	Ric15	42.6	44.2	0.36	0.06	0.02	Boo18
47	CDFS 158	0.738	53.0941	-27.7406	Bri14	41.8	44.2	1.15	1.51	0.75	Boo18
48	AEGIS 567	0.536	214.8070	52.8973	Bri14	42.0	44.2	2.45	0	-1	Boo18
49	Mrk 34	0.050	158.5358	60.0311	Gan14	43.1	44.3	0.86	0.94	0.58	Boo18
50	NGC 7674	0.029	351.9862	8.7792	Gan17	42.2	44.3	0.52	0.17	0.13	Boo18
51	NGC 6240	0.024	253.2454	2.4008	Ric15	42.9	44.3	0.41	0.15	0.04	Boo18
52	MCG +10-14-025	0.039	143.9654	61.3529	Ric15	41.7	44.3	0.64	0	-1	Boo18
53	CDFS 459	1.609	53.1228	-27.7228	Bri14	42.4	44.4	3.76	31.54	2.79	Boo18
54	AEGIS 602	0.769	214.8420	52.9219	Bri14	42.2	44.5	2.58	0	-1	Boo18
55	CDFS 264	2.026	53.0588	-27.7084	Bri14	43.1	44.7	1.74	2.31	1.37	Boo18
56	XMMID 60152	0.579	150.3122	1.7302	Lan15	43.7	44.7	0.57	0.38	0.26	Lan15
57	CDFS 039	3.660	53.0785	-27.8598	Bri14	43.7	44.8	1.25	0	-1	Boo18
58	CDFS 454	0.650	53.0446	-27.8019	Bri14	41.0	44.8	5.00	0	-1	Boo18
59	CDFS 448	0.680	53.0808	-27.6811	Bri14	41.8	44.9	1.47	4.86	1.12	Boo18
60	CDFS 401	1.370	52.9604	-27.8699	Bri14	42.7	45.0	1.11	1.12	0.88	Boo18
61	COSMOS 0581	1.778	150.2910	2.0895	Bri14	43.4	45.0	2.12	0	-1	Boo18
62	COSMOS 0987	0.353	149.7929	2.1256	Bri14	42.0	45.1	1.54	0	-1	Boo18
63	2MASX J03561995-6251391	0.108	59.0831	-62.8609	Ric15	43.4	45.1	0.20	0.19	0.03	Boo18
64	CDFS 460	2.145	53.0976	-27.7155	Bri14	42.5	45.1	1.93	0	-1	Boo18
65	COSMOS 0363	2.704	150.0459	2.2013	Bri14	44.4	45.2	0.91	0.96	0.60	Boo18
66	COSMOS 0482	0.120	150.4250	2.0663	Bri14	42.1	45.3	1.47	1.04	0.91	Boo18
67	XMMID 2608	0.125	150.4249	2.0660	Lan15	42.3	45.4	0.50	0.20	0.15	Lan15
68	COSMOS 2180	0.350	149.9758	2.4615	Bri14	42.1	45.5	5.00	0	-1	Boo18
69	BzK 4892	2.578	53.1488	-27.8211	Fer11	43.9	45.7	1.00	0.25	0.29	Corall6
70	CDFS 382	0.667	52.9624	-27.6879	Bri14	43.3	46.4	1.52	0	-1	Boo18
71	IRAS F15307+3252	0.930	233.1838	32.7131	H-L17	43.8	46.5	1.00	0.70	0.53	Boo18
72	XMMID 324	1.222	53.2051	-27.6806	Geo13	43.5	46.6	0.51	0.91	0.15	Geo13

Table 1: Complete list of all sources used in determining the anti-correlation plotted in Figure 4, ordered by rest-frame $12\mu\text{m}$ luminosity. Information on specific columns is as follows: (1) ID specific to each source, corresponding to the index featured on plots throughout the paper. (2) source name. (3) spectroscopic redshift. (4) right ascension in degrees. (5) declination in degrees. (6) Source reference. (7) Logarithm of the observed rest-frame $2-10\text{ keV}$ luminosity, measured in erg s^{-1} ; (8) Logarithm of the rest-frame $12\mu\text{m}$ luminosity predicted from the [Mullaney et al. \(2011\)](#) infrared spectral template; (9) Rest-frame neutral Fe K α fluorescence line EW measured in keV; (10) and (11) upper and lower limits on the rest-frame neutral Fe K α fluorescence line EW measured in keV (values of 0 and -1 respectively denote an upper limit to EW). (12) reference used for EW value. References: [Feruglio et al. \(2011, Fer11\)](#); [Goulding et al. \(2012, Gou12\)](#); [Georgantopoulos et al. \(2013, Geo13\)](#); [Brightman et al. \(2014, Br14\)](#); [Gandhi et al. \(2014, Gan14\)](#); [Baloković et al. \(2014, Bal14\)](#); [Lanzuisi et al. \(2015, Lan15\)](#); [Ricci et al. \(2015, Ric15\)](#); [Ptak et al. \(2015, Pta15\)](#); [Masini et al. \(2016a, Mas16\)](#); [Corral et al. \(2016, Cor16\)](#); [Gandhi et al. \(2017, Gan17\)](#); [Hlavacek-Larrondo et al. \(2017, H-L17\)](#); [Annuar et al. \(2017, Ann17\)](#); [Boo18](#): This work.

5 DISCUSSION

Our results indicate the presence of an Iwasawa-Taniguchi effect for Compton-thick AGN. This is surprising, since the majority of our sample is presumed to have a noticeable flux contribution from the reflected component in the ~ 6 – 7.9 keV energy region (e.g. Figure 1 - we will address this further in Section 5.2.1), and the Fe K α EW is not expected to vary relative to the underlying Compton-scattered reflection continuum. Here we discuss the significance of our result, as well as possible physical interpretations if confirmed on larger samples.

5.1 Significance of result

As a comparison to previous works, Table 2 includes the anti-correlation significance metric quoted for the studies into the Iwasawa-Taniguchi effect that we include in Figure 4, as well as the obscuration type of the sources included in the corresponding samples.

5.1.1 AGN dominance

In addition to estimating the effect of star formation contamination using high angular resolution observations (see Section 3.2.1), we sought to test the AGN dominance of our interpolated infrared luminosities. We use the colour criteria of Stern et al. (2012), Mateos et al. (2012) and Lacy et al. (2007) for observed flux densities (used to renormalise the Mullaney et al. 2011 AGN template and interpolate a rest-frame $12\mu\text{m}$ flux) from *WISE* and *Spitzer*, respectively. However, Stern et al. (2012) do note that the efficiency of such mid-infrared colour selections of AGN increases strongly with X-ray luminosity. As such, lower luminosity sources, e.g. with $L_{2-10\text{keV}} \lesssim 10^{43} \text{ erg s}^{-1}$, in our sample may not display AGN-like mid-infrared colours, and thus lie outside the wedge and cut thresholds. Alternatively, the sources lying outside the selection criteria may not be intrinsically weak - for example, Gandhi et al. (2015a) notes that bluer W1–W2 colours could arise from strong host star formation contamination or anisotropic/weak reprocessed torus emission. As such, sources satisfying any one of these three colour thresholds are most likely to not display star formation contamination, and be AGN-dominated in the mid-infrared. The flux densities are plotted in Figure 7. In total, 38/72 sources satisfy either Stern et al. (2012) and Mateos et al. (2012) combined (for *WISE*-based observations) or Lacy et al. (2007) (for *Spitzer*-based observations). This potentially indicates some form of star formation contamination (or another form of contaminant) present in the sources that do not satisfy these criteria. However, running a fit to only the 38 predicted AGN-dominated sources in our sample results in a gradient of $m = -0.04 \pm 0.06$ between EW and $L_{12\mu\text{m}}$, fully consistent with the main fit presented in Section 4, albeit with larger uncertainty.

As a further test of contamination in our sample, we carried out a fit only to sources displaying a deficit in observed X-ray to $12\mu\text{m}$ luminosity of greater than two orders of magnitude (see Figure 3). This again returned a consistent result with our main fit of $m = -0.08 \pm 0.05$ for 36 sources. These tests suggest that any star formation contamination does not dominate the trend that we observe.

5.1.2 Binning

Lastly, we carried out a fit to the sample binned by $12\mu\text{m}$ luminosity. A maximum binning of 9 sources optimised total number of bins together with sources per bin. We approximated all upper limits as the average between the limit and $\log 100 \text{ eV}$, then assigned a $1\text{-}\sigma$ error to the new point that encompassed $\log 100 \text{ eV}$ to the limit. The corresponding binned EW error for each bin was then given by:

$$\sigma_{\text{EW}} = \frac{\sqrt{\sum \delta \text{EW}^2}}{N} \quad (3)$$

Here N refers to the number of sources in each bin. The best fit gradient we get to the binned data is $\log(\text{EW}_{\text{FeK}\alpha}) \propto -0.06^{+0.05}_{-0.08} \log(L_{12\mu\text{m}})$, and is plotted in Figure 8 with a red solid line and one standard deviation shading. The best fit to the original sample is shown with a dashed (black) line, which is fully consistent with the binned gradient. The binned data has been renormalised to have the same y-intercept as the original result for easier visual comparison of gradients. The background grey points show the original data.

5.2 Physical interpretation

5.2.1 Covering factor dependence

The EW of the Fe K α line measured solely relative to the reprocessed continuum is very rarely $< 1 \text{ keV}$ (see Figure 8 of Murphy & Yaqoob 2009). One way to achieve an observed EW significantly less than 1 keV is via leaked intrinsic AGN emission contributing some flux to the observed spectrum in the iron line region. An example of this would be in transmission-dominated Compton-thick AGN, or a ‘clumpy’ torus. Typical X-ray spectral model predictions (see Figure 1) for AGN show that for column densities, $N_{\text{H}} \gtrsim 1.5 \times 10^{24} \text{ cm}^{-2}$, the observed reflected flux is $\gtrsim 10$ times more than the transmitted flux. Below this column density, a borderline Compton-thin/thick AGN could have a reasonable contribution in flux from the transmitted component, and hence a variable continuum with intrinsic luminosity. One way to obtain less reflected flux with increasing column would be a decreased covering factor, which has been dubbed the ‘receding torus’, and was suggested to explain the Iwasawa-Taniguchi effect for unobscured and mildly obscured sources previously (e.g. Page et al. 2004; Ricci et al. 2013b, see Section 1 of this paper). However, Lawrence & Elvis (2010) discuss that the apparent decrease of obscured AGN fraction with bolometric luminosity is much less significant in IR/radio samples than with X-ray samples, suggesting that the receding torus model may not exist in nature.

In Figure 9, we show a colour map of simulated EWs predicted from the *borus02* model for an $\sim \text{edge on}$ (84°) viewing angle, with varying column densities and covering factors. All spectra were simulated using *fakeit* from within *xspec* with the *NuSTAR* simulation files provided by the *NuSTAR* team¹⁰, and then the resulting spectrum was re-fit in the 6 – 7 keV energy region by a *POWERLAW* + *GAUSSIAN* model. The EW of a narrow (FWHM $\sim 2 \text{ eV}$) Gaussian was

¹⁰ https://www.nustar.caltech.edu/page/response_files

Reference (1)	Metric (2)	Value (3)	No. of sources (4)	Obscuration class (5)
This work	Prob.	98.7%	54	Compton-thick
Ricci et al. 2014	Prob.	99%	47	Seyfert 2
Bianchi et al. 2007	Prob.	99.6%	157	Unobscured
Jiang et al. 2006	ρ	-0.47	101	Unobscured
Page et al. 2004	Prob.	> 99.98%	53	Unobscured
Iwasawa & Taniguchi 1993	Corr. coeff.	> 0.8	37	Unobscured

Table 2. Summary of the anti-correlation probability significances found for the studies into the Iwasawa-Taniguchi effect included in Figure 4. The table lists the (1) study reference, (2) the correlation metric used to quantify the significance of the resulting anti-correlation: ‘Prob.’ - probability of an anti-correlation; ‘ ρ ’ - Spearman’s Rank correlation coefficient; ‘Corr. coeff.’ - correlation coefficient, (3) the value of the correlation metric found by the work, (4) the number of objects in each sample, and (5) the obscuration classes of the sources included in the corresponding work.

then derived at fixed line centroid ($E_L = 6.4$ keV, using the `eqwidth` command in `xspect`). We also overplot the limiting contour at which all EWs are > 1 keV, which we take as a proxy for reflection-dominance. Interestingly, for lower covering factors (higher opening angles), the column density can be high ($\log N_H > 24.3$ in some cases), and still feature a spectrum with presumably leaked transmitted emission. Since our original N_H selection was $\log N_H > 24.18$ ($N_H > 1.5 \times 10^{24} \text{ cm}^{-2}$) to 90% confidence from literature values, from this plot we cannot rule out that the higher luminosity sources (with assumed lower covering factors) would feature some sort of leaked transmitted flux contributing to the continuum around 6.4 keV and decreasing observed neutral Fe $K\alpha$ EW. Furthermore, if the luminosity-dependent covering factor explanation is correct, then we are currently lacking such reflection-dominated Compton-thick AGN at high luminosities since the Fe $K\alpha$ EW is predicted to always be greater than 1 keV for $N_H \gtrsim 1.5 \times 10^{24} \text{ cm}^{-2}$.

As an additional test, we selected sources with literature best fit *lower* 90% uncertainty on the column density to be $N_H > 1.5 \times 10^{24} \text{ cm}^{-2}$. This returned 14 sources, with only two sources at higher redshift (COSMOS 0363; $z = 2.704$ and BzK 4892; $z = 2.578$). Although the corresponding best fit to this sample returns a gradient of $m = -0.10^{+0.07}_{-0.08}$, which is entirely consistent with the result for the full sample, we lack enough robustly reflection-dominated sources at higher redshifts to draw precise conclusions for a transmitted component altering the narrow Fe $K\alpha$ line.

An alternative way to detect a considerable contribution from the transmitted component in Compton-thick AGN would be via changing-look AGN variability. In this scenario, the Compton-thick obscurer is clumpy, enabling clouds of differing column to traverse the line of sight, potentially resulting in leaked intrinsic emission. Such extreme eclipsing events from Compton-thin to Compton-thick levels of obscuration have been observed previously (Risaliti et al. 2007), but are rare. As such, this is unlikely to be responsible for the diminished Fe $K\alpha$ lines observed in all higher luminosity sources of the sample where we see the greatest decrease in EW, but may play a non-negligible role.

5.2.2 Ionisation

Finally, we consider the effects of ionisation on Compton-thick X-ray spectra. As mentioned in Section 1, many obscured candidate AGN not only show diminished neutral Fe $K\alpha$ line EWs, but also increased ionised Fe $K\alpha$ EWs with intrinsic luminosity (Iwasawa et al. 2009). Indeed, a correlation between spectral slope (a proxy for the accretion efficiency of AGN) with the Fe $K\alpha$ line energy was found by Dewangan (2002). From Figure 4, one would expect this effect to be most prevalent for intrinsically bright (i.e. high L_{bol} and/or high Eddington ratio) systems, which may be more *intrinsically* UV-luminous relative to X-rays.

To robustly test this would require an ionised toroidal X-ray reprocessing model, which is currently unavailable. For this reason, we use the `xillver` (García et al. 2013) disc reflection model, which calculates a spectrum from the accretion disc surrounding AGN including reflection and also ionised emission lines. Figure 10 illustrates the approximate EWs of the ionised 6.70 and 6.97 keV iron emission lines and neutral Fe $K\alpha$ line as a function of ionisation parameter. This is defined as $\xi = 4\pi F_X/n_e$ (García et al. 2013), where F_X is the net flux in the 1–1000 Ry energy region, and n_e is the electron number density. From Figure 10, one can infer that the dominance of ionised lines increases with respect to the neutral ones for high values of ξ . Thus, ionisation could be a potential explanation for our results.

5.2.3 Other possibilities

Another possibility for a depleted neutral iron line in a Compton-thick candidate AGN would be dilution of the reflection spectrum by scattered primary emission from the AGN that is reprocessed by a diffuse ionised ‘mirror’ in a line of sight direction of lower column density. Such a component would scale with intrinsic luminosity and thus contribute to the Iwasawa-Taniguchi effect. In fact, a considerable scattered fraction of intrinsic emission was found to explain the observed X-ray spectrum of the local Compton-thick AGN NGC 7674 by Gandhi et al. (2017). The authors find a fraction of $\sim 2 - 10\%$ to 90% confidence could explain the low

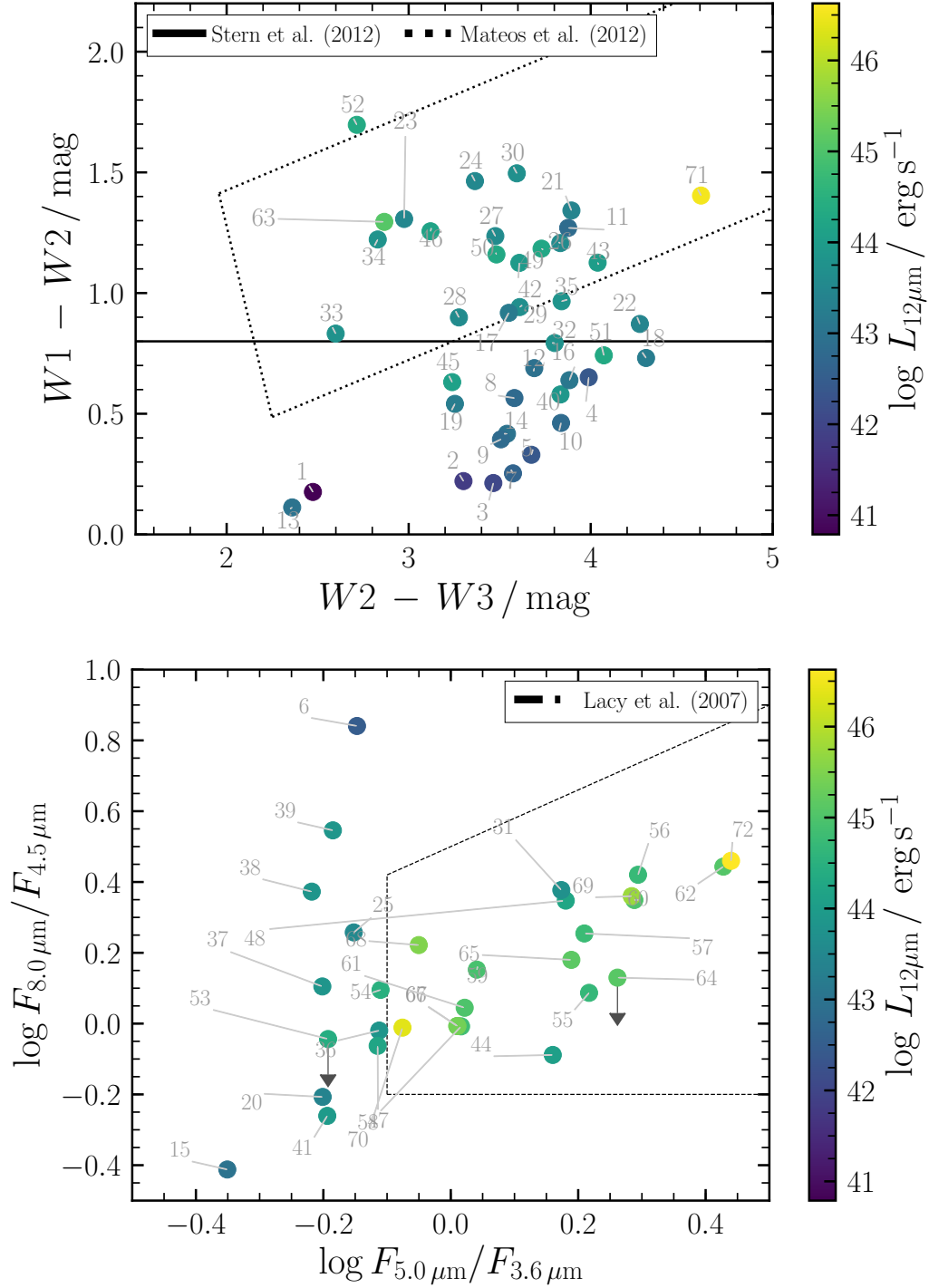


Figure 7. Colour selection criteria for *WISE* (top panel) and *Spitzer* (bottom panel) flux densities. The *WISE* thresholds are from Stern et al. (2012) and Mateos et al. (2012), and the *Spitzer* colour wedge is from Lacy et al. (2007). In total, 38/72 sources lie outside these criteria, but after testing the possible effects of star formation on these sources, we still require a significant anti-correlation to fit the data - see Section 3.2.1 for details.

observed EW of the neutral Fe K α line from this Compton-thick source.

A second tentative explanation for an obscured Iwasawa-Taniguchi effect comes from dual AGN candidate systems, in which a spatially unresolved, less-obscured AGN

is present in combination with a heavily obscured source. Supermassive black hole evolution simulations (from, e.g. Hopkins et al. 2008) predict luminous quasars to originate from gas-rich mergers. Immediately post-merger, these sources are predicted to be deeply embedded in the large dust and

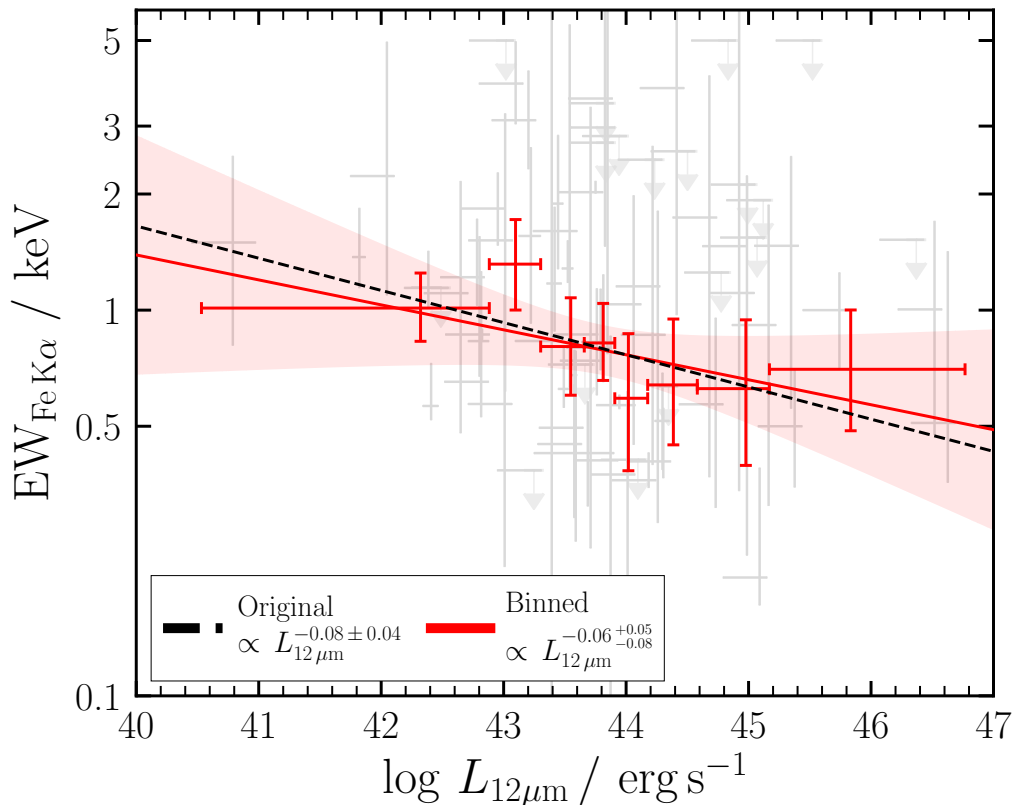


Figure 8. The best fit to the binned sample, with a maximum of 9 sources per bin (see the text for details of the binning method used). The red shaded region shows the standard deviation from the mean of our fit, which is fully consistent with the original best fit found for the unbinned data (shown with a black dotted line). This has been renormalised to the same y-intercept as the binned fit to allow an easier comparison between gradients. Background grey points show the source data that was binned.

gas reservoirs that are rapidly being accreted, which absorb optical to X-ray emission and reprocess this at infrared wavelengths. Depending on the spatial separation of the merging supermassive black holes, the extracted X-ray spectrum could actually be the combined contribution from two components of differing obscuration levels. Koss et al. (2016) used *NuSTAR* to spatially resolve the emission from the dual AGN in NGC 6921. The authors found the two AGN components to be Compton-thick, but were able to separately study each independently in the >10 keV waveband. If one component of a dual AGN were less obscured, but contributed a considerable proportion of the total flux contribution, this could result in a diminished Fe K α complex in some post-merger candidates such as hyperluminous ($L_{8-1000\mu\text{m}} > 10^{13} L_{\odot}$) infrared galaxies, Dust Obscured Galaxies (Dey et al. 2008, DOGs) and Hot DOGs (Wu et al. 2012). For example, recent works have postulated the presence of dual AGN in NGC 7674 (Kharb et al. 2017) and Mrk 273 (Iwasawa et al. 2017). Furthermore, Vito et al. (2018) recently studied the X-ray emission from 20 Hot DOGs, and found typical predicted X-ray line of sight column densities of $N_{\text{H}} \sim 1 - 1.5 \times 10^{24} \text{ cm}^{-2}$. This is illustrated in Figure 11, in which we plot the composite spectrum in black (solid line), formed by combining the spectrum from a reflection-dominated AGN ($\log N_{\text{H}}/\text{cm}^{-2} = 24.5$; red dashed line) and an unobscured AGN ($\log N_{\text{H}}/\text{cm}^{-2} = 22$; blue dot-dashed

line). Higher angular resolution X-ray instruments would be required to separate the two components and stringently test this hypothesis. We further note that both a strong scattered component as well as dual AGN would struggle to explain the observed prominence of ionised iron emission lines often observed in the X-ray spectra of infrared-luminous systems (Teng et al. 2014; Gilli et al. 2014; Farrah et al. 2016).

A final possibility arises from the effects of dust grains on X-ray photons. Typical X-ray reprocessing spectral models consist of ray-tracing through a dust-free gas, but not all consider the possible effects that dust grains have on the observed X-ray spectrum in detail. In fact, Draine (2003) has shown that $\sim 90\%$ of the incident power at energy $E = 6.4$ keV on dust grains scatter with angle, $\theta_s < 0.05^\circ$, relative to the incident photon direction. Gohil & Ballantyne (2015) further found that such a large anisotropic emission associated with dust grains, as opposed to the isotropic emission of hot gas typically invoked in X-ray reprocessing torus models could enhance the Fe K α line EW relative to the underlying reflection continuum by up to factors of ~ 8 for Compton-thick gas. More luminous AGN would be expected to have a larger dust sublimation radius, and thus have an altered Fe K α EW relative to the less luminous sources, presumably with smaller dust sublimation radii. Such a scenario effectively decouples the Fe K α line from the underlying reflection continuum, and there is already tentative evidence

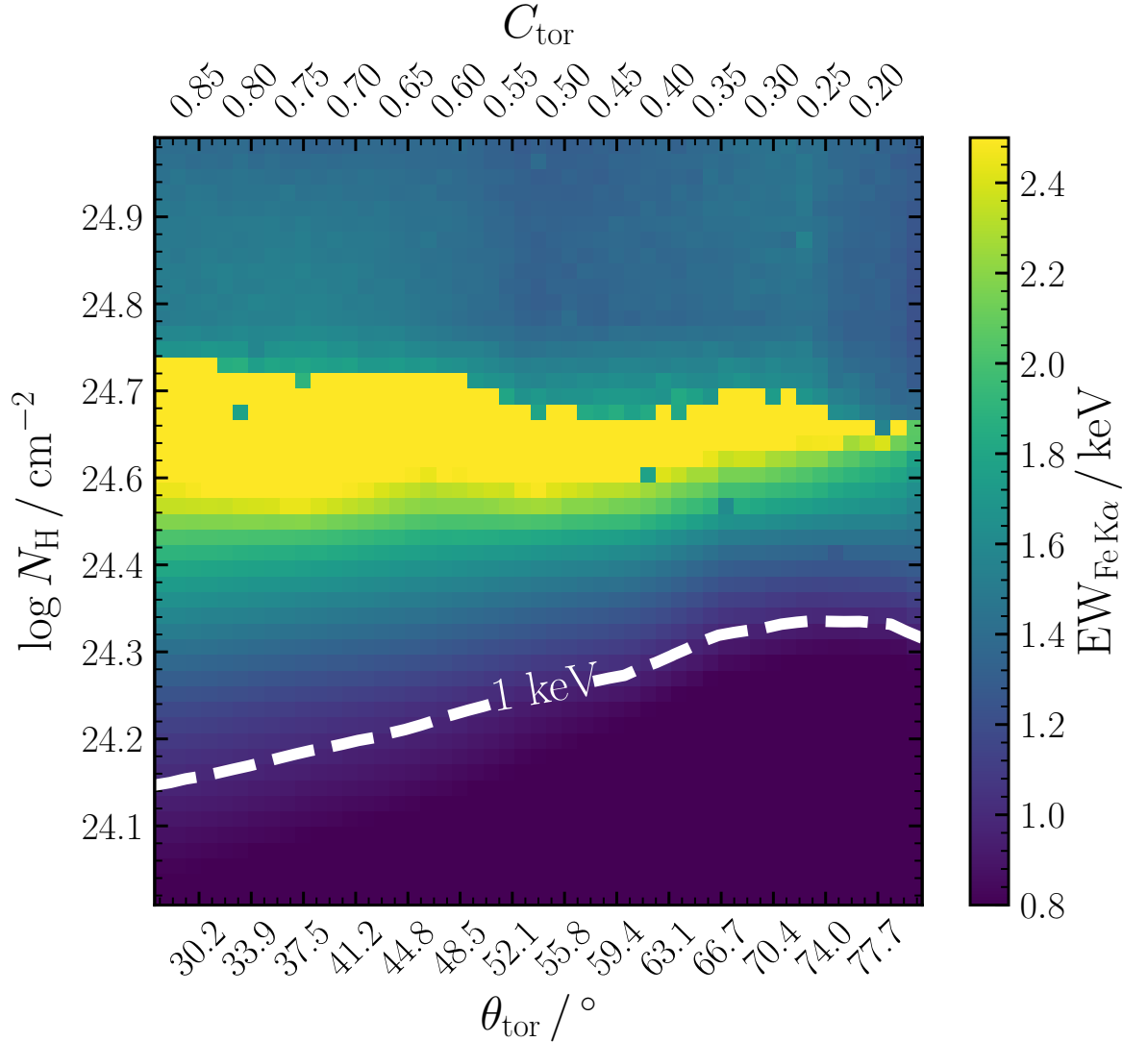


Figure 9. A colour map of simulated neutral iron $K\alpha$ EW for a series of line of sight column densities (N_H) and torus covering factors ($C_{\text{tor}} = \cos \theta_{\text{tor}}$) in the *borus02* (Baloković et al. 2018) model. For these simulations, the line of sight column density and equatorial column density were tied together. Spectra were simulated using the *NuSTAR* response matrices. The simulated spectra were then fit in the 6–7 keV energy region with a *POWERLAW* + *GAUSSIAN* to derive a predicted EW. The contour shows the boundary at which all EW are predicted to be > 1 keV. All EWs predicted to be < 0.8 keV or > 2.5 keV were capped (shown with the same minimum and maximum colour, respectively). Due to our selection of sources with $\log N_H > 24.18$ ($N_H > 1.5 \times 10^{24} \text{cm}^{-2}$) to 90% confidence from literature values, we cannot rule out sources as having at least a partial EW dependence with covering factor, as can be seen by this region of the colour map.

suggesting that these two components may arise from physically separate regions within the torus dust sublimation zone (Gandhi et al. 2015b).

5.3 Implications

5.3.1 Redshift Evolution of Compton-thick AGN

As stated earlier, multiple works predict the obscured fraction of AGN to decrease with increasing luminosity and/or Eddington fraction (Ueda et al. 2011; Merloni et al. 2014; Georgakakis et al. 2017). In addition, since the number of luminous AGN is predicted to increase with redshift, this

would imply a redshift evolution of obscuration amongst AGN. However, the anti-correlation we report could lead to a correction to X-ray inferred column densities, that were derived based on fitting an observed iron line. From Figure 4, this correction factor would be largest for the most luminous sources. Depending on the relative contributions at different luminosities, this could then alter the obscured fraction dependence with luminosity. Some evidence has indicated a weak or no evolution of the obscured AGN fraction. For example, Vito et al. (2014) studied a sample of 141 X-ray selected AGN at $3 < z \leq 5$ and found no evidence for an anti-correlation between obscured fraction and luminosity, despite suggesting that this may be due to the

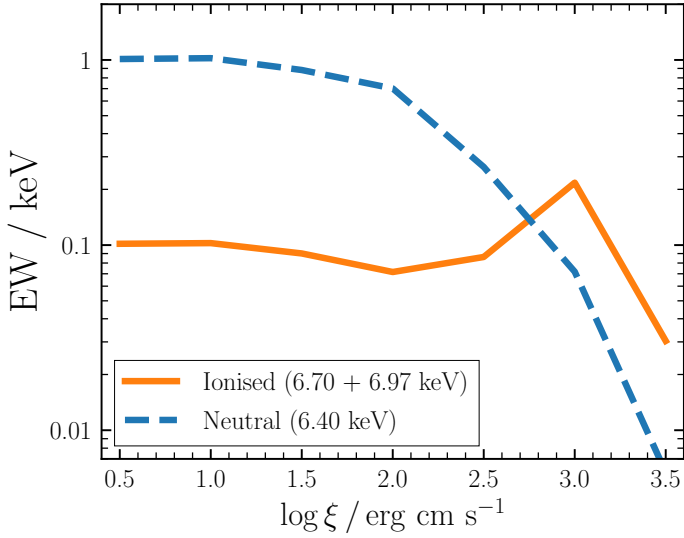


Figure 10. *xillver* Simulated EWs of the ionised iron lines at 6.70 and 6.97 keV (solid orange line) together with neutral Fe K α line EW (dotted blue line) as a function of ionisation parameter. The EWs were calculated by integrating the flux in the continuum between 5.9–7.2 keV, subtracted from the flux in the lines (integrated ± 0.05 keV of each predicted line centroid), and then divided by the interpolated continuum at the line centroid. The spectra were simulated using the *xillver* spectral model, assuming an inclination of 18.2° (\sim face-on, i.e. maximum reflection).

non-detection of the lower luminosity obscured sources at higher redshift. In contrast, Mateos et al. (2017) only found a weak luminosity dependence of the type 2 AGN fraction for covering factors derived from infrared clumpy torus modelling for $z \leq 1$, and Buchner et al. (2015) further found a constant Compton-thick fraction with redshift or accretion luminosity for a sample of ~ 2000 AGN.

To test if our result is biased by redshift, we further separated our sample into two redshift bins, below and above the median redshift of 0.038. Figure 12 shows the redshift distribution of our sample with the median redshift shown with an orange (vertical) line. Carrying out a fit to either redshift bin independently yielded consistent gradients of $m = -0.19^{+0.06}_{-0.07}$ and $m = -0.04 \pm 0.08$, for the low and high redshift bins respectively, albeit with large scatter.

5.3.2 The Growth Rate of AGN

Current X-ray reprocessing torus models do not account for the possible effects of dust grains, and/or reflector ionisation on the observed reflection spectrum. To zeroth order, such a model could interpret a less prominent neutral Fe K α line as evidence for a lower obscuring column than the true value for intrinsically bright, heavily obscured objects if our results are confirmed using larger sample studies. In the most extreme case, a Compton-thick system could be predicted to be only mildly obscured. From Figure 3, this would mean underpredicting the intrinsic X-ray luminosity, and hence the growth rate of such systems, potentially by factors of around two orders of magnitude.

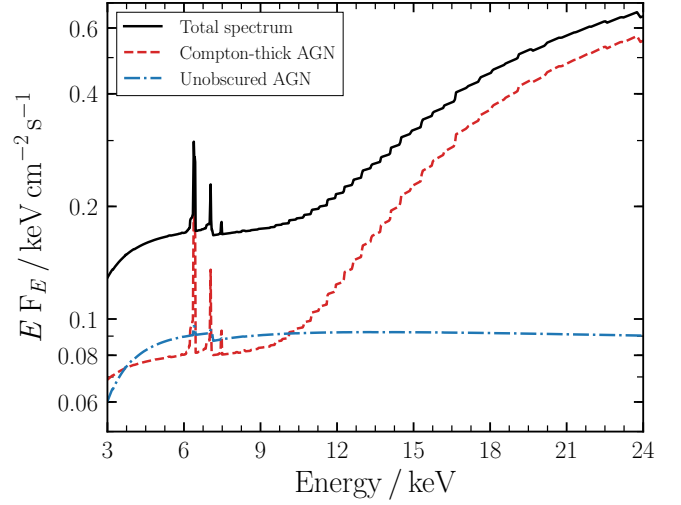


Figure 11. Dual-AGN schematic to explain the lower observed Fe K α EWs observed in luminous and ultraluminous infrared galaxies ($L_{8-1000\mu\text{m}} > 10^{11} L_\odot$ and $L_{8-1000\mu\text{m}} > 10^{12} L_\odot$, respectively). If an AGN were observed post-merger, the two supermassive black holes could exist temporarily separately, but spatially unresolved, leading to an observed (solid black line) composite spectra from two AGN. The individual unobscured (dot-dash, blue) and obscured (dashed, red) predicted AGN spectra are also plotted. Depending on the relative contributions in observed flux from either component, the total spectrum could have characteristics of a mildly obscured AGN, despite containing a heavily obscured source. Both the AGN spectra were simulated using the *borus02* model.

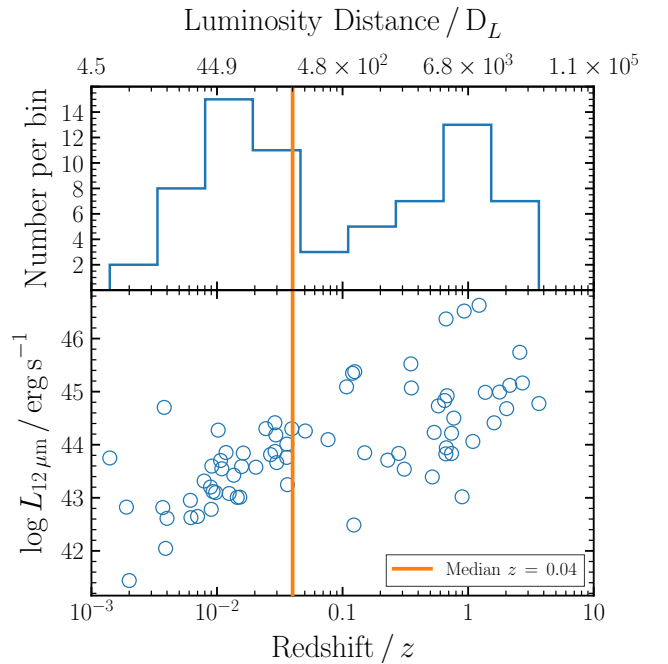


Figure 12. Redshift distribution of our sample, according to the rest-frame $12\mu\text{m}$ luminosity. The median redshift was chosen to split the sample into two redshift bins, in order to provide comparable numbers of sources in either bin.

5.4 The Future

Clearly one of the major sources of uncertainty in the relation we report here is on the EW of the Fe K α line. However, many future X-ray missions can improve on this uncertainty, such as the *X-ray Astronomy Recovery Mission (XARM)*¹¹, or *Athena* (Nandra et al. 2013). *XARM* will enable high spectral resolution studies of the iron line (e.g. Hitomi Collaboration et al. 2017) and be able to test the ionisation scenario directly. Additionally, *Athena* will probe high redshift Compton-thick AGN sensitively. Figure 13 shows the possibilities with the *Athena* Wide Field Imager (WFI), with a 20 ks simulated spectrum shown in purple together with the original 4 Ms *Chandra* Deep Field South observed spectrum for CDFS 384 from our sample, shown in black. Clearly the signal to noise is dramatically enhanced at the Fe K α (rest-frame 6.4 keV) line as well as the neighbouring continuum, enabling a huge improvement on the calculated EW contour in the lower panel of the figure. The simulated spectrum was calculated from the original best fit model to the observed *Chandra* spectrum. What this figure clearly shows, however, is that the confidence range on the EW of such obscured objects will be powerfully improved with the advent of such high-sensitivity instruments in the future.

6 SUMMARY

Here we have carried out the first study into the Iwasawa-Taniguchi effect for Compton-thick AGN. Our key findings are enumerated below:

(i) We select from the literature a sample of 72 Compton-thick candidate AGN, covering a redshift range of $z \sim 0.0014 - 3.7$. The candidates were confirmed via an offset between predicted intrinsic and observed X-ray luminosity, given the rest-frame $12 \mu\text{m}$ luminosity interpolated from the Mullaney et al. (2011) AGN infrared spectral template.

(ii) We find an anti-correlation between the rest-frame equivalent width of the narrow core of the neutral Fe K α fluorescence emission line and the mid-infrared $12 \mu\text{m}$ continuum luminosity, which we use as a proxy for the bolometric AGN luminosity. From the Spearman's Rank, we find the anti-correlation to be significant to 98.7% confidence.

(iii) We discuss four possible interpretations of such an anti-correlation:

- (a) A luminosity-dependent covering factor (Section 5.2.1).
- (b) Luminosity-dependent ionisation state of the circumnuclear reprocessing material (Section 5.2.2).
- (c) Other possibilities including the contribution from two AGN in a dual system (Section 5.2.3).
- (iv) Possible implications of the Compton-thick Iwasawa-Taniguchi effect include:

- (a) An increased number density of Compton-thick AGN at higher redshifts due to predicted higher intrinsic luminosities (Section 5.3.1).

¹¹ <https://heasarc.gsfc.nasa.gov/docs/xarm/>

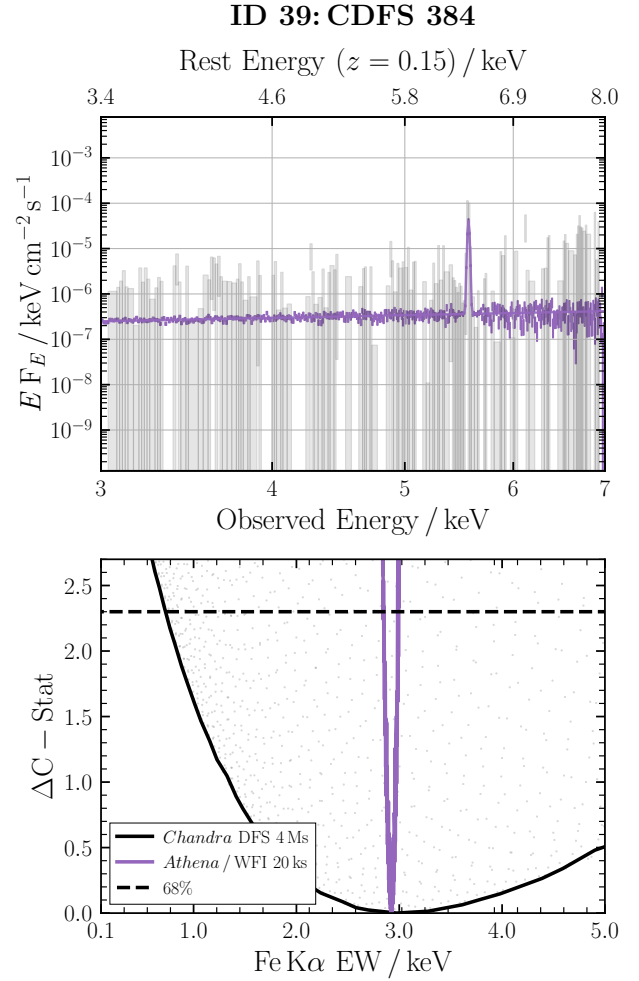


Figure 13. Top panel: Observed *Chandra* Deep Field South (CDFS) 4 Ms spectrum for CDFS 384 together with simulated *Athena*/WFI spectrum for a 20 ks observation, shown in black and purple, respectively. Lower panel: Reported EW contour for CDFS 384 used in the paper, together with the improved contour attained with the simulated *Athena*/WFI spectrum shown above. A dramatic improvement to the S/N of the observed spectrum is clearly attainable with *Athena*, not to mention the improved EW confidence region. Such observations of Compton-thick AGN are to be carried out as part of the *Athena* mission, with the aim to study obscured accretion and galaxy formation with the WFI instrument.

(b) Current X-ray reprocessing models do not account for this effect, and as such may incorrectly interpret a weak Fe K α line as a signature of Compton-thin reprocessing, leading to an under-estimation of the true intrinsic luminosity and hence growth rate of X-ray-obscured AGN.

(c) If a luminosity-dependent covering factor can explain the Iwasawa-Taniguchi effect, it would imply that we are still lacking a population of truly reflection-dominated, luminous Compton-thick AGN, since for $N_{\text{H}} \gtrsim 1.5 \times 10^{24} \text{ cm}^{-2}$, the EW of the Fe K α line are predicted to always be $> 1 \text{ keV}$, contrary to what we find.

(v) This work further illustrates why the Fe K α line alone

cannot be directly used to accurately determine the line of sight column density to a source. Future dedicated studies of Compton-thick AGN over broad redshift ranges are required to be able to confirm this effect, which could further hold the answers to understanding the physical geometry and evolution of obscuration surrounding AGN.

ACKNOWLEDGEMENTS

We thank the anonymous referee for invaluable comments on the paper.

P.B. and P.G. (grant reference ST/J003697/2) thank the STFC for support. In addition, the authors thank R. Gilli and C. Circosta for providing the 4 and 7 Ms spectra of LESS J0033229.4-275619 used in Figure 2.

This work was supported in part by the Black Hole Initiative at Harvard University, which is funded by a grant from the John Templeton Foundation.

M.B. acknowledges support from NASA Headquarters under the NASA Earth and Space Science Fellowship Program, grant NNX14AQ07H.

We acknowledge financial support from FONDECYT 1141218 (C.R.), Basal-CATA PFB-06/2007 (C.R.), the China-CONICYT fund (C.R.). This work is partly sponsored by the Chinese Academy of Sciences (CAS), through a grant to the CAS South America Center for Astronomy (CASSACA) in Santiago, Chile.

The scientific results reported in this article are based on observations made by the *Chandra* X-ray Observatory.

This research has made use of data, software and/or web tools obtained from the High Energy Astrophysics Science Archive Research Center (HEASARC), a service of the Astrophysics Science Division at NASA/GSFC and of the Smithsonian Astrophysical Observatory's High Energy Astrophysics Division.

This research has made use of the NASA/IPAC Extragalactic Database (NED), which is operated by the Jet Propulsion Laboratory, California Institute of Technology, under contract with the National Aeronautics and Space Administration.

This work made use of data from the *NuSTAR* mission, a project led by the California Institute of Technology, managed by the Jet Propulsion Laboratory, and funded by the National Aeronautics and Space Administration. We thank the *NuSTAR* Operations, Software and Calibration teams for support with the execution and analysis of these observations. This research has made use of the *NuSTAR* Data Analysis Software (NuSTARDAS) jointly developed by the ASI Science Data Center (ASDC, Italy) and the California Institute of Technology (USA).

This work is based [in part] on observations made with the *Spitzer* Space Telescope, which is operated by the Jet Propulsion Laboratory, California Institute of Technology under a contract with NASA.

This publication makes use of data products from the Wide-field Infrared Survey Explorer, which is a joint project of the University of California, Los Angeles, and the Jet Propulsion Laboratory/California Institute of Technology, funded by the National Aeronautics and Space Administration.

This work made use of the NumPy (Van Der Walt et al.

2011), Matplotlib (Hunter 2007), SciPy (Jones et al. 2001), pandas (McKinney 2010), Astropy (Astropy Collaboration et al. 2013) and adjustText¹² Python packages.

P.B. would also like to thank S.Hönig, C.Knigge, J.Matthews, M.Middleton, M.Smith, A.Beri, A.Hill, J.Buchner and others for vital scientific discussions into the data analysis and interpretations of the Compton-thick Iwasawa-Taniguchi effect.

REFERENCES

- Annuar A., et al., 2015, *ApJ*, **815**, 36
 Annuar A., et al., 2017, *ApJ*, **836**, 165
 Antonucci R., 1993, *ARA&A*, **31**, 473
 Arévalo P., et al., 2014, *ApJ*, **791**, 81
 Asmus D., Hönig S. F., Gandhi P., Smette A., Duschl W. J., 2014, *MNRAS*, **439**, 1648
 Asmus D., Gandhi P., Hönig S. F., Smette A., Duschl W. J., 2015, *MNRAS*, **454**, 766
 Astropy Collaboration et al., 2013, *A&A*, **558**, A33
 Baldwin J. A., 1977, *ApJ*, **214**, 679
 Ballantyne D. R., 2014, *MNRAS*, **437**, 2845
 Baloković M., et al., 2014, *ApJ*, **794**, 111
 Baloković M., et al., 2018, *ApJ*, **854**, 42
 Bauer F. E., et al., 2015, *ApJ*, **812**, 116
 Bianchi S., Guainazzi M., Matt G., Fonseca Bonilla N., 2007, *A&A*, **467**, L19
 Boorman P. G., et al., 2016, *ApJ*, **833**, 245
 Brightman M., Nandra K., 2011, *MNRAS*, **414**, 3084
 Brightman M., et al., 2013, *MNRAS*, **433**, 2485
 Brightman M., Nandra K., Salvato M., Hsu L.-T., Aird J., Rangel C., 2014, *MNRAS*, **443**, 1999
 Brightman M., et al., 2016, *ApJ*, **826**, 93
 Buchner J., et al., 2015, *ApJ*, **802**, 89
 Burlon D., Ajello M., Greiner J., Comastri A., Merloni A., Gehrels N., 2011, *ApJ*, **728**, 58
 Cash W., 1979, *ApJ*, **228**, 939
 Chen C.-T. J., et al., 2017, *ApJ*, **837**, 145
 Corral A., et al., 2016, *A&A*, **592**, A109
 Dewangan G. C., 2002, *ApJ*, **581**, L71
 Dey A., et al., 2008, *ApJ*, **677**, 943
 Draine B. T., 2003, *ApJ*, **598**, 1026
 Farrah D., et al., 2016, *ApJ*, **831**, 76
 Feruglio C., Daddi E., Fiore F., Alexander D. M., Piconcelli E., Malacaria C., 2011, *ApJ*, **729**, L4
 Gandhi P., Horst H., Smette A., Hönig S., Comastri A., Gilli R., Vignali C., Duschl W., 2009, *A&A*, **502**, 457
 Gandhi P., et al., 2013, *ApJ*, **773**, 51
 Gandhi P., et al., 2014, *ApJ*, **792**, 117
 Gandhi P., Yamada S., Ricci C., Asmus D., Mushotzky R. F., Ueda Y., Terashima Y., La Parola V., 2015a, *MNRAS*, **449**, 1845
 Gandhi P., Hönig S. F., Kishimoto M., 2015b, *ApJ*, **812**, 113
 Gandhi P., et al., 2017, *MNRAS*, **467**, 4606
 García J., Dauser T., Reynolds C. S., Kallman T. R., McClintock J. E., Wilms J., Eikmann W., 2013, *ApJ*, **768**, 146
 Georgakakis A., et al., 2017, *MNRAS*, **469**, 3232
 Georgantopoulos I., et al., 2013, *A&A*, **555**, A43
 Gilli R., et al., 2011, *ApJ*, **730**, L28
 Gilli R., et al., 2014, *A&A*, **562**, A67
 Gohil R., Ballantyne D. R., 2015, *MNRAS*, **449**, 1449

¹² <https://github.com/Phlya/adjustText>

- Goulding A. D., Alexander D. M., Bauer F. E., Forman W. R., Hickox R. C., Jones C., Mullaney J. R., Trichas M., 2012, *ApJ*, **755**, 5
- Haardt F., Maraschi L., 1991, *ApJ*, **380**, L51
- Haardt F., Maraschi L., 1993, *ApJ*, **413**, 507
- Harrison F. A., et al., 2013, *ApJ*, **770**, 103
- Hitomi Collaboration et al., 2017, preprint, ([arXiv:1711.06289](https://arxiv.org/abs/1711.06289))
- Hlavacek-Larrondo J., et al., 2017, *MNRAS*, **464**, 2223
- Hopkins P. F., Hernquist L., Cox T. J., Kereš D., 2008, *ApJS*, **175**, 356
- Horst H., Gandhi P., Smette A., Duschl W. J., 2008, *A&A*, **479**, 389
- Hunter J. D., 2007, *Computing In Science & Engineering*, 9, 90
- Ikeda S., Awaki H., Terashima Y., 2009, *ApJ*, **692**, 608
- Iwasawa K., Taniguchi Y., 1993, *ApJ*, **413**, L15
- Iwasawa K., Sanders D. B., Evans A. S., Mazzarella J. M., Armus L., Surace J. A., 2009, *ApJ*, **695**, L103
- Iwasawa K., U V., Mazzarella J. M., Medling A. M., Sanders D. B., Evans A. S., 2017, preprint, ([arXiv:1711.01750](https://arxiv.org/abs/1711.01750))
- Jiang P., Wang J. X., Wang T. G., 2006, *ApJ*, **644**, 725
- Jones E., Oliphant T., Peterson P., et al., 2001, SciPy: Open source scientific tools for Python, <http://www.scipy.org/>
- Kharb P., Lal D. V., Merritt D., 2017, *Nature Astronomy*, **1**, 727
- Koss M. J., et al., 2016, *ApJ*, **824**, L4
- Koss M., et al., 2017, *ApJ*, **850**, 74
- Krolik J. H., Madau P., Zycki P. T., 1994, *ApJ*, **420**, L57
- Lacy M., Petric A. O., Sajina A., Canalizo G., Storrie-Lombardi L. J., Armus L., Fadda D., Marleau F. R., 2007, *AJ*, **133**, 186
- Lanzuisi G., Piconcelli E., Fiore F., Feruglio C., Vignali C., Salvato M., Gruppioni C., 2009, *A&A*, **498**, 67
- Lanzuisi G., et al., 2015, *A&A*, **573**, A137
- Lawrence A., 1991, *MNRAS*, **252**, 586
- Lawrence A., Elvis M., 1982, *ApJ*, **256**, 410
- Lawrence A., Elvis M., 2010, *ApJ*, **714**, 561
- Levenson N. A., Radomski J. T., Packham C., Mason R. E., Schaefer J. J., Telesco C. M., 2009, *ApJ*, **703**, 390
- Lightman A. P., White T. R., 1988, *ApJ*, **335**, 57
- Lu Y., Yu Q., 1999, *ApJ*, **526**, L5
- Lusso E., et al., 2013, *ApJ*, **777**, 86
- Lutz D., Maiolino R., Spoon H. W. W., Moorwood A. F. M., 2004, *A&A*, **418**, 465
- Malizia A., Molina M., Bassani L., Stephen J. B., Bazzano A., Ubertini P., Bird A. J., 2014, *ApJ*, **782**, L25
- Marchesi S., Ajello M., Comastri A., Cusumano G., La Parola V., Segreto A., 2017, *ApJ*, **836**, 116
- Masini A., Comastri A., Puccetti S., Baloković M., Gandhi P., 2016a, in prep.
- Masini A., et al., 2016b, *A&A*, **589**, A59
- Mateos S., et al., 2012, *MNRAS*, **426**, 3271
- Mateos S., et al., 2015, *MNRAS*, **449**, 1422
- Mateos S., et al., 2017, *ApJ*, **841**, L18
- McKinney W., 2010, in van der Walt S., Millman J., eds, *Proceedings of the 9th Python in Science Conference*. pp 51 – 56
- Merloni A., et al., 2014, *MNRAS*, **437**, 3550
- Mullaney J. R., Alexander D. M., Goulding A. D., Hickox R. C., 2011, *MNRAS*, **414**, 1082
- Murphy K. D., Yaqoob T., 2009, *MNRAS*, **397**, 1549
- Nandra K., et al., 2013, preprint, ([arXiv:1306.2307](https://arxiv.org/abs/1306.2307))
- Netzer H., 2015, *ARA&A*, **53**, 365
- Page K. L., O’Brien P. T., Reeves J. N., Turner M. J. L., 2004, *MNRAS*, **347**, 316
- Planck Collaboration 2014, *A&A*, **571**, A16
- Polletta M., et al., 2007, *ApJ*, **663**, 81
- Ptak A., et al., 2015, *ApJ*, **800**, 104
- Puccetti S., et al., 2014, *ApJ*, **793**, 26
- Reynolds C. S., 1999, in Poutanen J., Svensson R., eds, *Astronomical Society of the Pacific Conference Series Vol. 161, High Energy Processes in Accreting Black Holes*. p. 178 ([arXiv:astro-ph/9810018](https://arxiv.org/abs/astro-ph/9810018))
- Ricci C., Paltani S., Ueda Y., Awaki H., 2013a, *MNRAS*, **435**, 1840
- Ricci C., Paltani S., Awaki H., Petrucci P.-O., Ueda Y., Brightman M., 2013b, *A&A*, **553**, A29
- Ricci C., Ueda Y., Paltani S., Ichikawa K., Gandhi P., Awaki H., 2014, *MNRAS*, **441**, 3622
- Ricci C., Ueda Y., Koss M. J., Trakhtenbrot B., Bauer F. E., Gandhi P., 2015, *ApJ*, **815**, L13
- Ricci C., et al., 2016, *ApJ*, **820**, 5
- Ricci C., et al., 2017, *ApJ*, **835**, 105
- Risaliti G., Maiolino R., Salvati M., 1999, *ApJ*, **522**, 157
- Risaliti G., Elvis M., Fabbiano G., Baldi A., Zezas A., Salvati M., 2007, *ApJ*, **659**, L111
- Risaliti G., Young M., Elvis M., 2009, *ApJ*, **700**, L6
- Rivers E., et al., 2015, *ApJ*, **815**, 55
- Shemmer O., Brandt W. N., Netzer H., Maiolino R., Kaspi S., 2006, *ApJ*, **646**, L29
- Shu X. W., Wang J. X., Yaqoob T., Jiang P., Zhou Y. Y., 2012, *ApJ*, **744**, L21
- Stern D., 2015, *ApJ*, **807**, 129
- Stern D., et al., 2012, *ApJ*, **753**, 30
- Teng S. H., et al., 2014, *ApJ*, **785**, 19
- Trakhtenbrot B., et al., 2017, *MNRAS*, **470**, 800
- Ueda Y., et al., 2011, *PASP*, **63**, S937
- Urry C. M., Padovani P., 1995, *PASP*, **107**, 803
- Van Der Walt S., Colbert S. C., Varoquaux G., 2011, preprint, ([arXiv:1102.1523](https://arxiv.org/abs/1102.1523))
- Vito F., Gilli R., Vignali C., Comastri A., Brusa M., Cappelluti N., Iwasawa K., 2014, *MNRAS*, **445**, 3557
- Vito F., et al., 2018, *MNRAS*, **474**, 4528
- Wright E. L., et al., 2010, *AJ*, **140**, 1868
- Wu J., et al., 2012, *ApJ*, **756**, 96

All spectra presented here are plotted with energies in the source observed frame on the lower axis, with the source rest-frame energy shown on the upper axis. Sources with an additional *apex* component included in the spectral fit are shown with a corresponding label in their legend.

The grouping used is annotated on each plot and has one of two possibilities:

- (i) Binning by a minimum number of counts per bin.
- (ii) Binning to have a minimum S/N ratio in each bin.

All sources were fitted with a simplified phenomenological model consisting of photoelectric absorption acting on a composite powerlaw (Γ , the photon index of the powerlaw was assigned to 1.4 for all cases) plus a narrow Gaussian of $\text{FWHM} \approx 2 \text{ eV}$ ($\sigma = 1 \text{ eV}$), modelling the observed continuum and narrow core of the Fe K α fluorescence line, respectively. See Section 3.3 for further details on the spectral model adopted. The corresponding confidence contours shown (where applicable) in the top right panel illustrate a delta statistic of +2.30 to represent the 1- σ (68%) confidence level for two interesting parameters¹³.

All spectra shown feature the spectral fit to the data and the DEL for the fit in the top and bottom panels, respectively. DEL is defined as the (data – model)/error.

¹³ <https://heasarc.gsfc.nasa.gov/xanadu/xspec/manual/XSappendixStatistics.html>

APPENDIX A: SOURCES EXCLUDED

NuSTAR data was not publicly available for 19/55 low redshift sources from the *Neil Gehrels Swift*/BAT sample of Ricci et al. (2015), and so were excluded from this work. See Section 2.2 for more information. This excluded ESO 565-G019, which is in the Gandhi et al. (2014) bona-fide Compton-thick AGN sample, and has been studied individually in Gandhi et al. (2013) with *Suzaku* data.

In addition, our own analysis of the archival archival XMM-*Newton* EPIC/PN spectrum as compared to the more recent *NuSTAR* FPMA & FPMB spectra strongly indicated a changing-look AGN scenario for NGC 4102 and NGC 4939. These sources were thus excluded since changing-look AGN could adhere to variable obscuration effects.

Finally, 5 sources had observed rest-frame 2-10 keV fluxes in agreement with the interpolated rest-frame 12 μm flux, predicted from the relation presented in Asmus et al. (2015). These 5 sources were ruled out from our sample, and their spectra are shown in Figure A1.

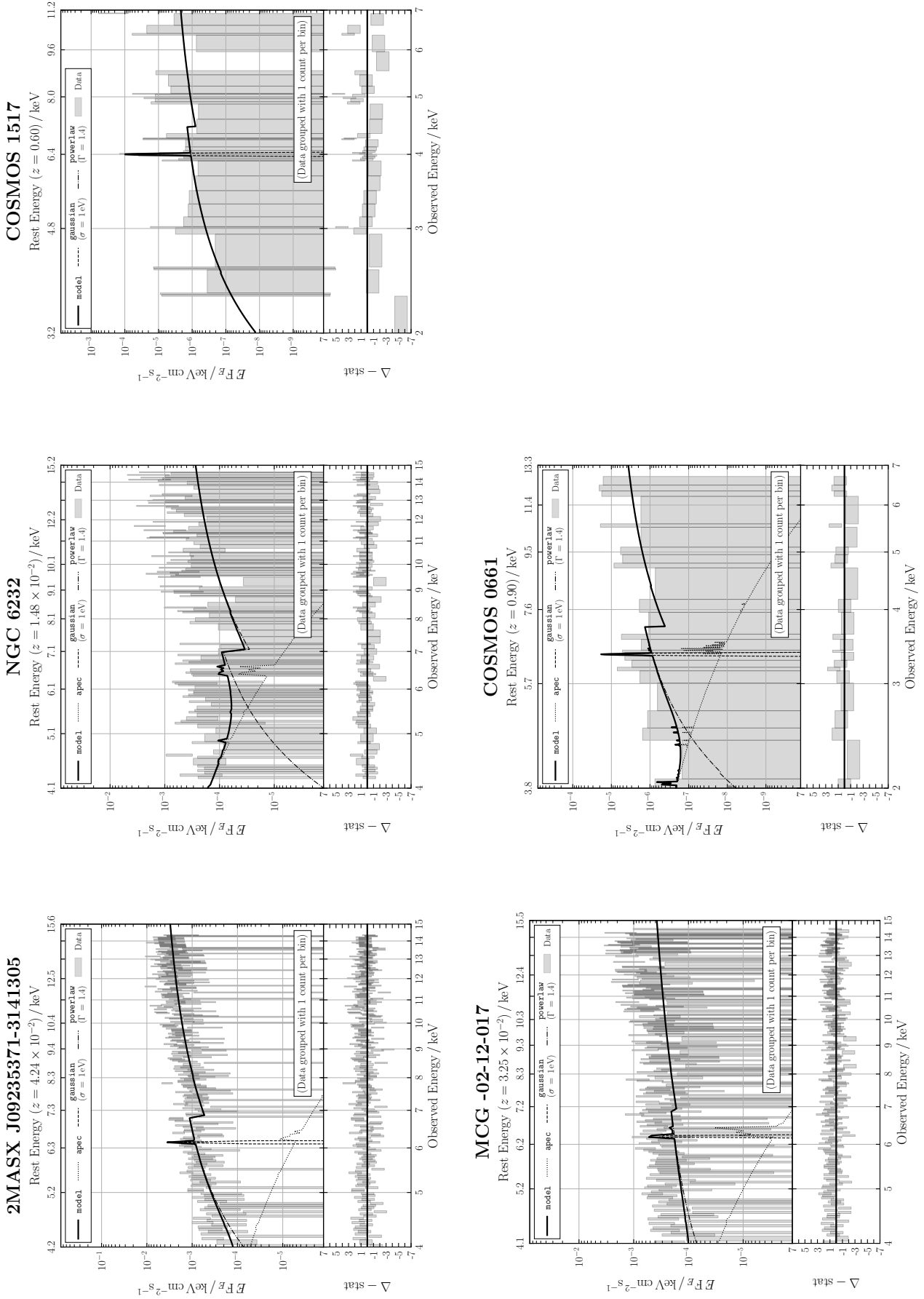
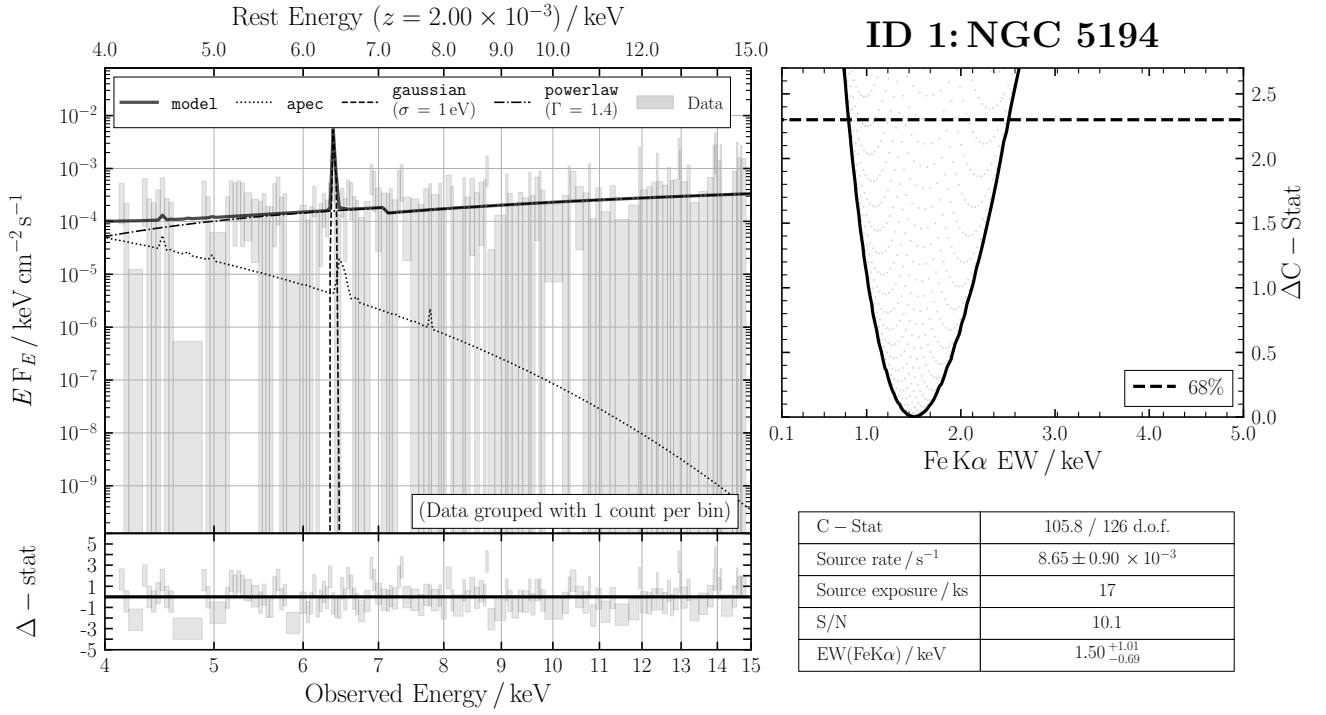


Figure A1. Spectra of the 5 sources ruled out in our analysis due to an agreement with the [Asmus et al. \(2015\)](#) correlation between observed X-ray and mid-infrared luminosity, which can infer less than Compton-thick obscuration. For details of the spectrum, see the description at the start of the Appendix. The top and bottom panels show the spectral fit to the data and the DEL for the fit, respectively. DEL is defined as the $(\text{data} - \text{model})/\text{error}$.

APPENDIX B: SOURCES INCLUDED

Here we include individual spectra and equivalent width (EW) contours for the sources we derive EWs for ourselves. The sources are ordered in ascending $12\mu\text{m}$ luminosity, as in Table 1 of the paper. We used the limit derived from best-fit parameters for 3 sources that the contour method did not provide a reasonable constraint for. These sources are: COSMOS0581, COSMOS 0987 and CDFS 460. Furthermore, due to an unphysical EW determined for CDFS 443, CDFS 454 and COSMOS 2180, we fixed the EW for these sources to be $< 5\text{ keV}$.

The upper right panel for each source figure indicates the contour plot for the EW, with the grid best-fit values shown as faint grey points. Statistical details of the spectral fit are tabulated in the bottom right panel of each source figure. All uncertainties shown from the intersection of the horizontal black line with the solid line contour correspond to the 68% confidence level for two interesting parameters.

**Figure B1.** ID 1: NGC 5194

This paper has been typeset from a \LaTeX file prepared by the author.

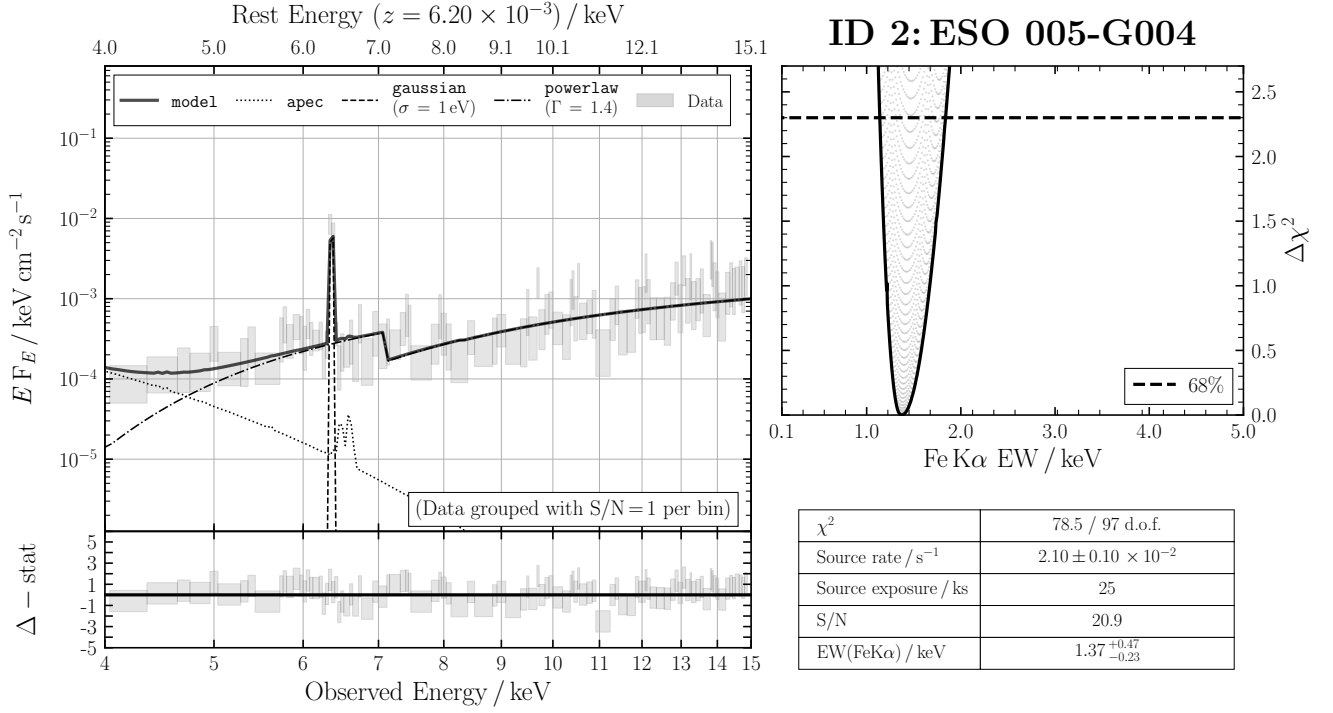


Figure B2. ID 2: ESO 005-G004

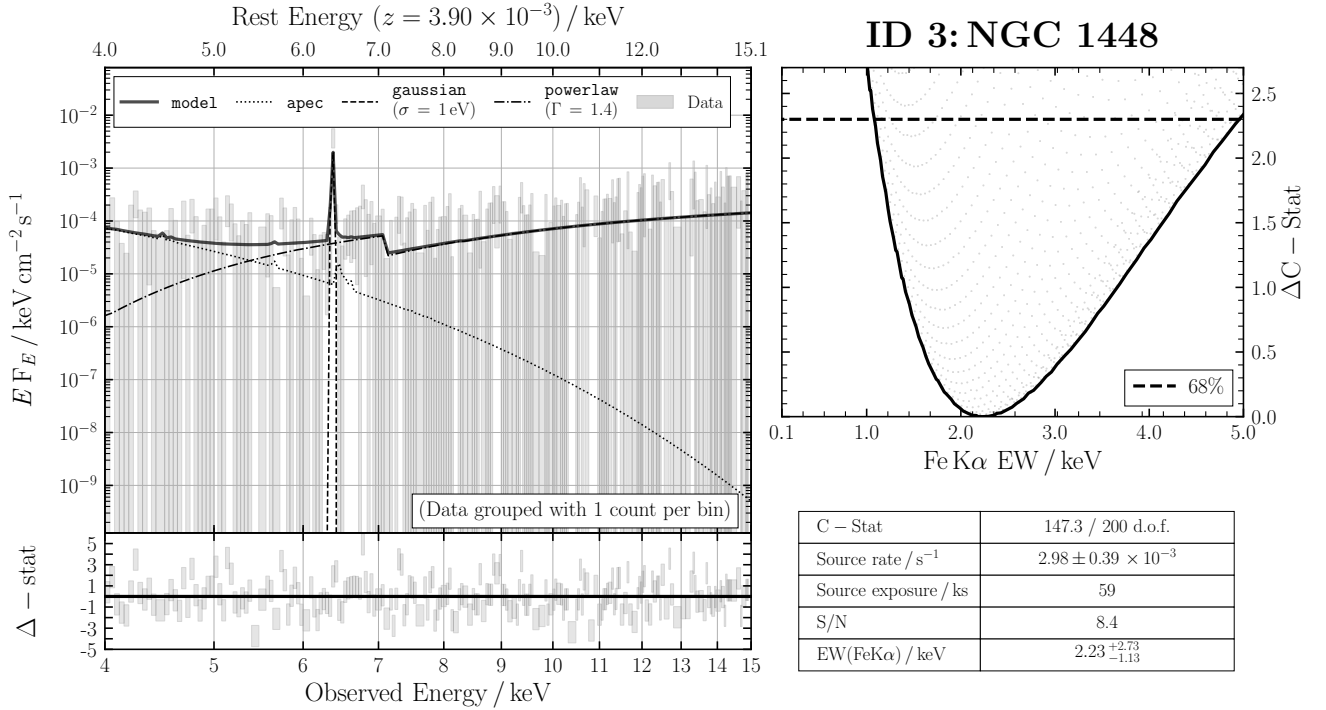
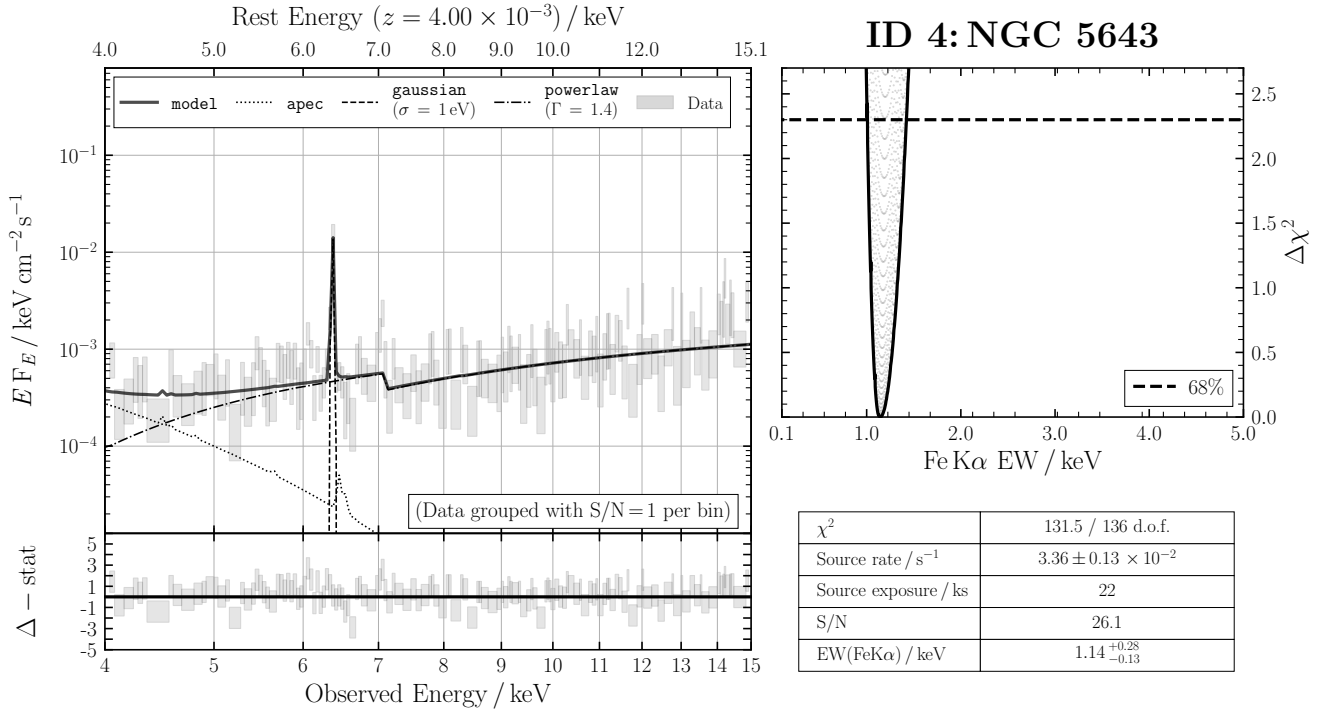
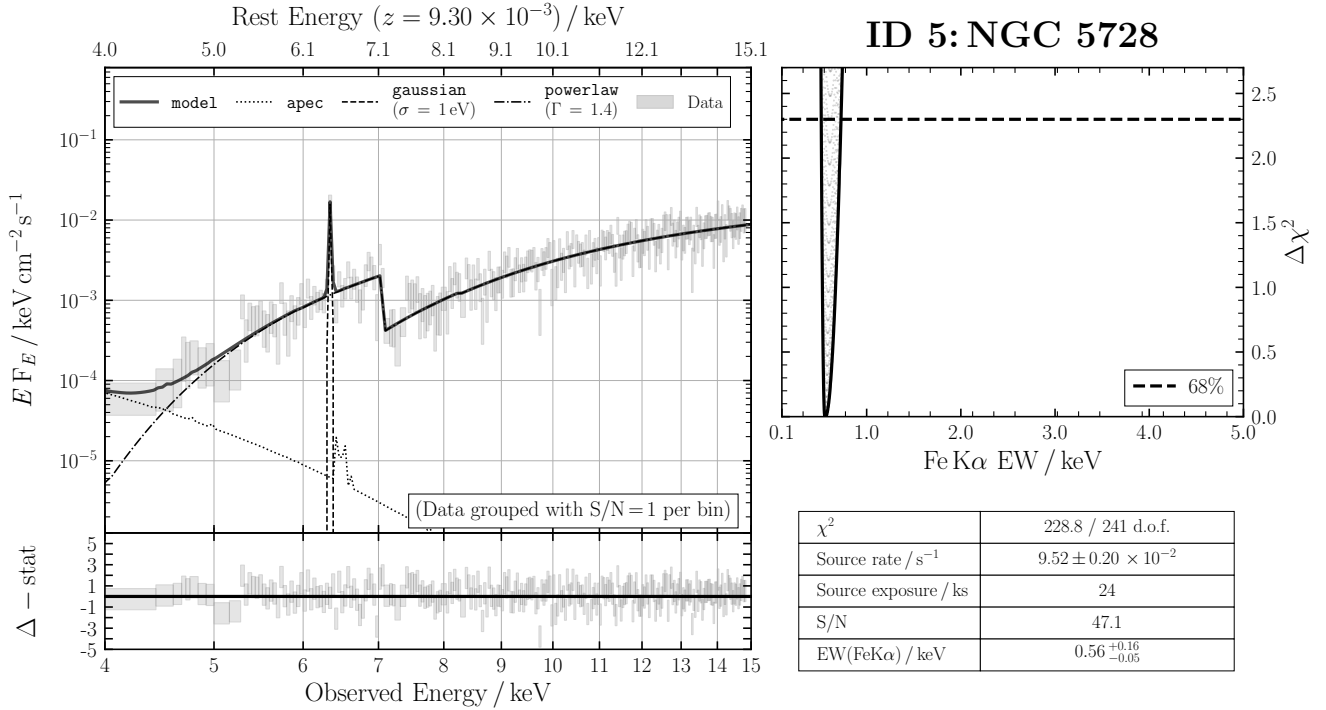


Figure B3. ID 3: NGC 1448

**Figure B4.** ID 4: NGC 5643**Figure B5.** ID 5: NGC 5728

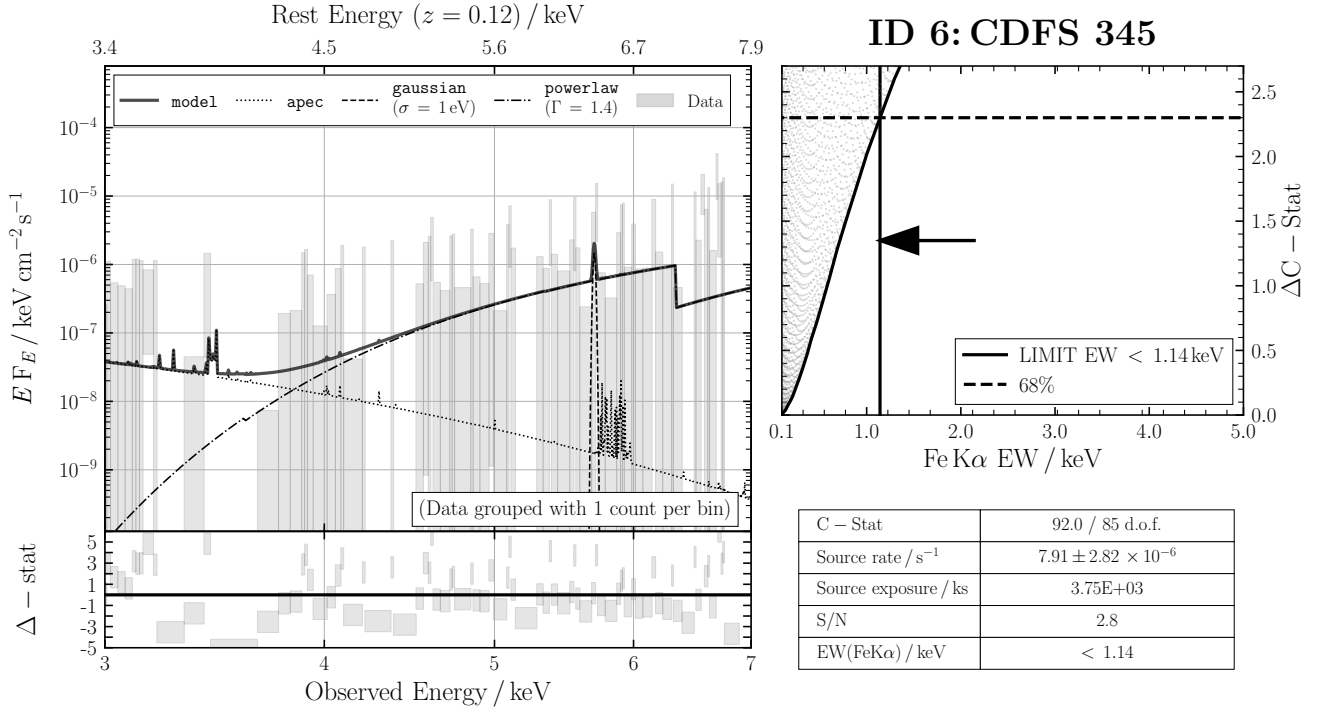


Figure B6. ID 6: CDFS 345

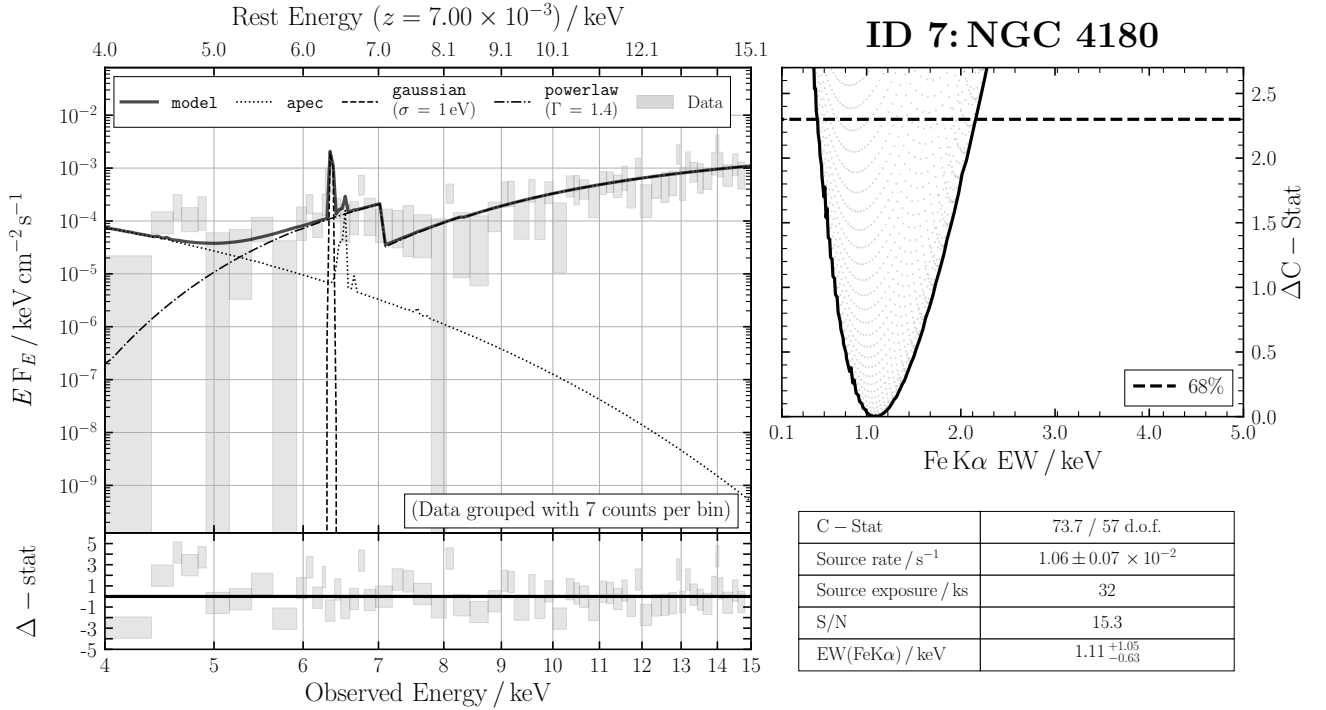
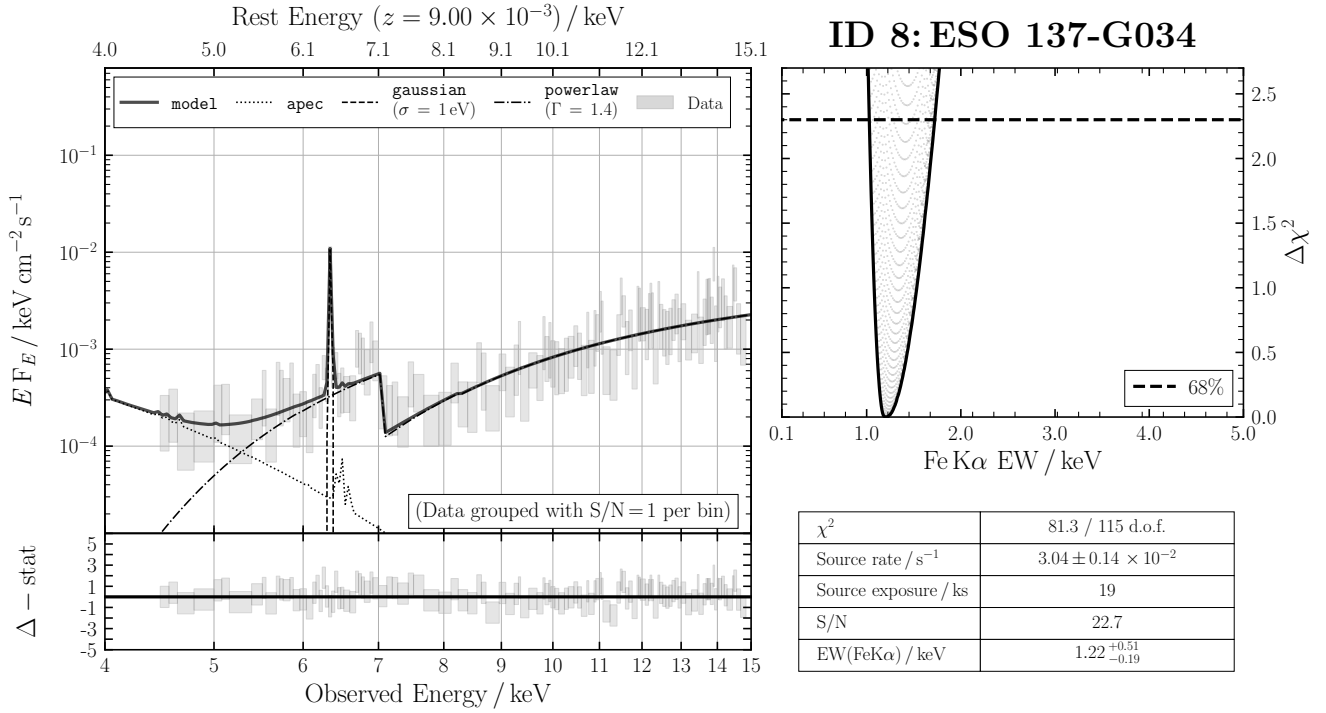
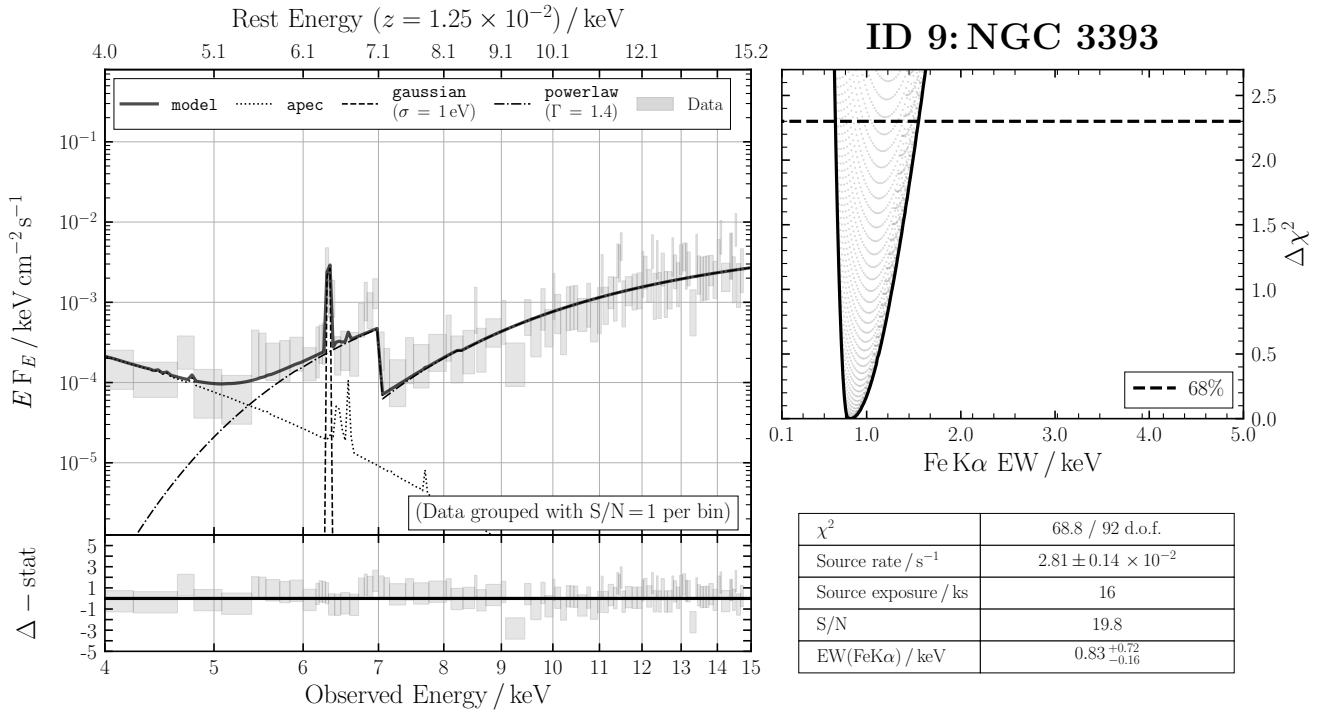


Figure B7. ID 7: NGC 4180

**Figure B8.** ID 8: ESO 137-G034**Figure B9.** ID 9: NGC 3393

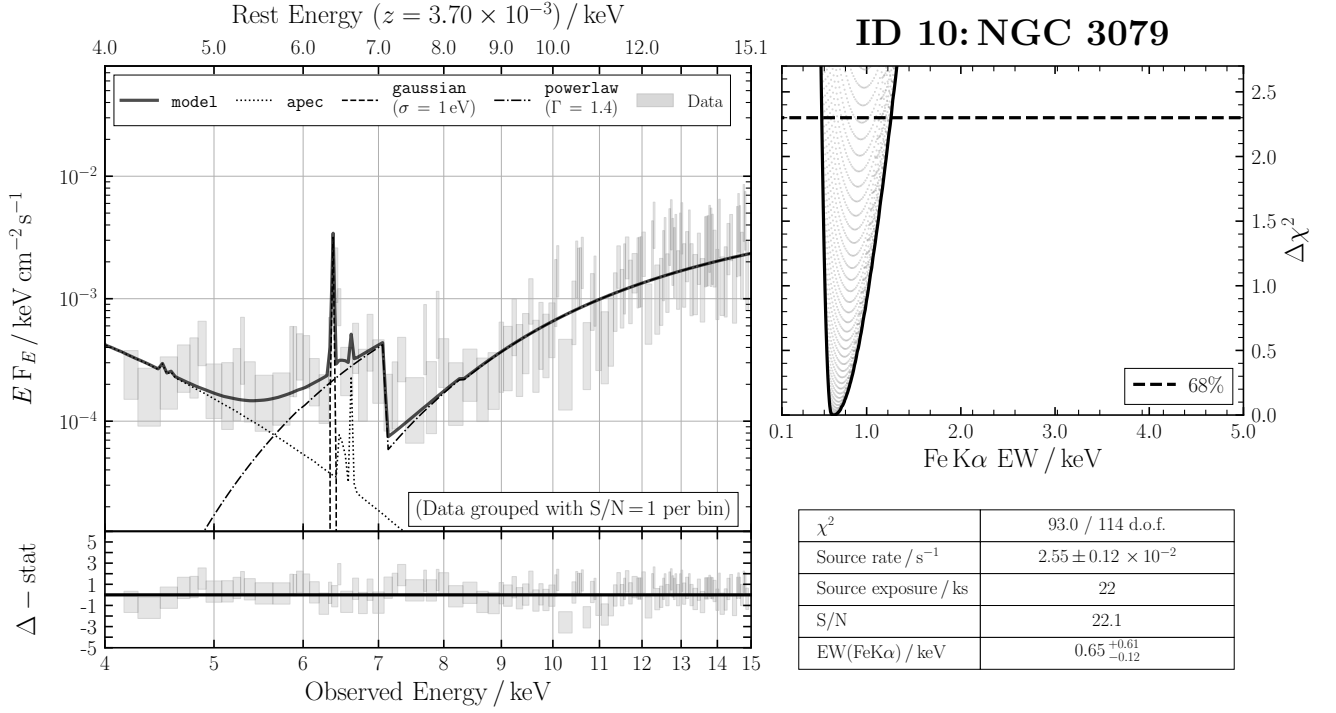


Figure B10. ID 10: NGC 3079

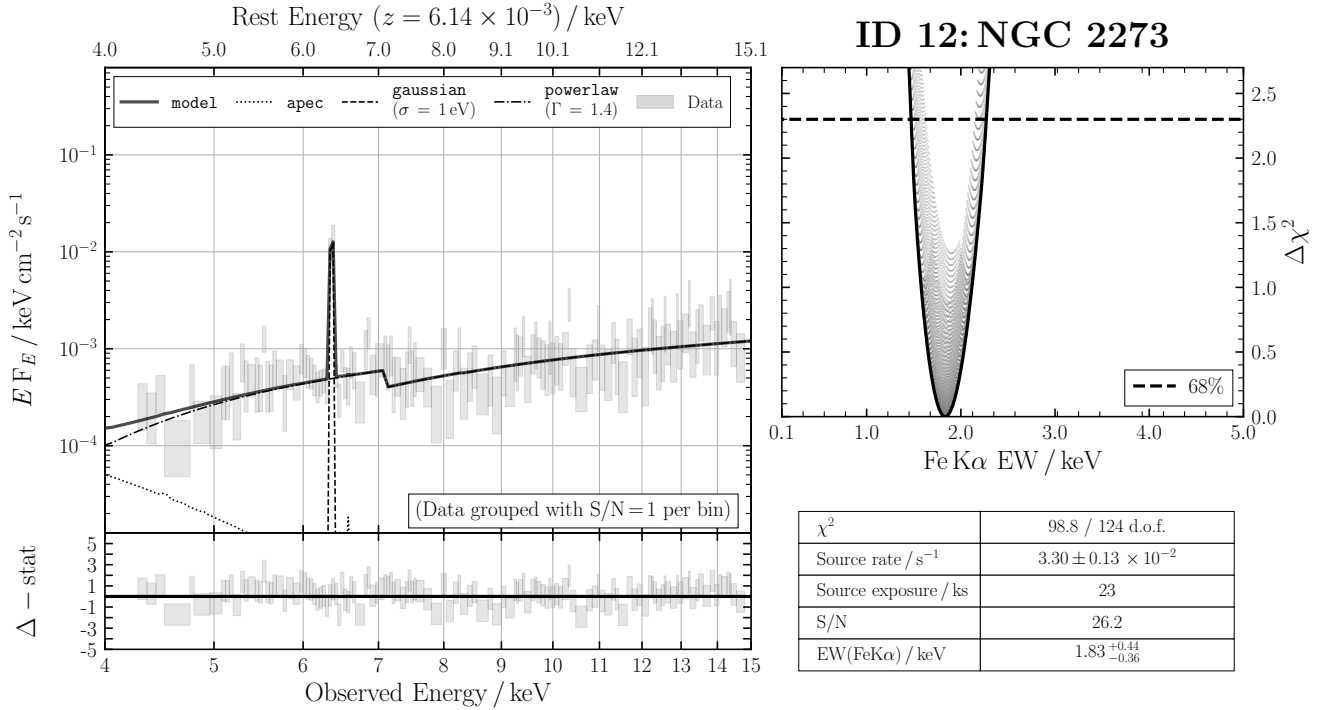
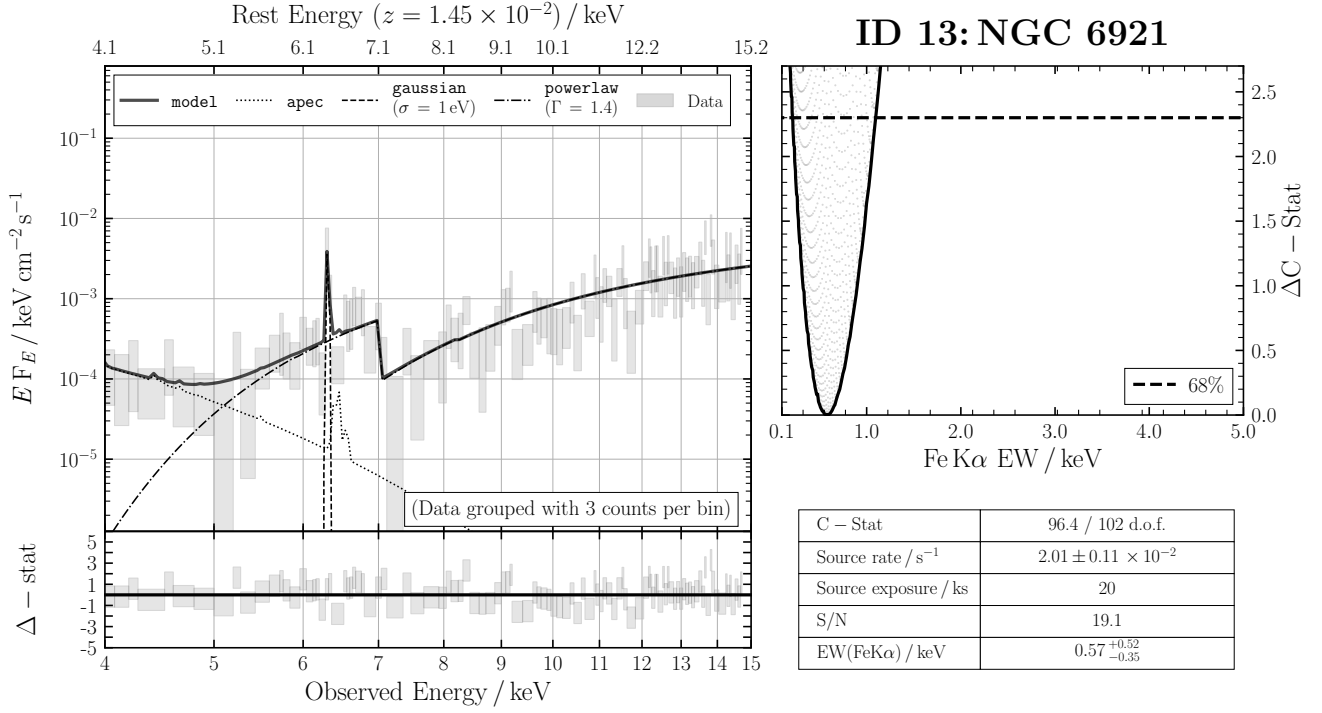
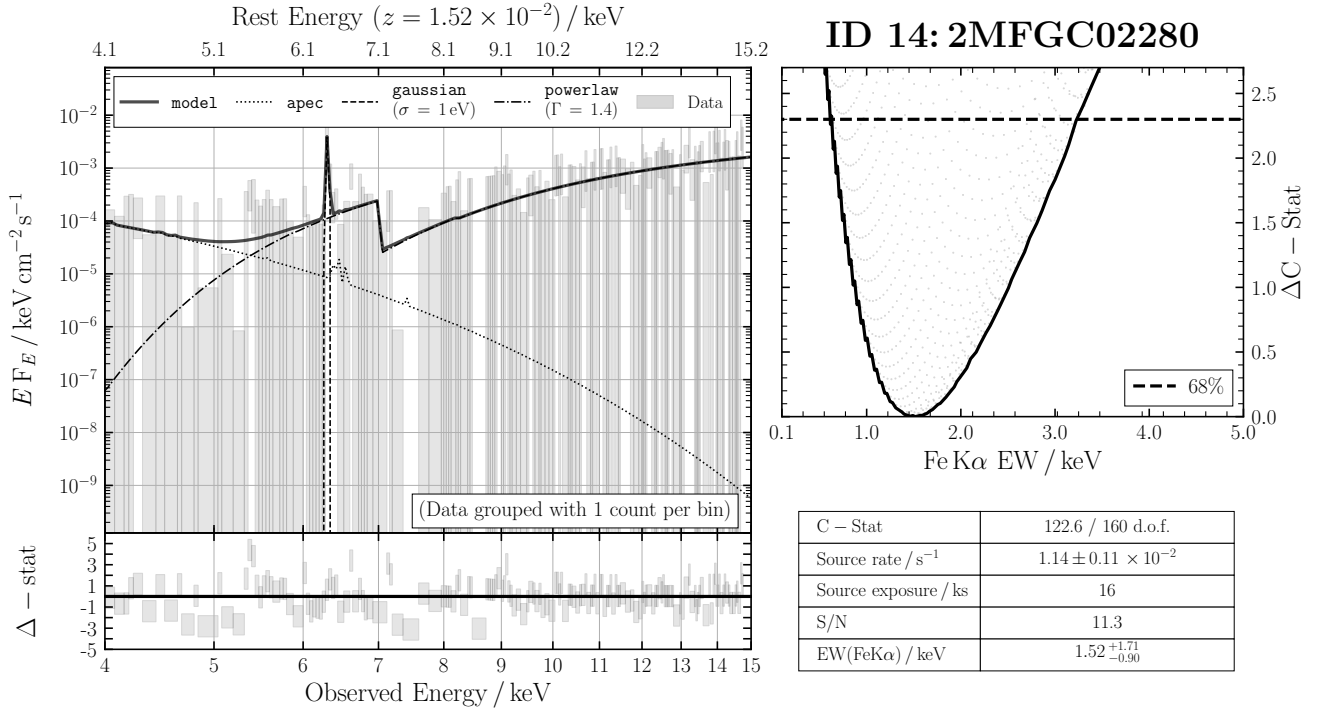


Figure B11. ID 12: NGC 2273

**Figure B12.** ID 13: NGC 6921**Figure B13.** ID 14: 2MFGC02280

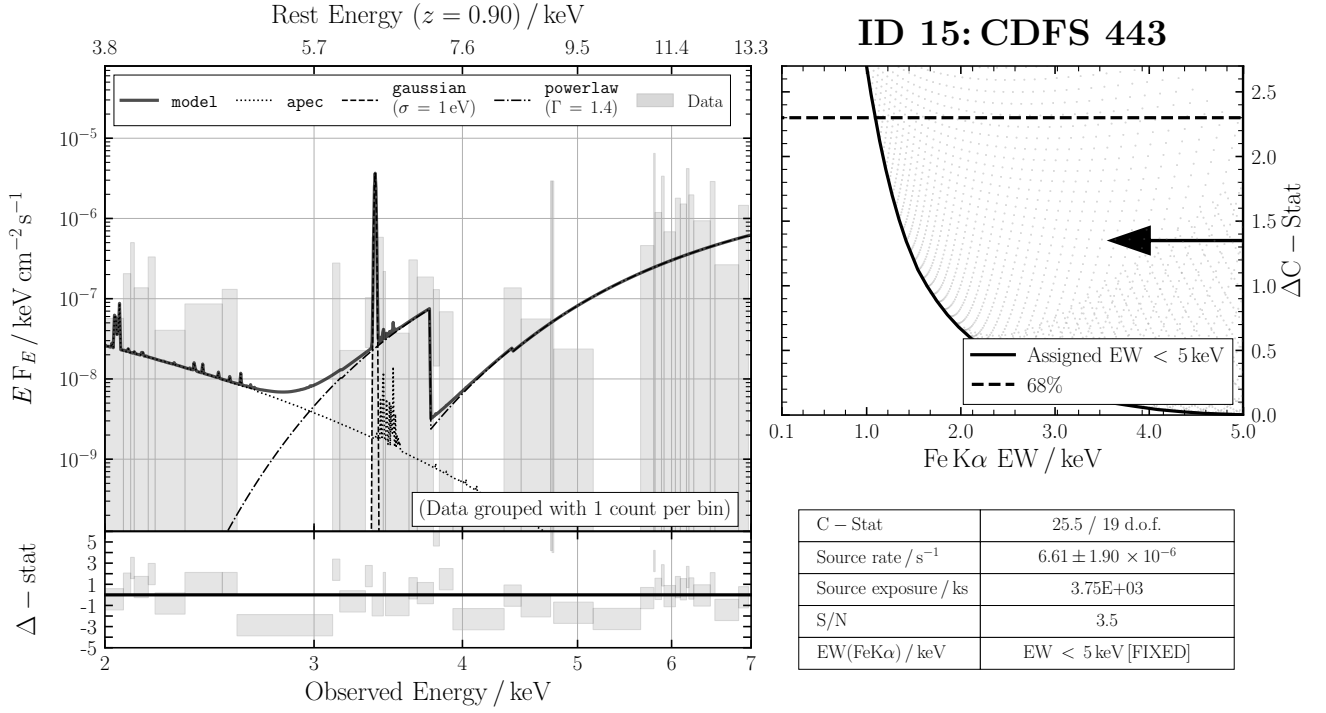


Figure B14. ID 15: CDFS 443

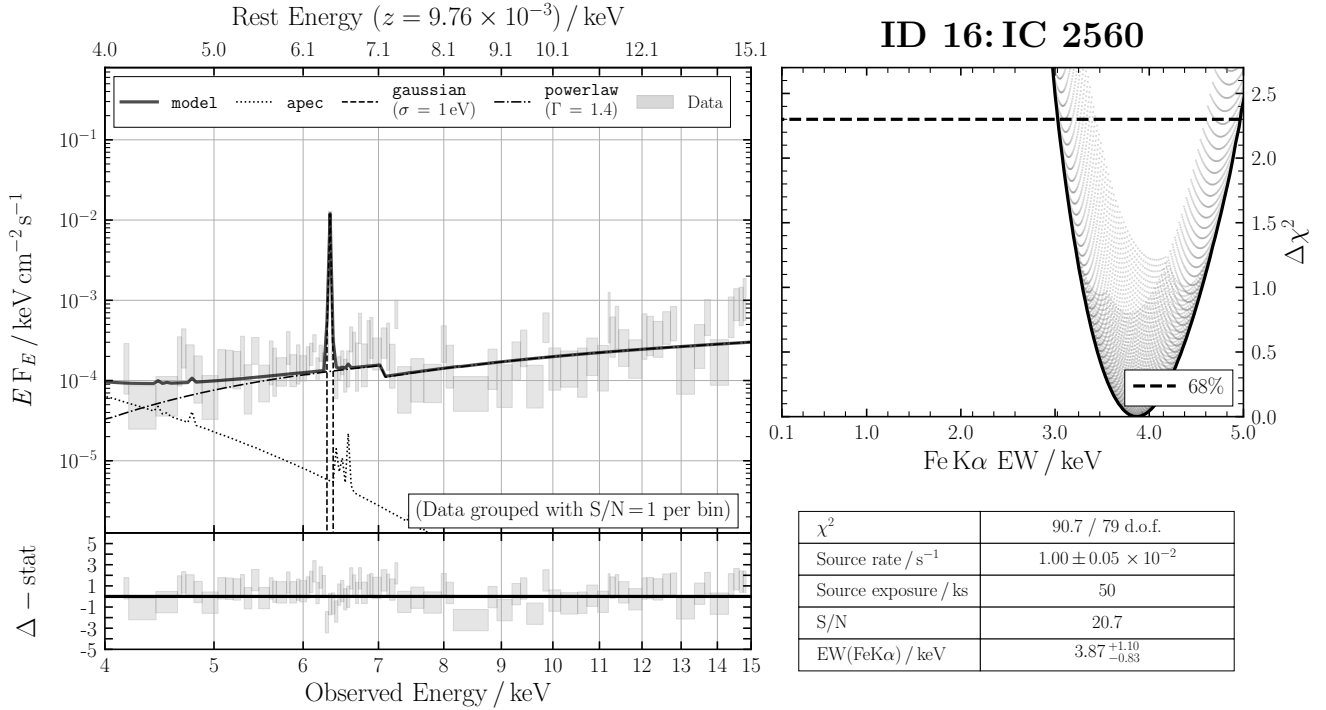
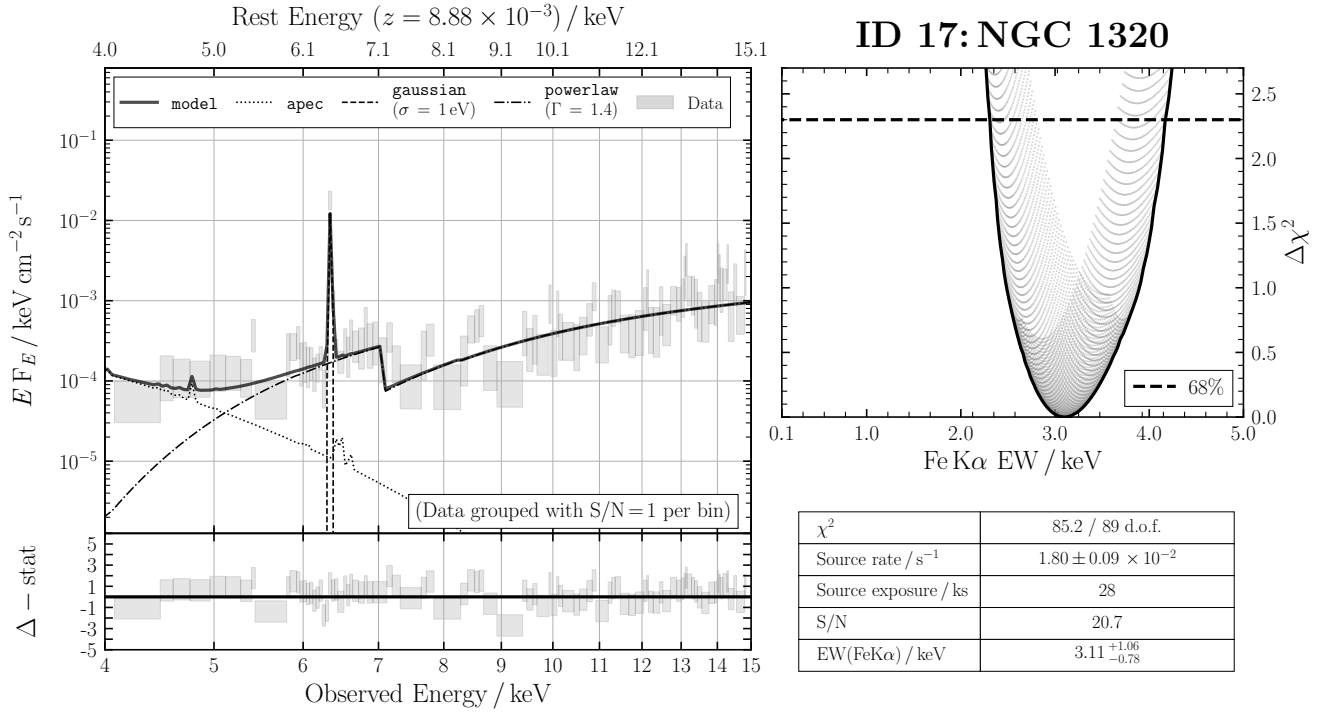
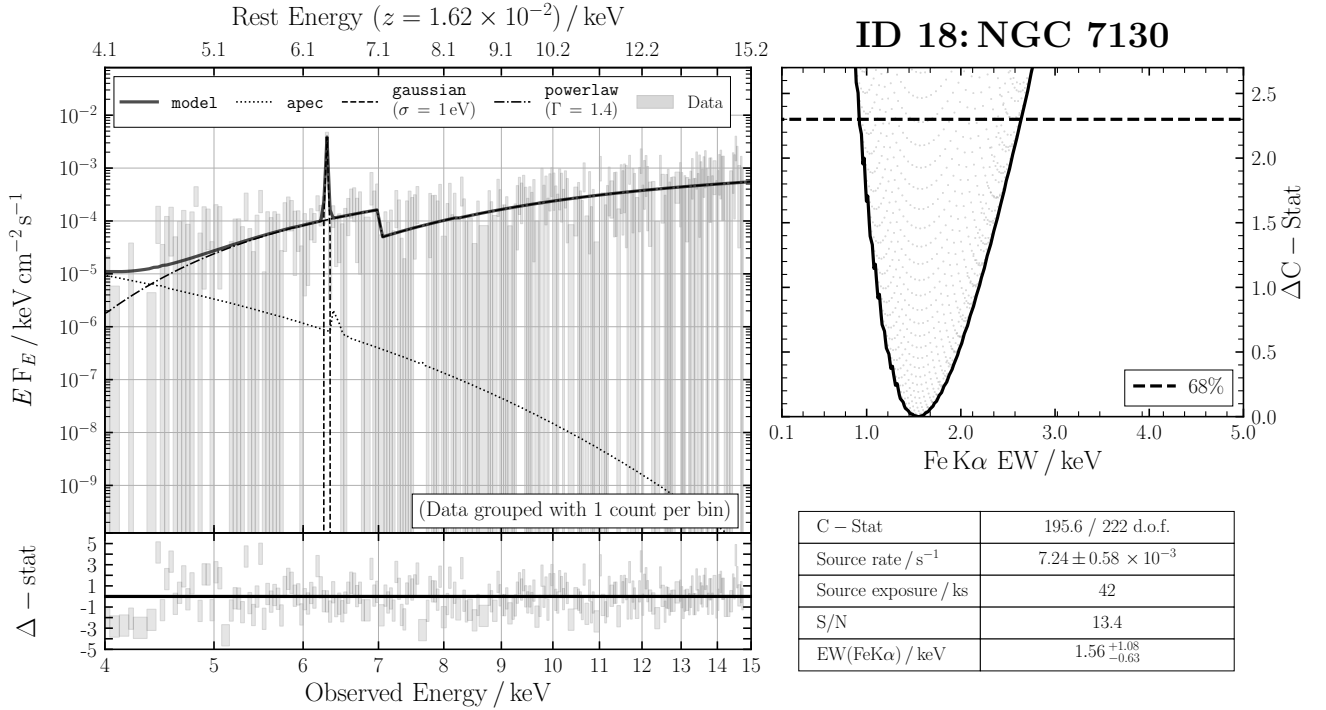


Figure B15. ID 16: IC 2560

**Figure B16.** ID 17: NGC 1320**Figure B17.** ID 18: NGC 7130

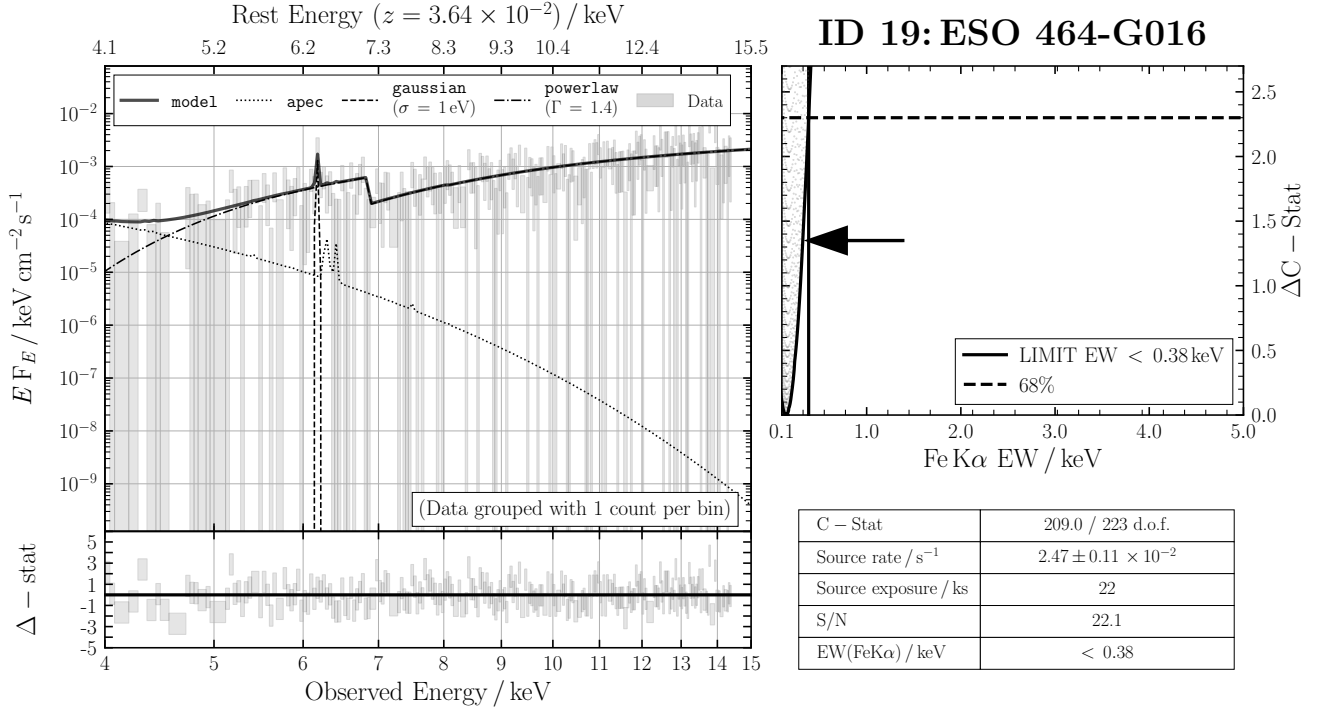


Figure B18. ID 19: ESO 464-G016

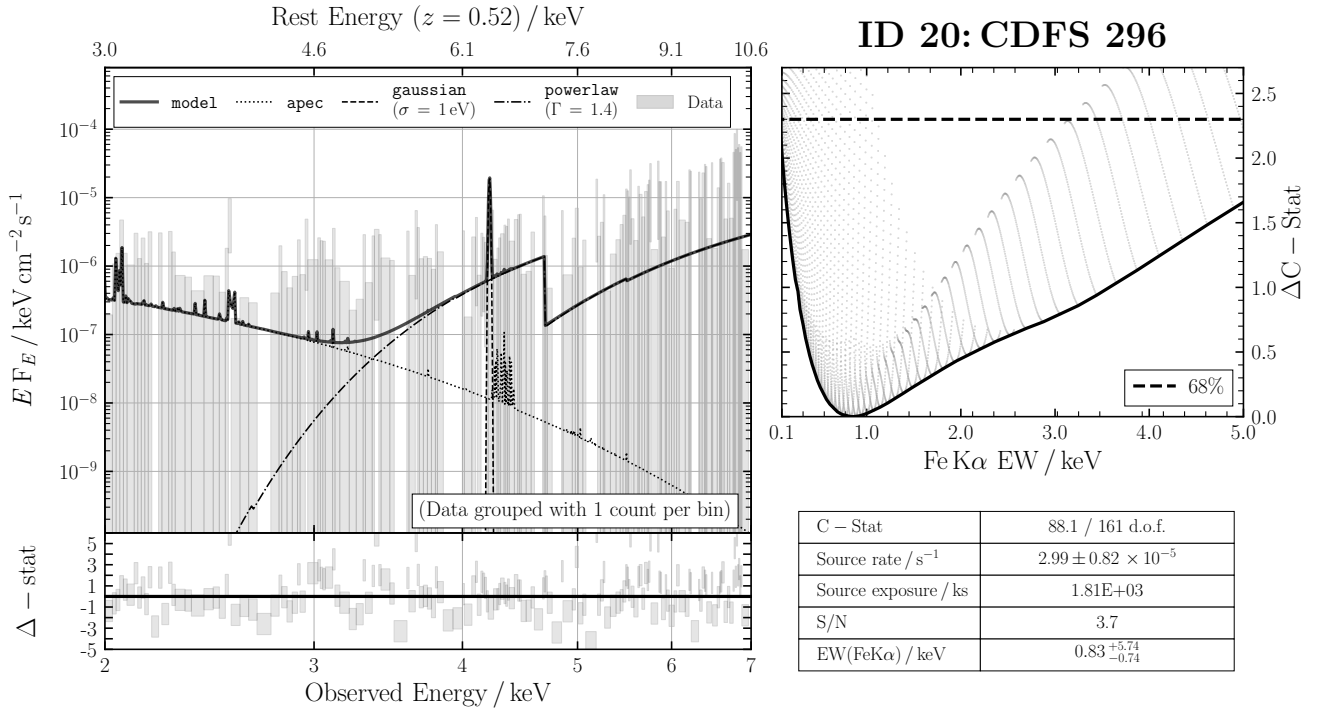
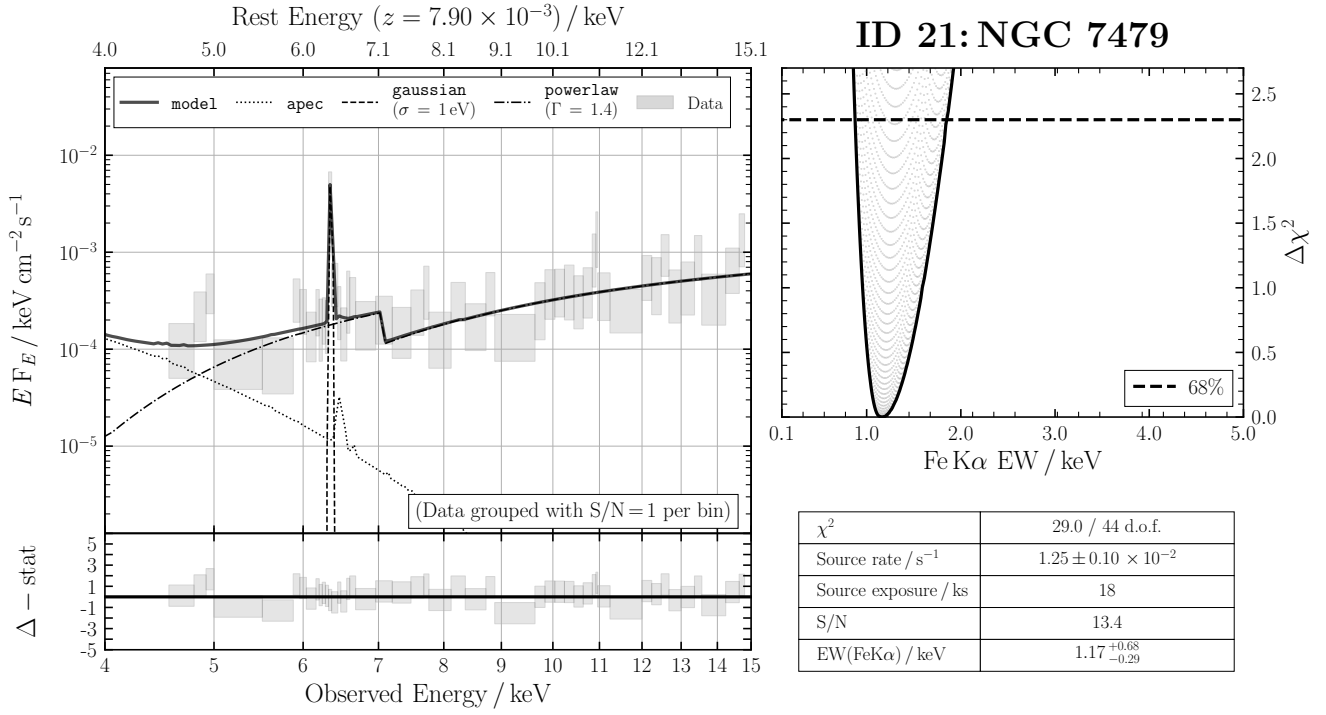
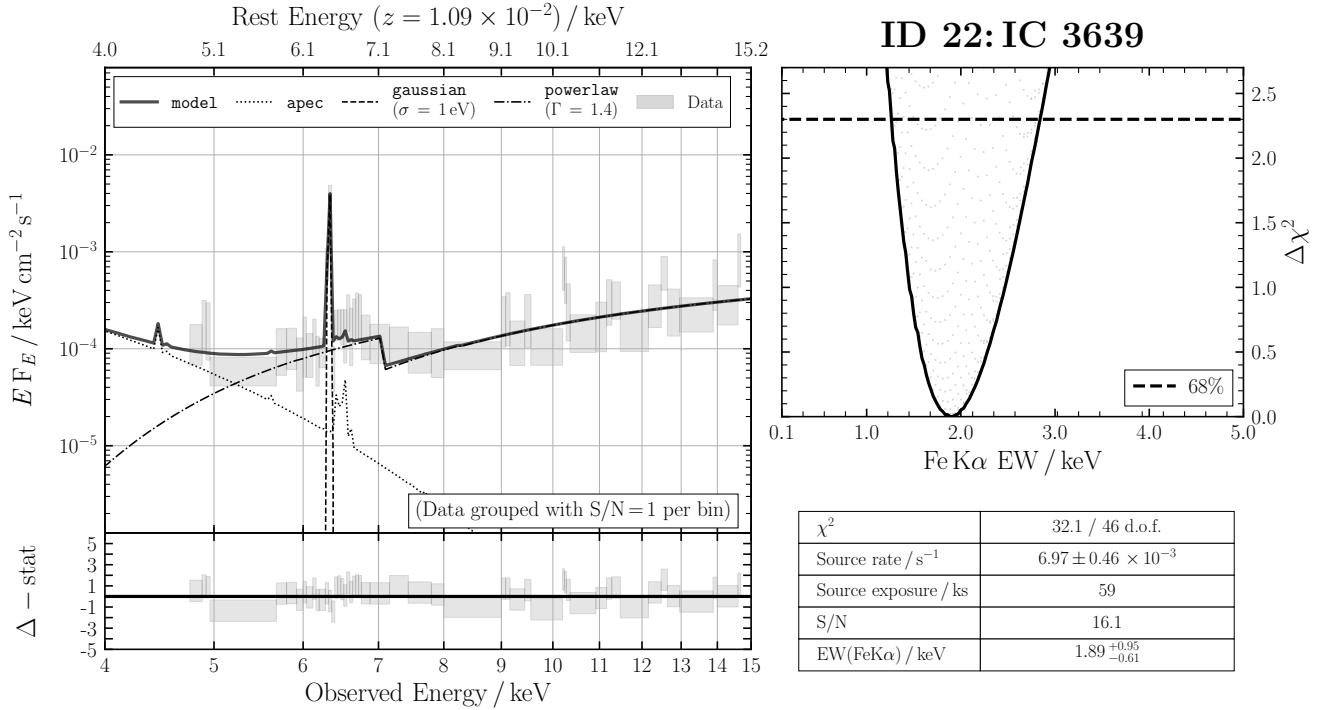


Figure B19. ID 20: CDFS 296

**Figure B20.** ID 21: NGC 7479**Figure B21.** ID 22: IC 3639

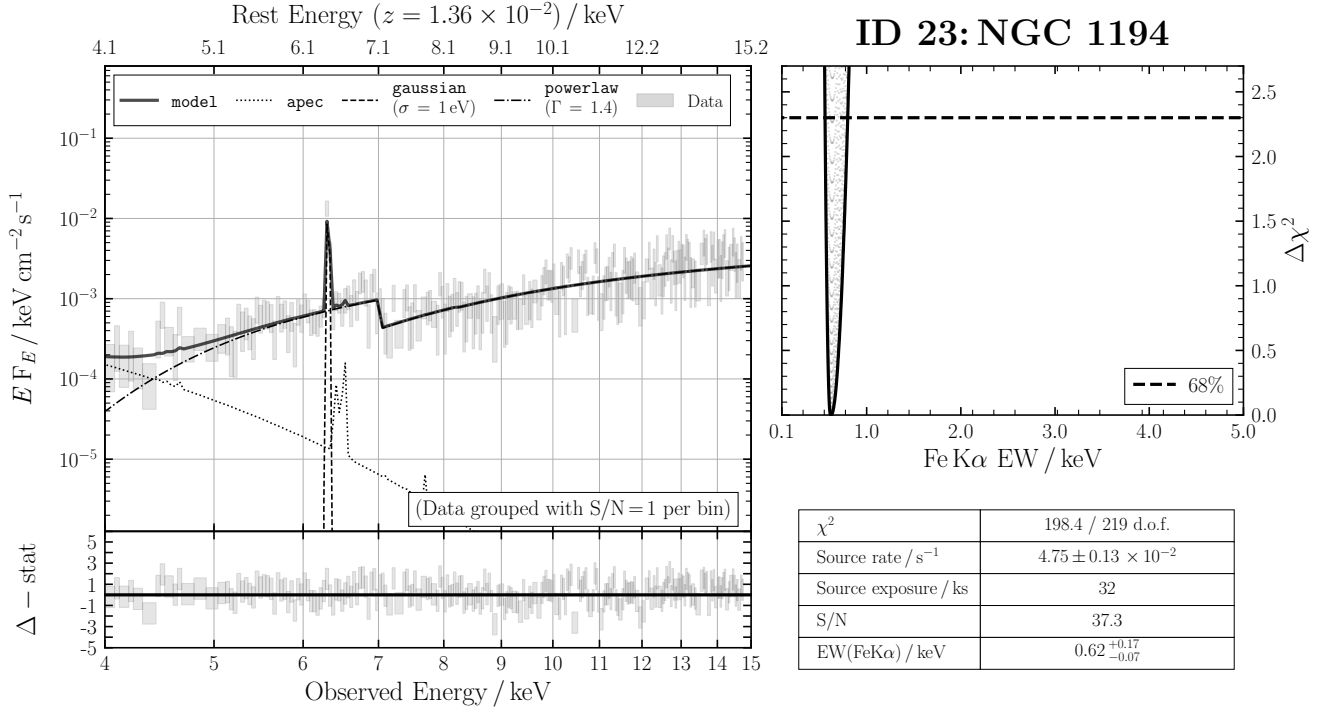


Figure B22. ID 23: NGC 1194

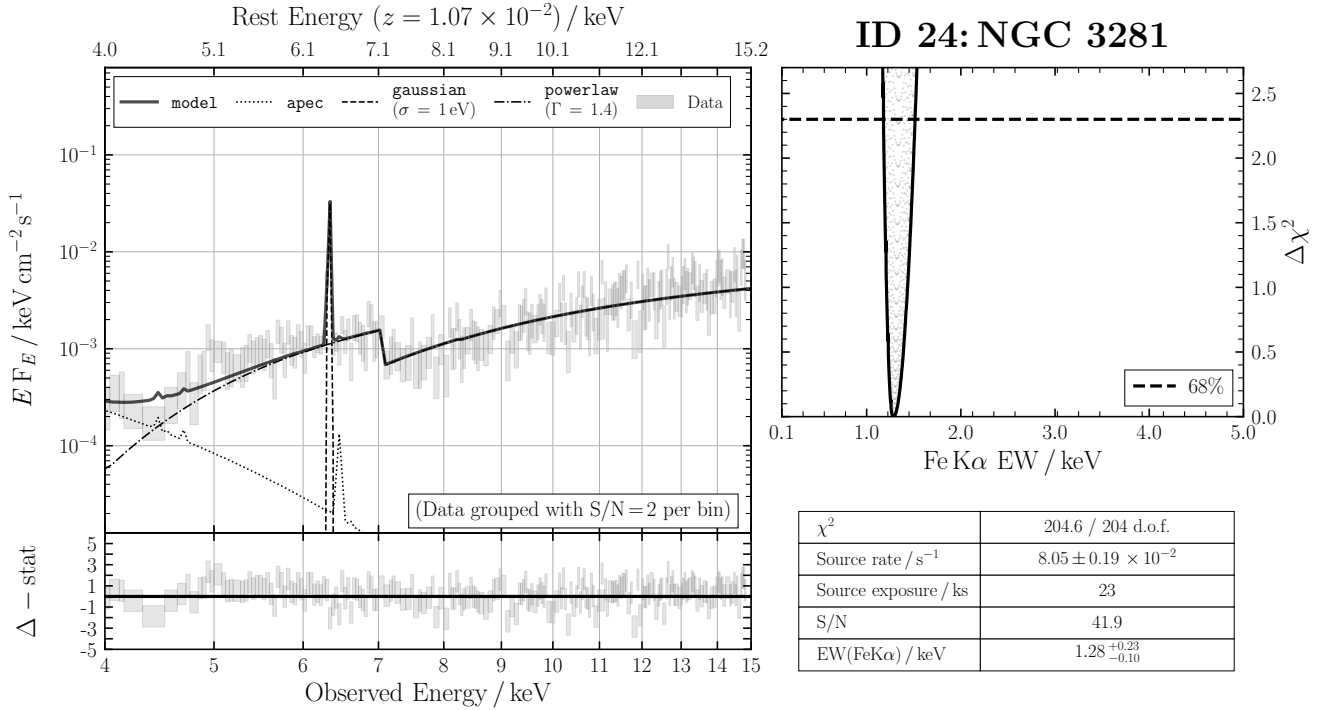
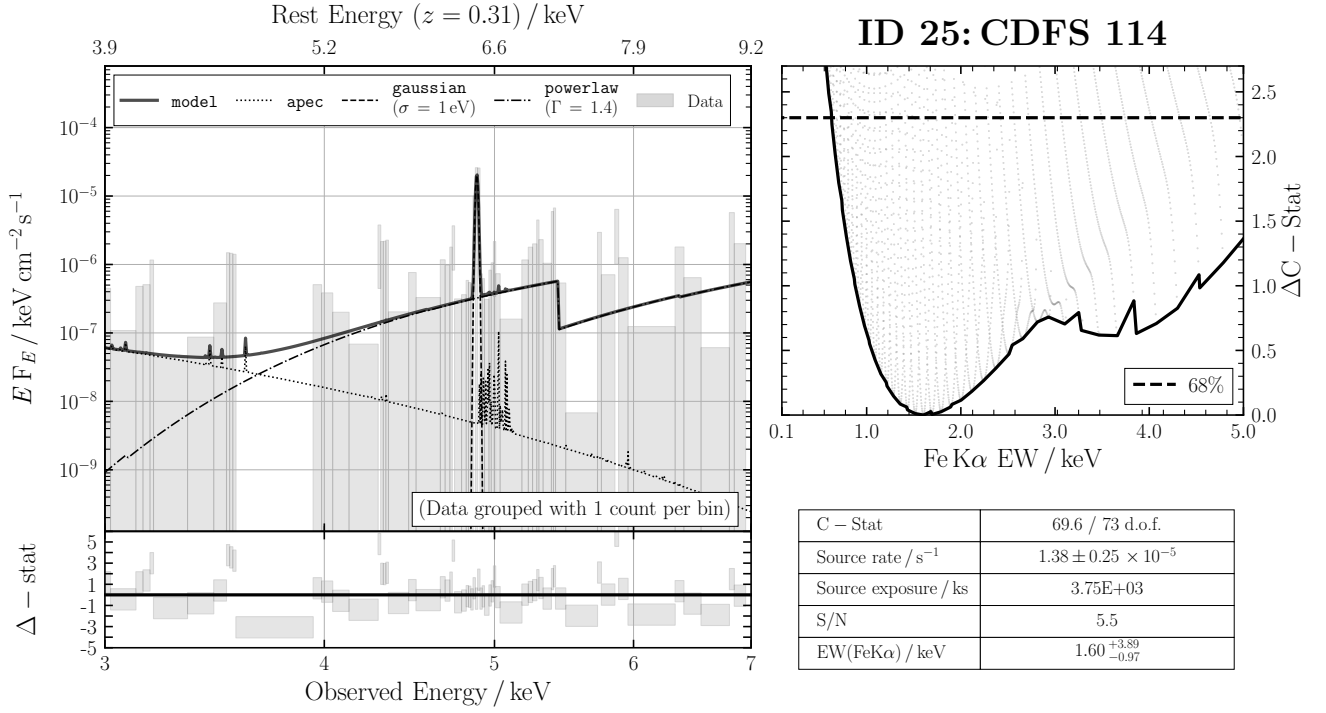
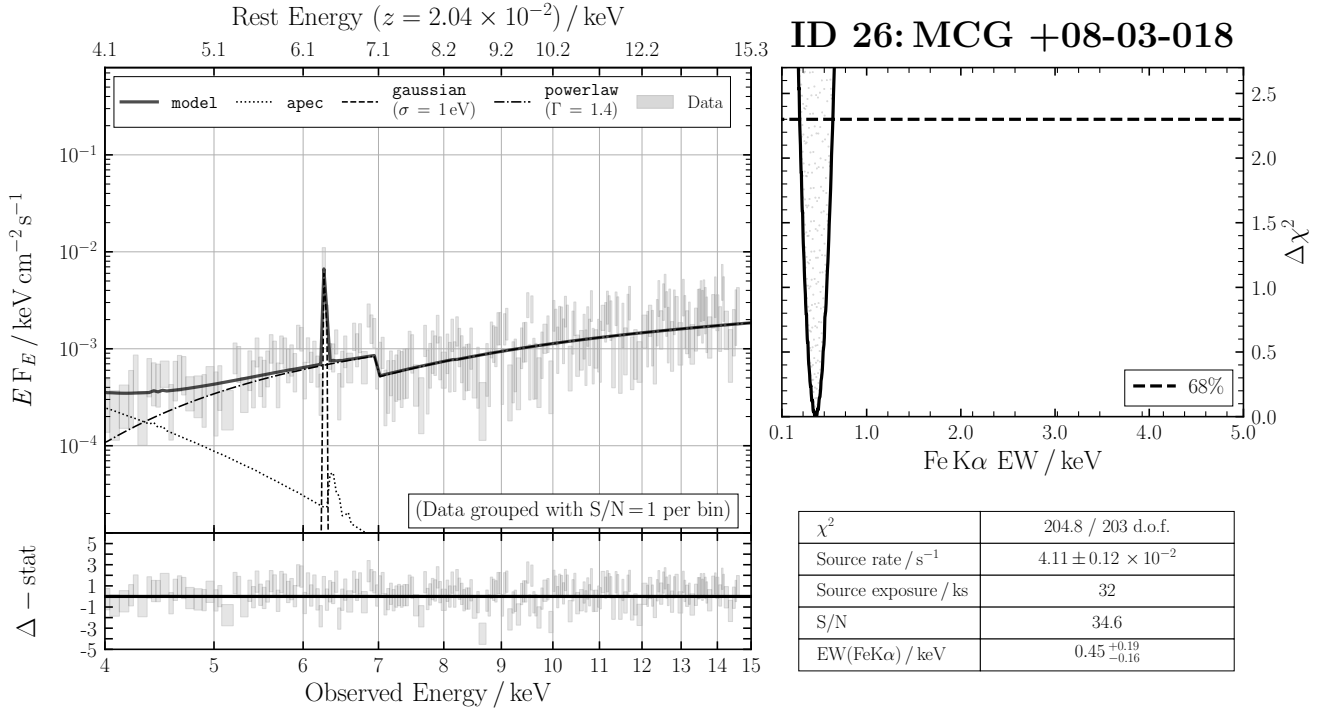


Figure B23. ID 24: NGC 3281

**Figure B24.** ID 25: CDFS 114**Figure B25.** ID 26: MCG +08-03-018

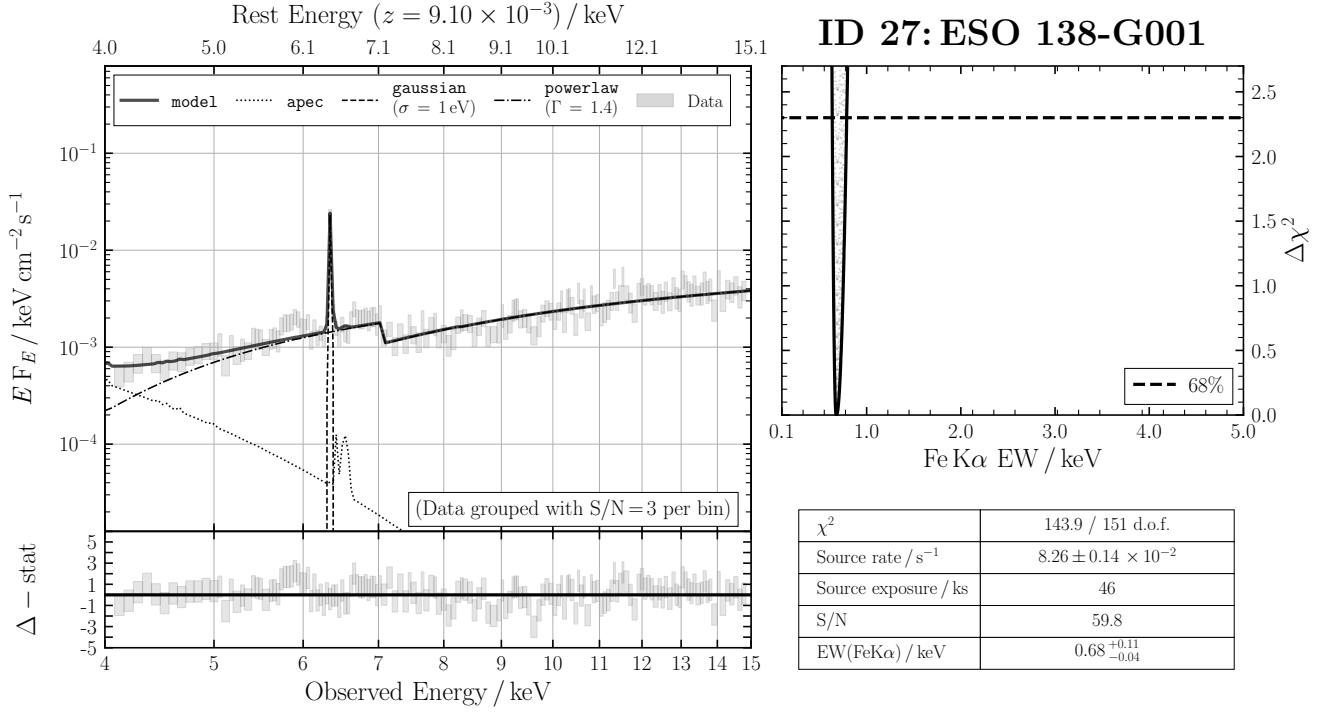


Figure B26. ID 27: ESO 138-G001

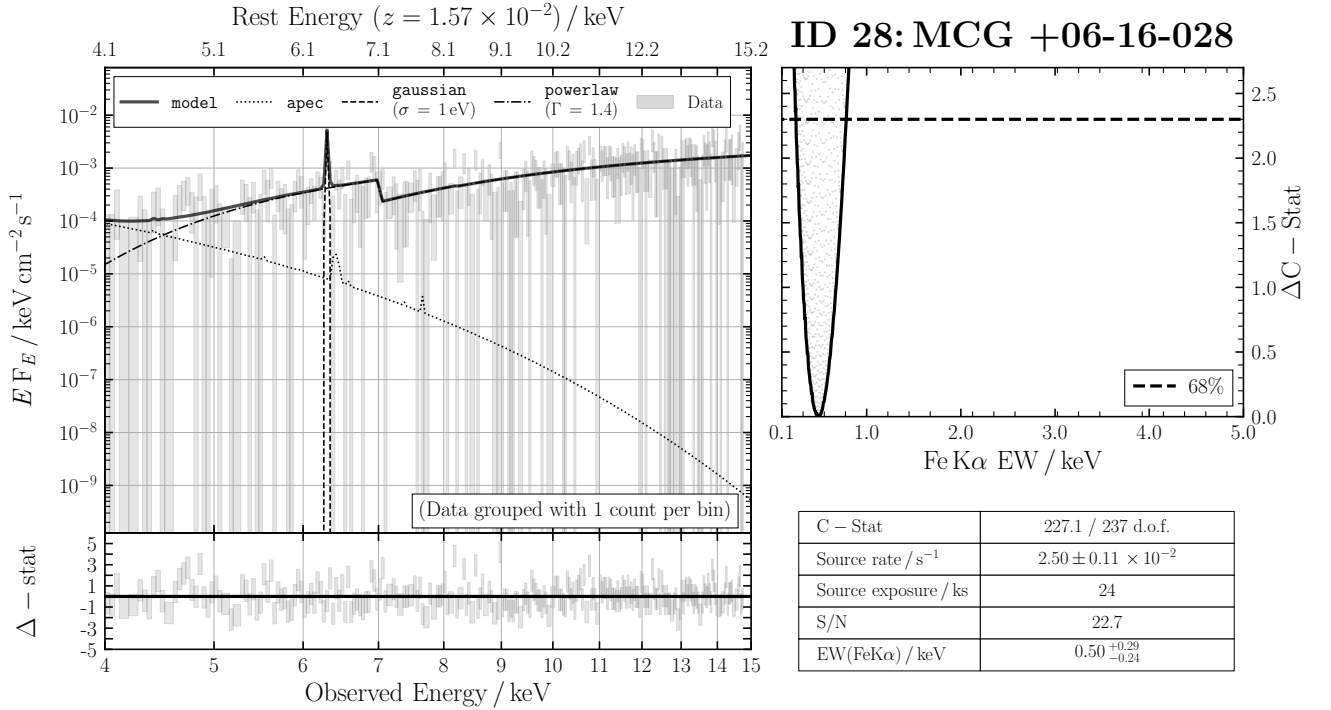
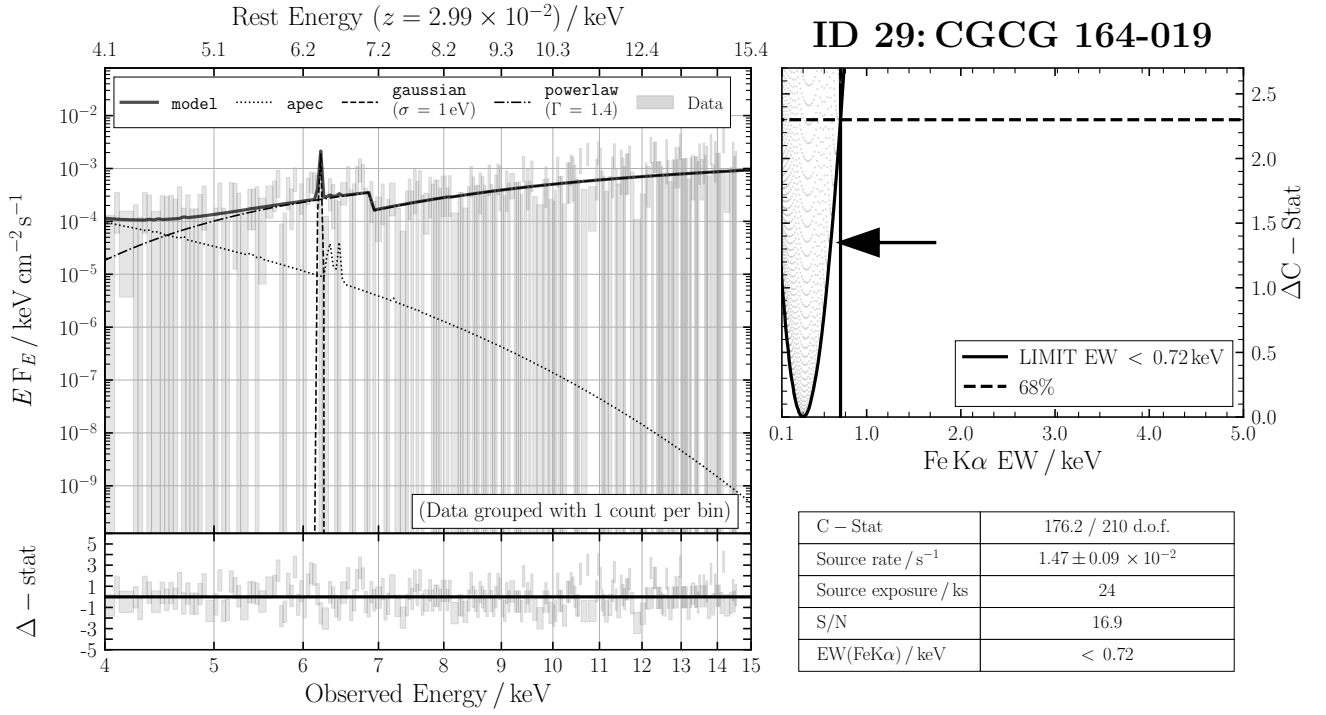
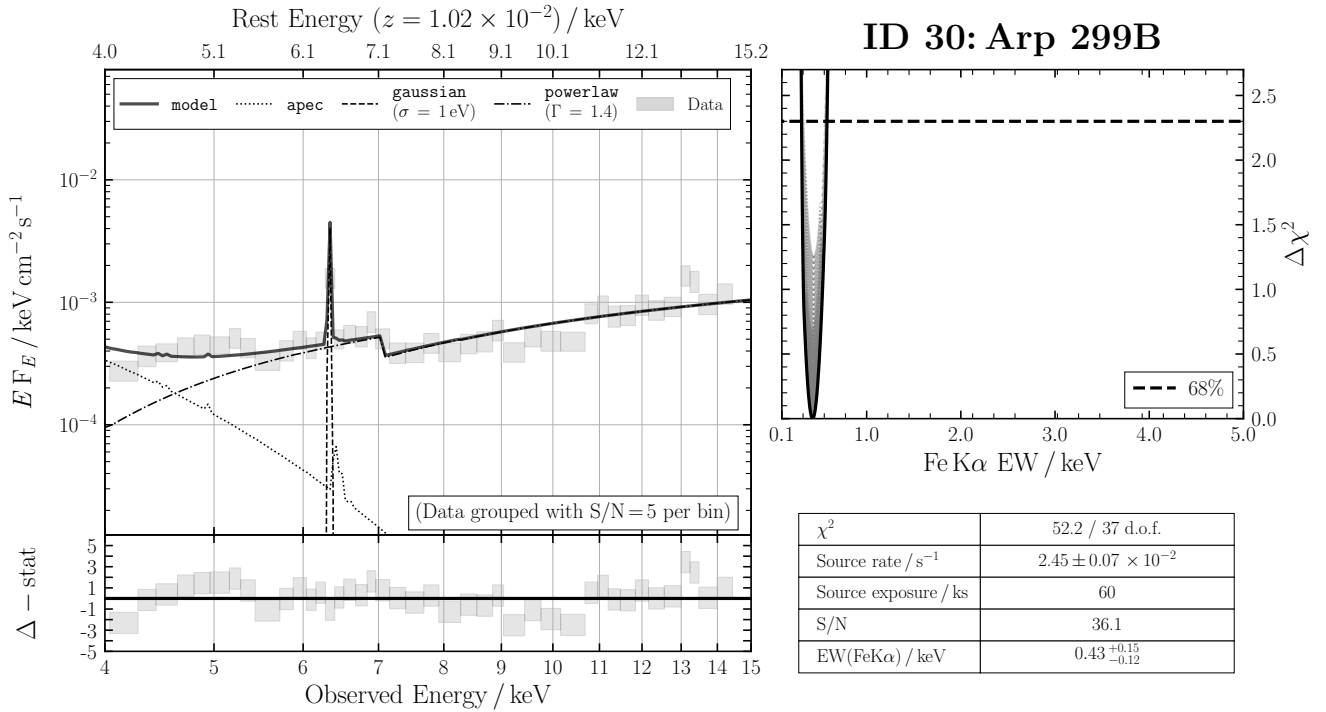


Figure B27. ID 28: MCG +06-16-028

**Figure B28.** ID 29: CGCG 164-019**Figure B29.** ID 30: Arp 299B

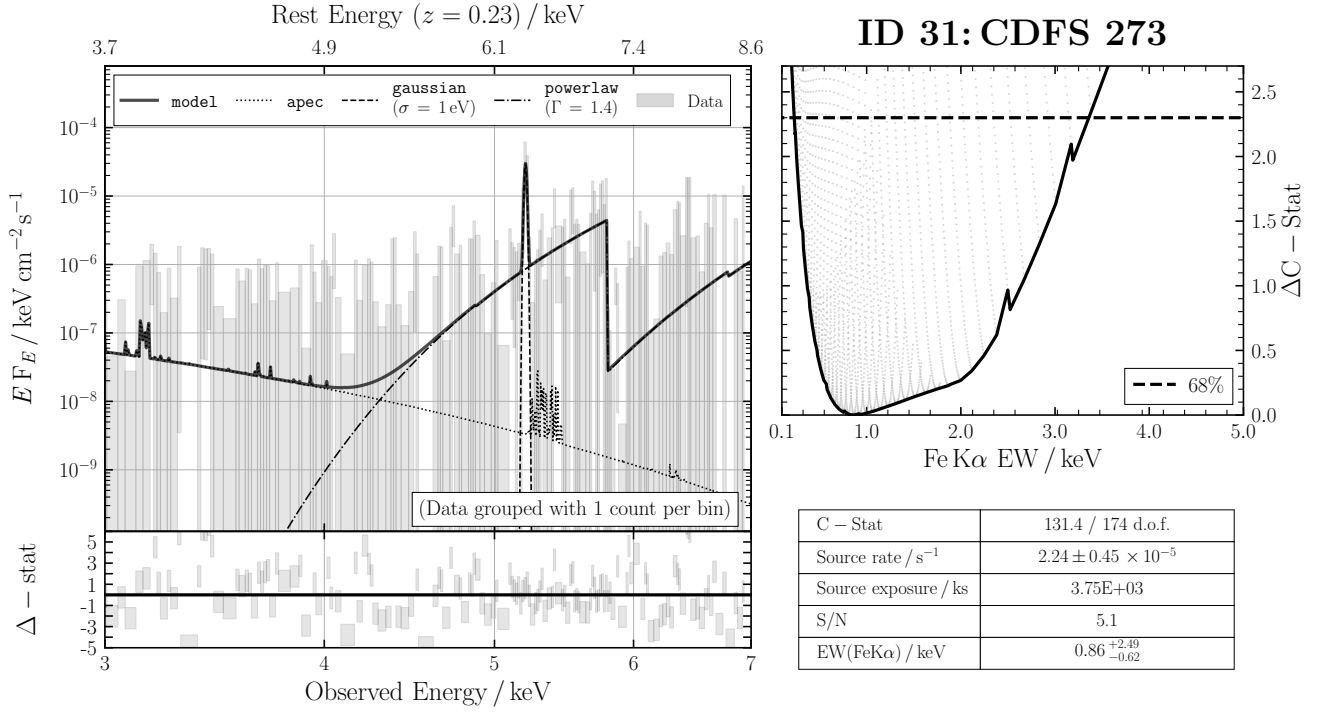


Figure B30. ID 31: CDFS 273

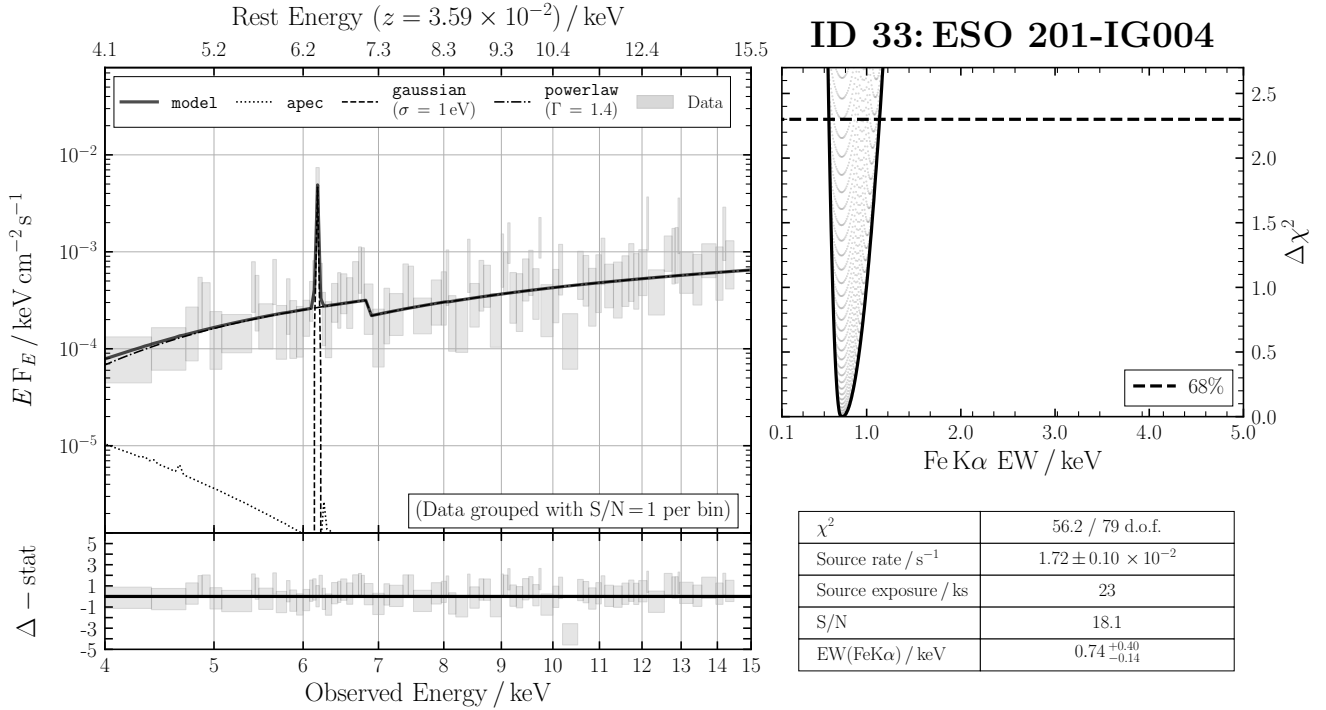
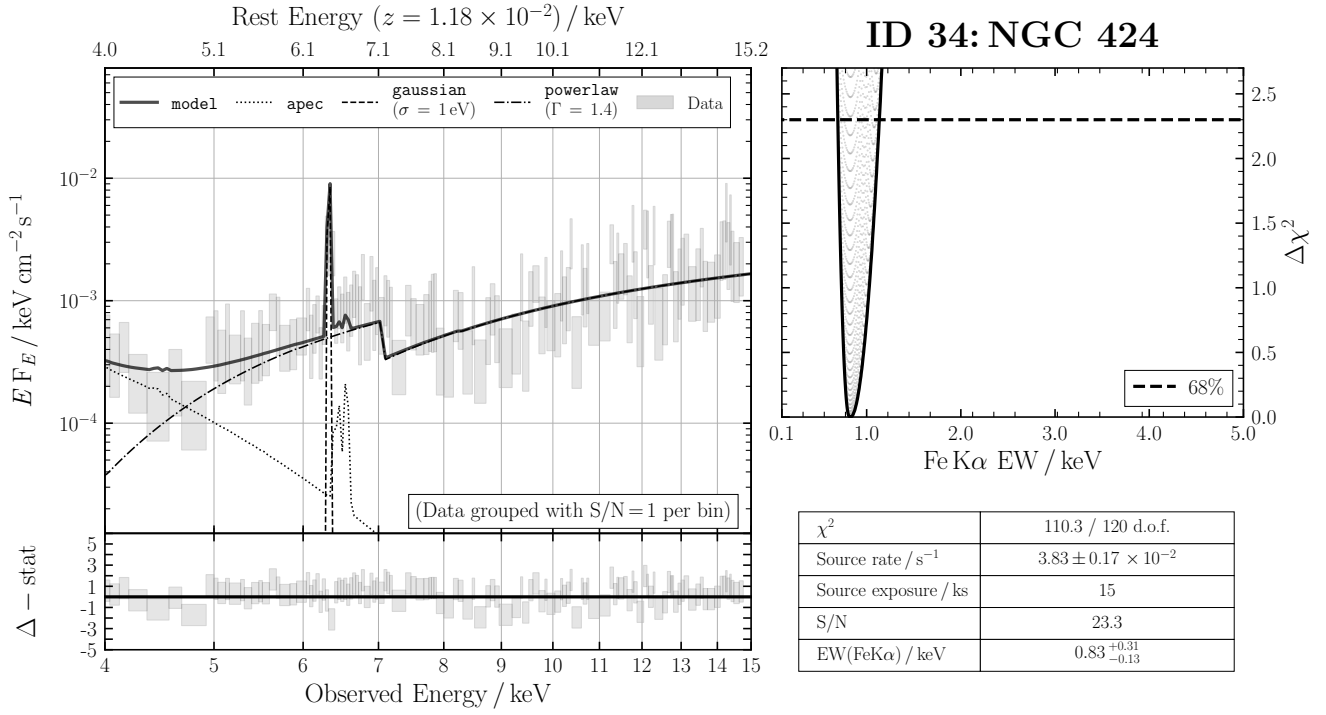
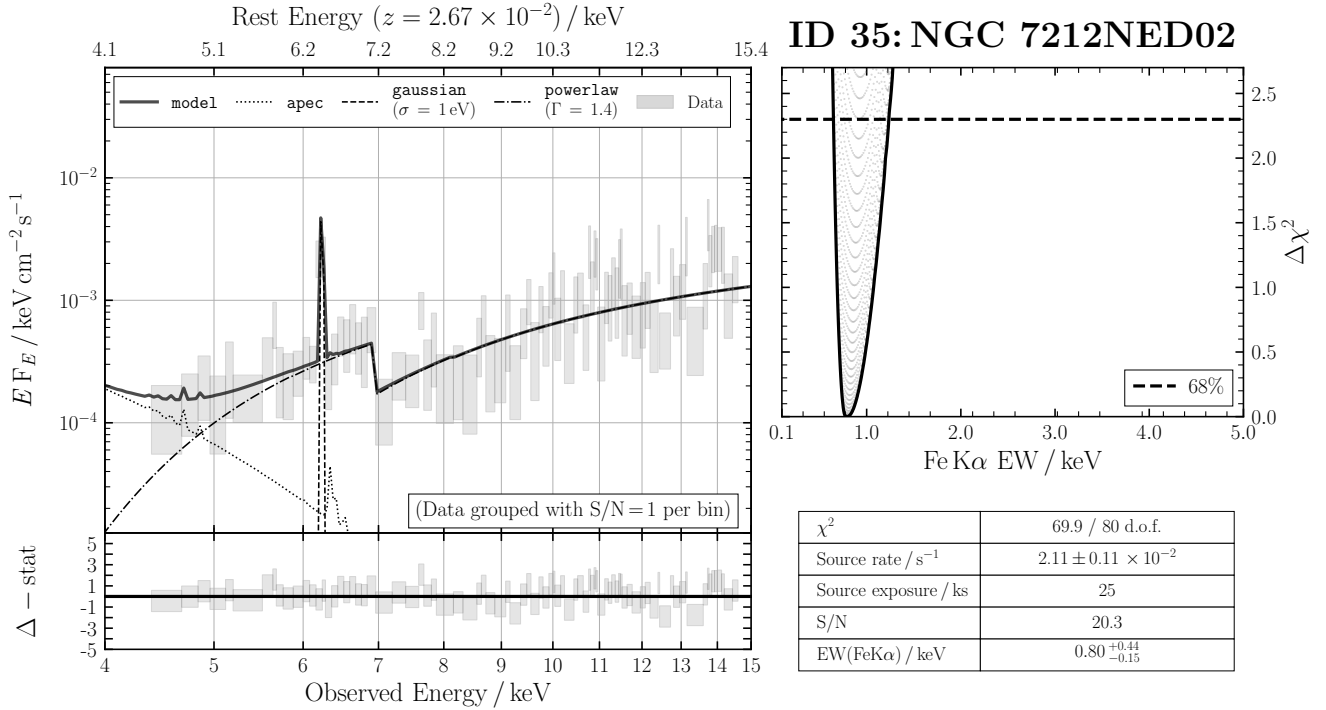


Figure B31. ID 33: ESO 201-IG004

**Figure B32.** ID 34: NGC 424**Figure B33.** ID 35: NGC 7212NED02

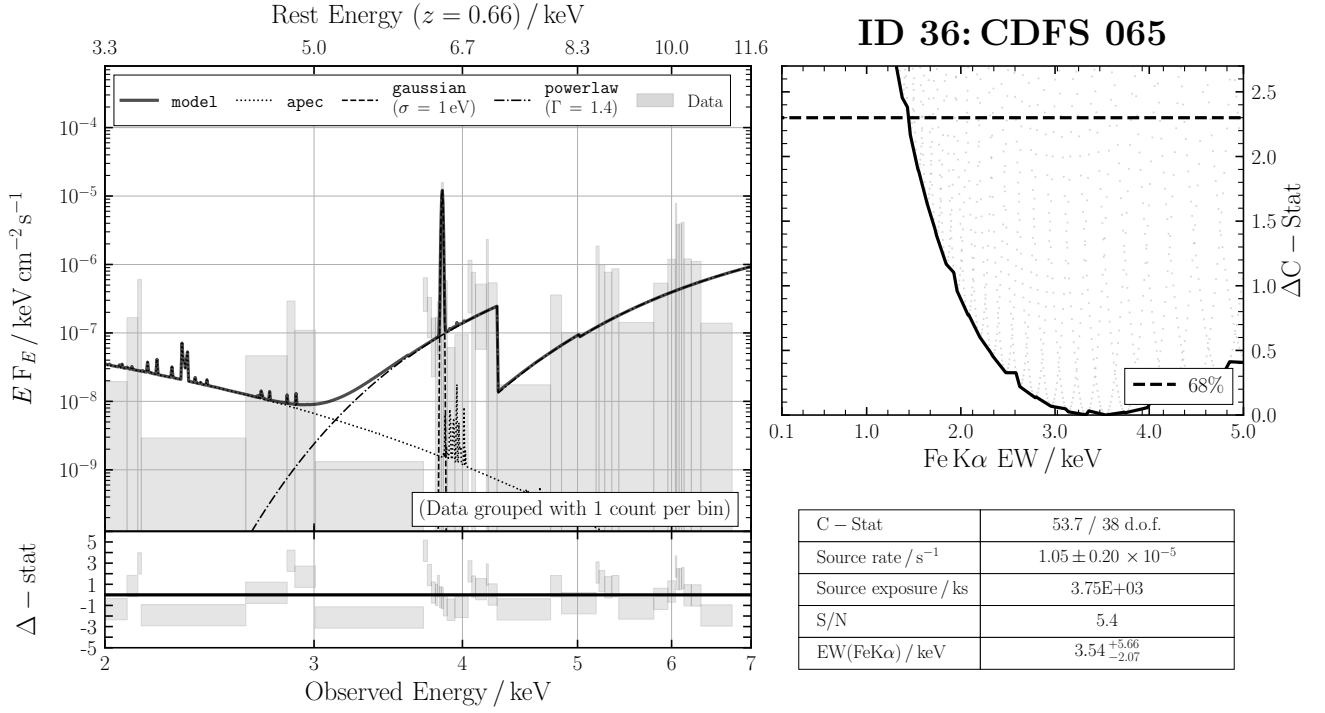


Figure B34. ID 36: CDFS 065

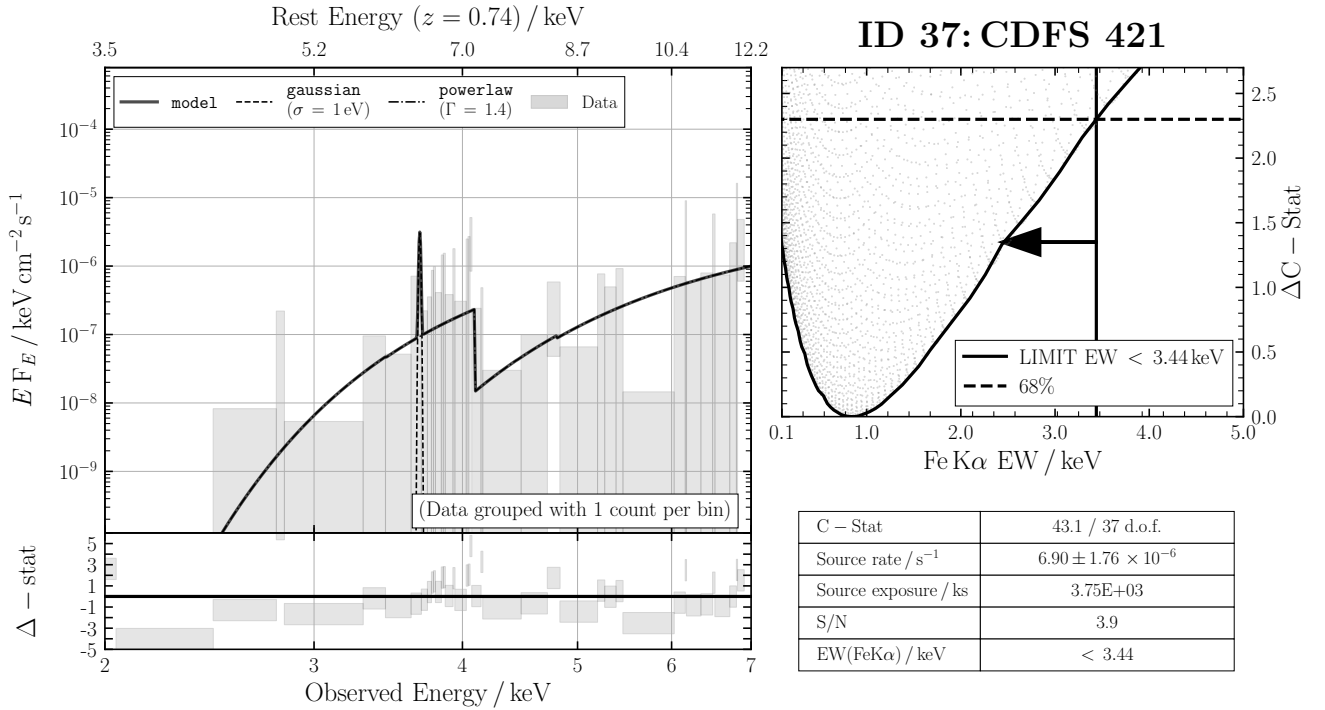
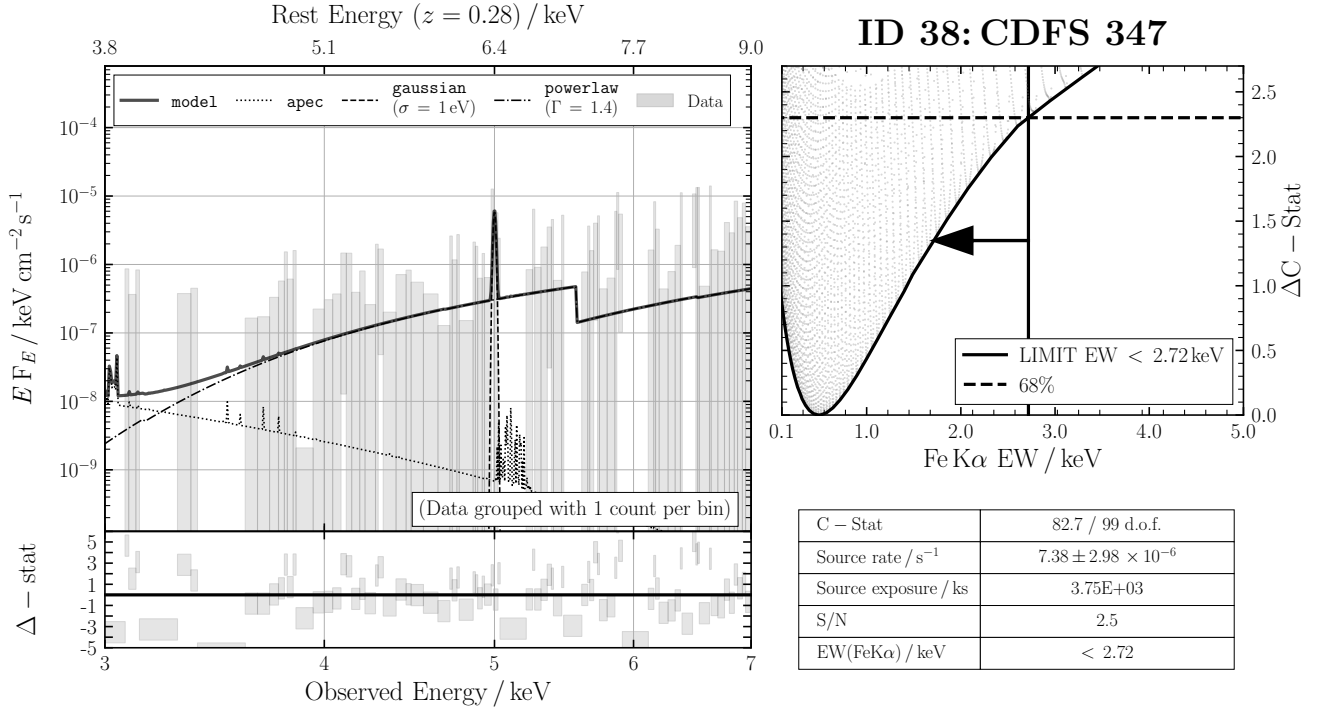
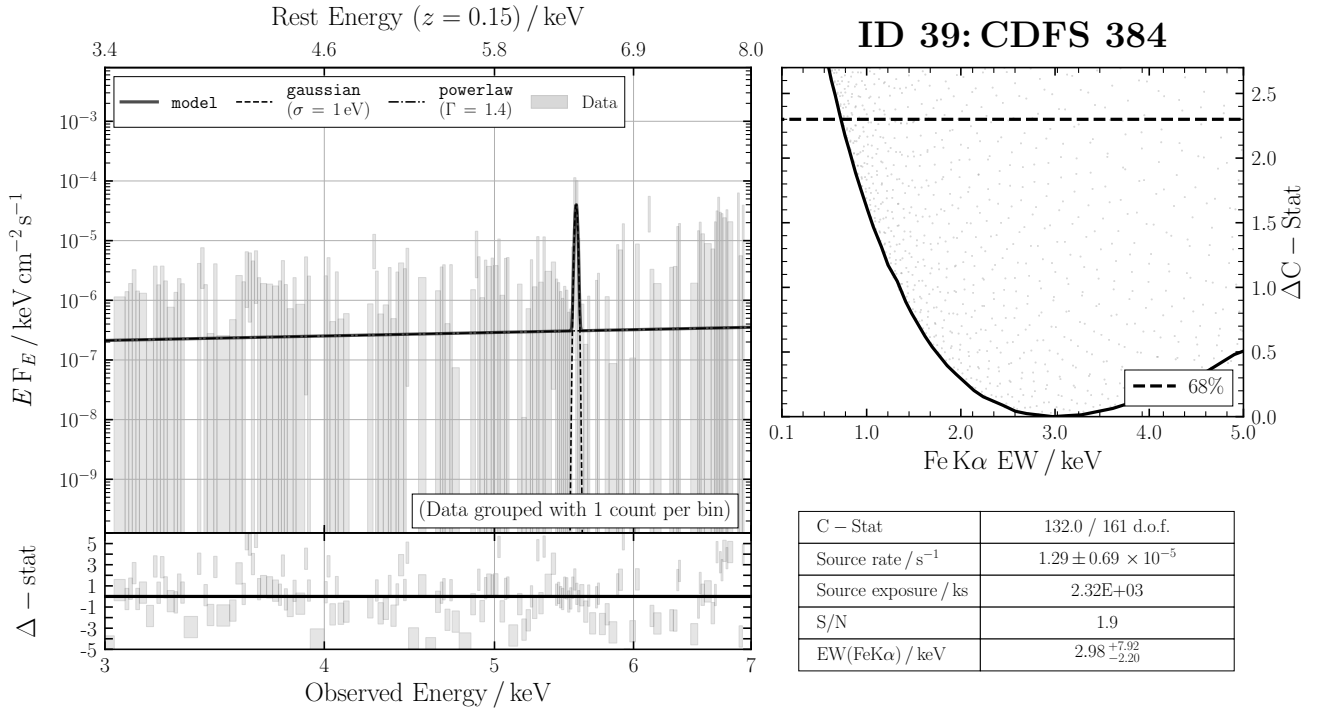


Figure B35. ID 37: CDFS 421

**Figure B36.** ID 38: CDFS 347**Figure B37.** ID 39: CDFS 384

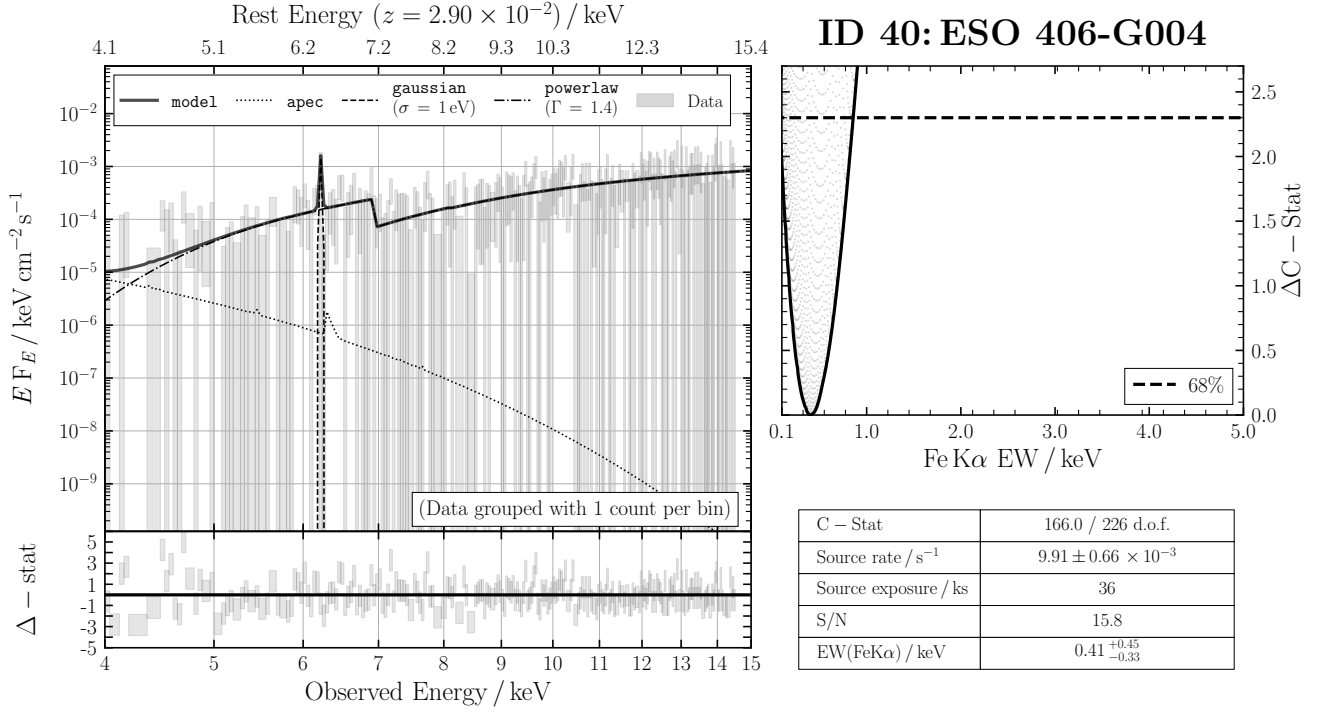


Figure B38. ID 40: ESO 406-G004

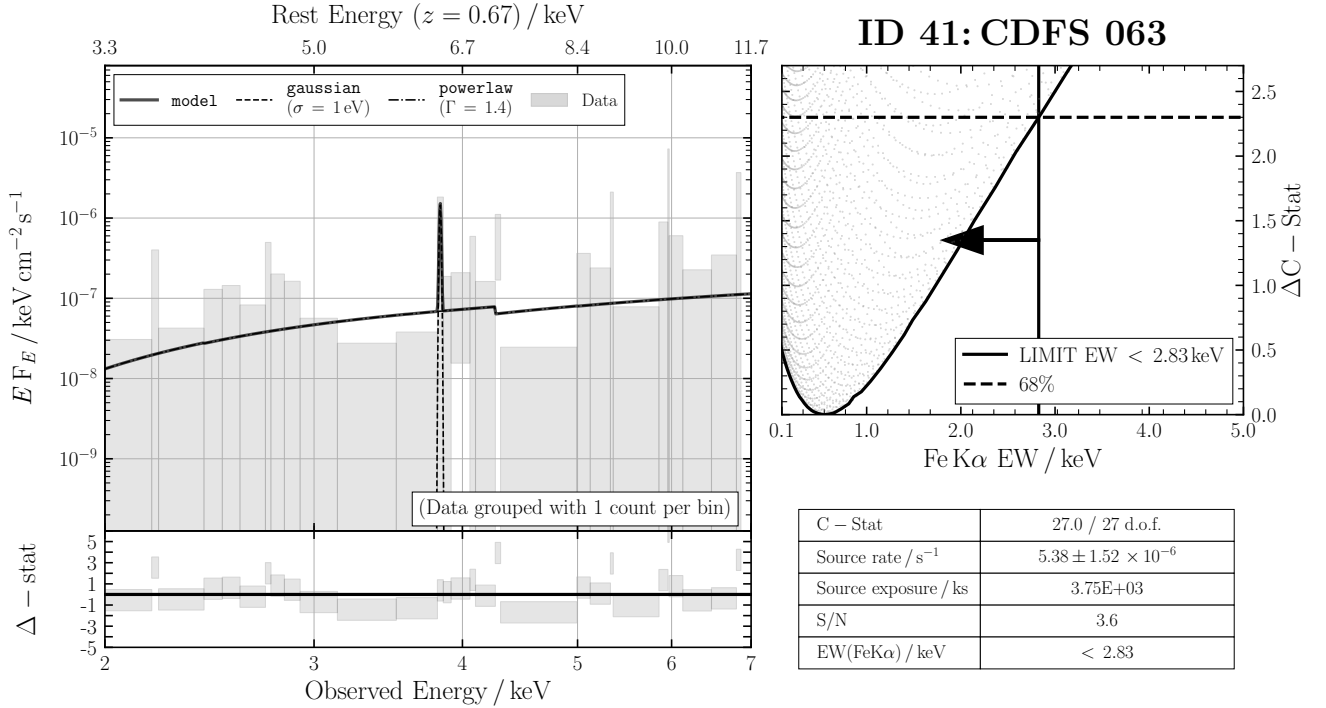
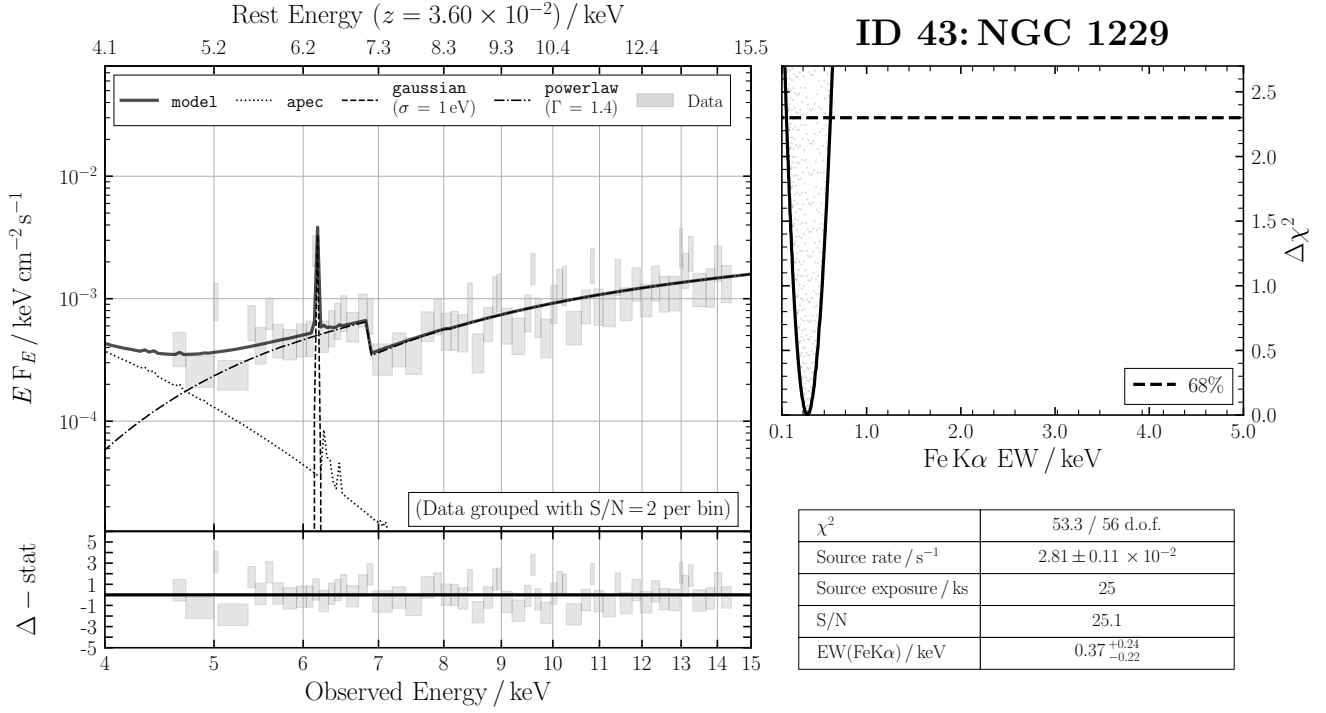
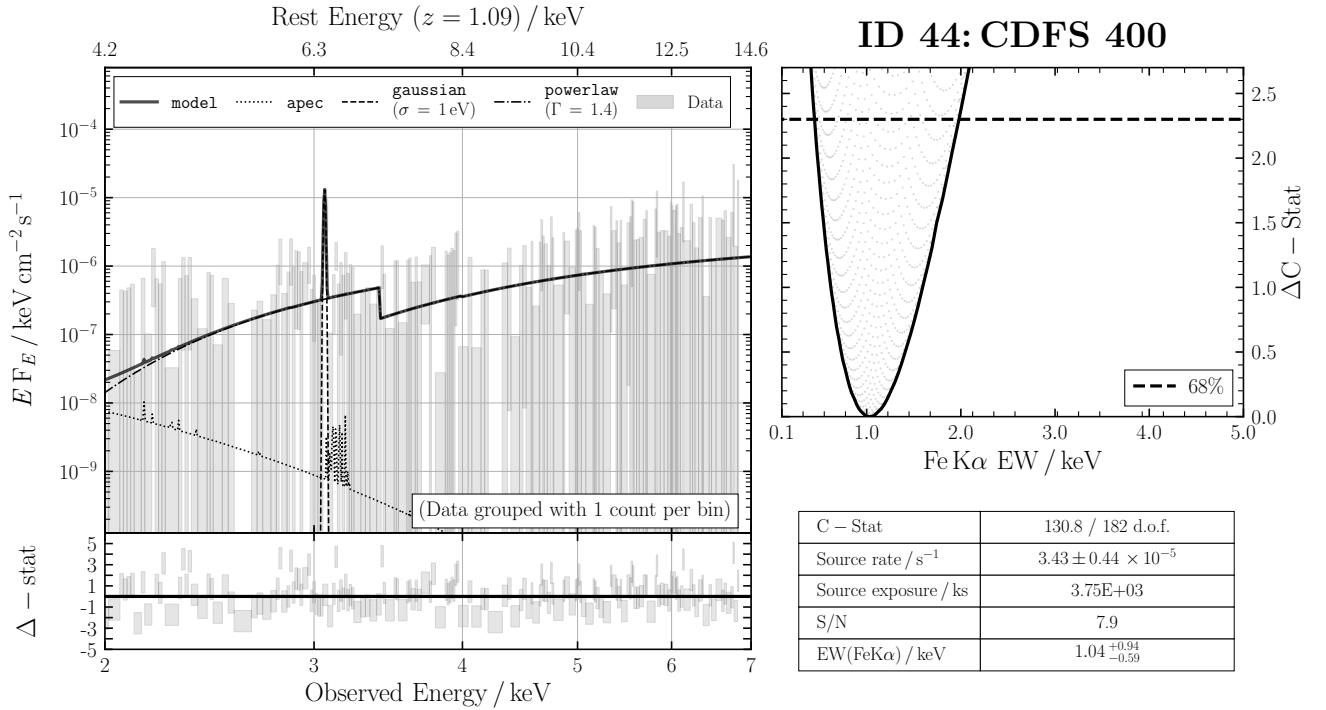


Figure B39. ID 41: CDFS 063

**Figure B40.** ID 43: NGC 1229**Figure B41.** ID 44: CDFS 400

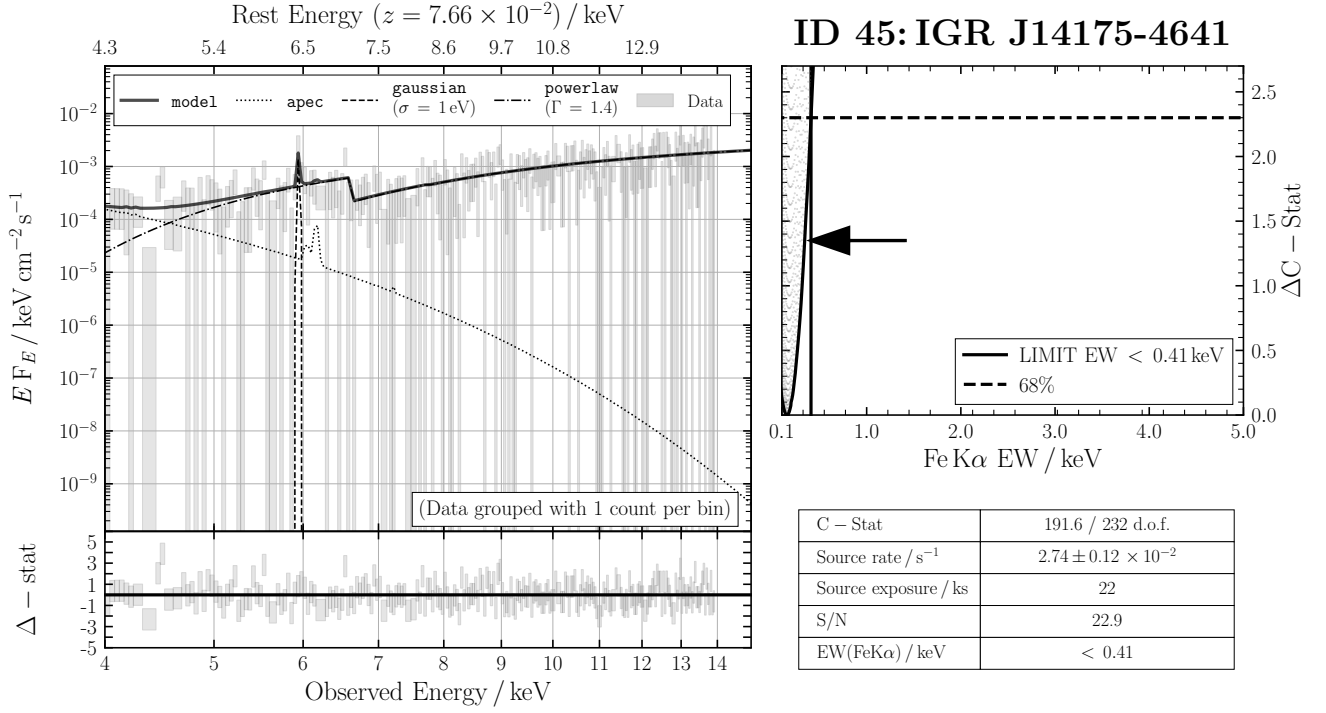


Figure B42. ID 45: IGR J14175-4641

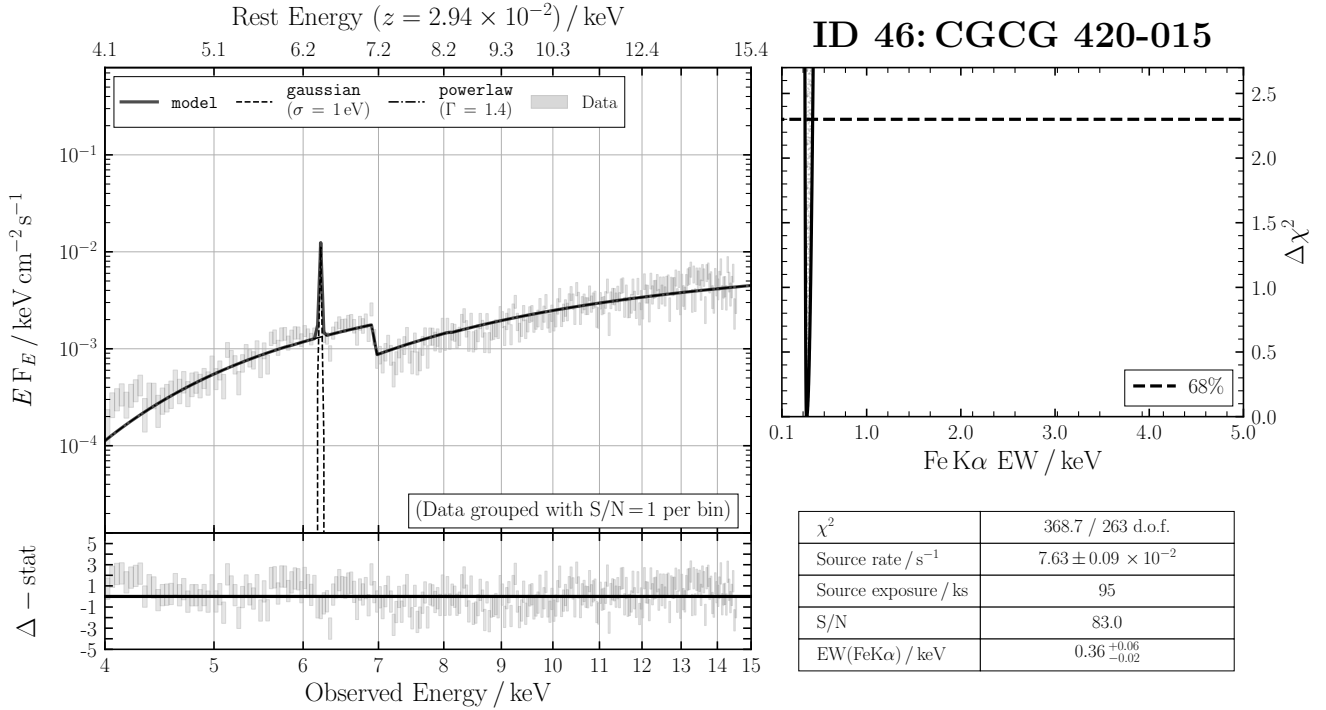
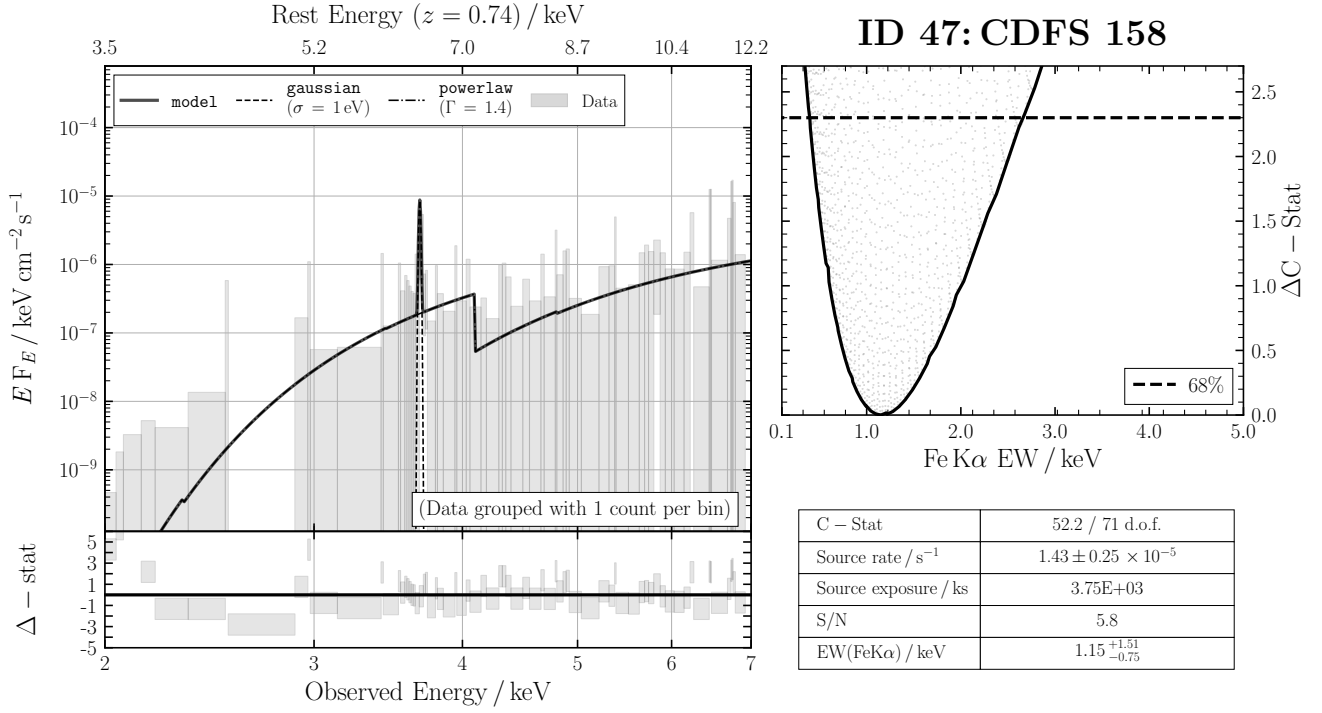
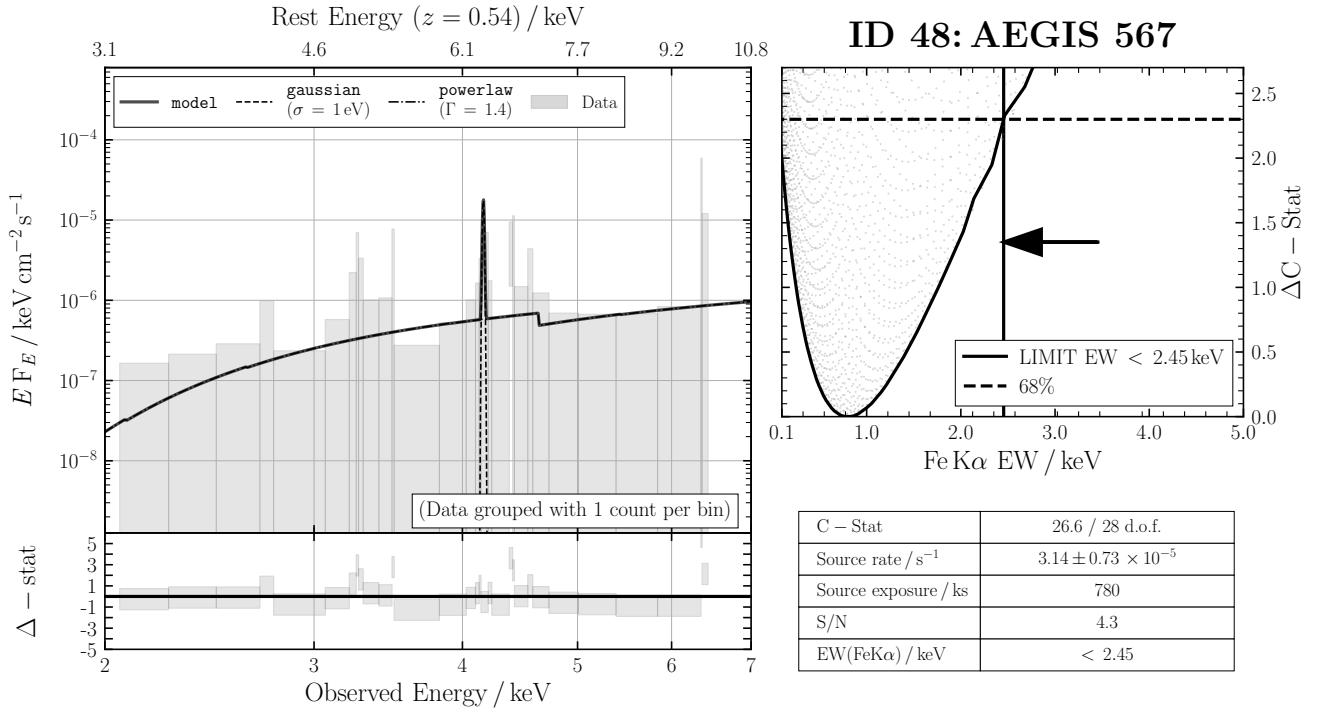


Figure B43. ID 46: CGCG 420-015

**Figure B44.** ID 47: CDFS 158**Figure B45.** ID 48: AEGIS 567

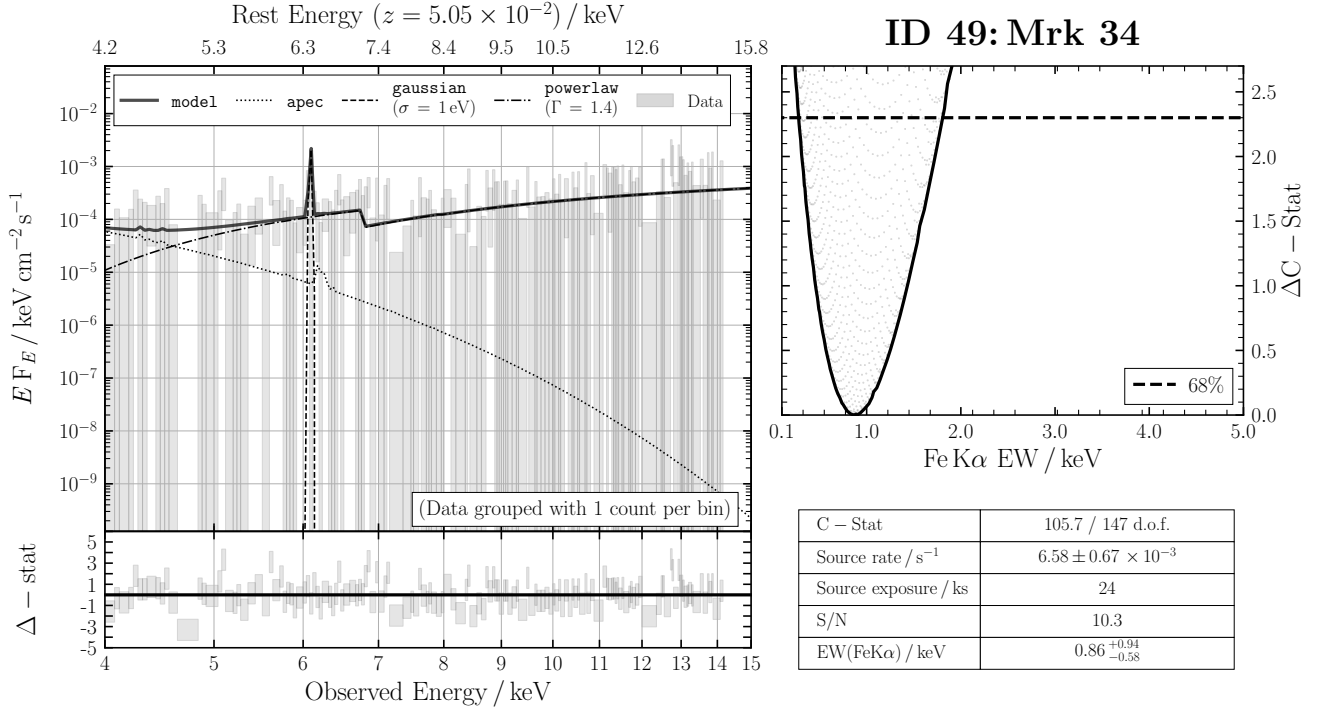


Figure B46. ID 49: Mrk 34

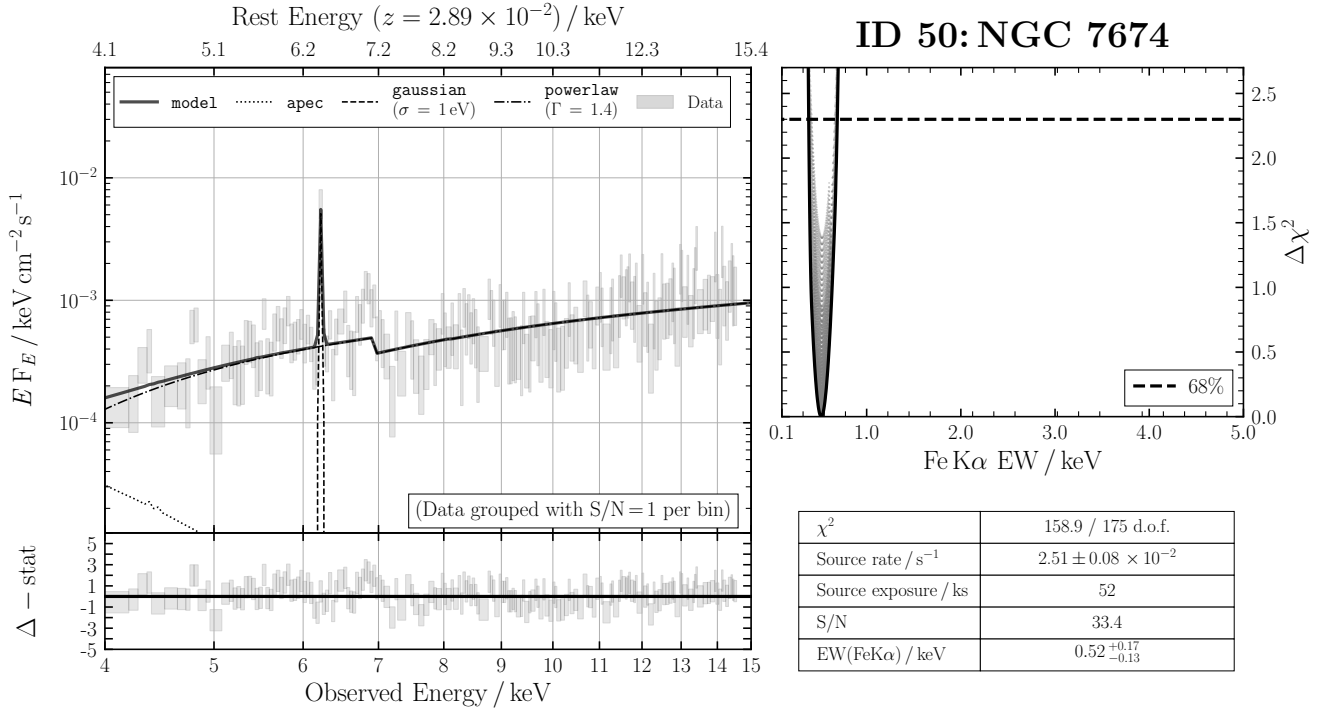
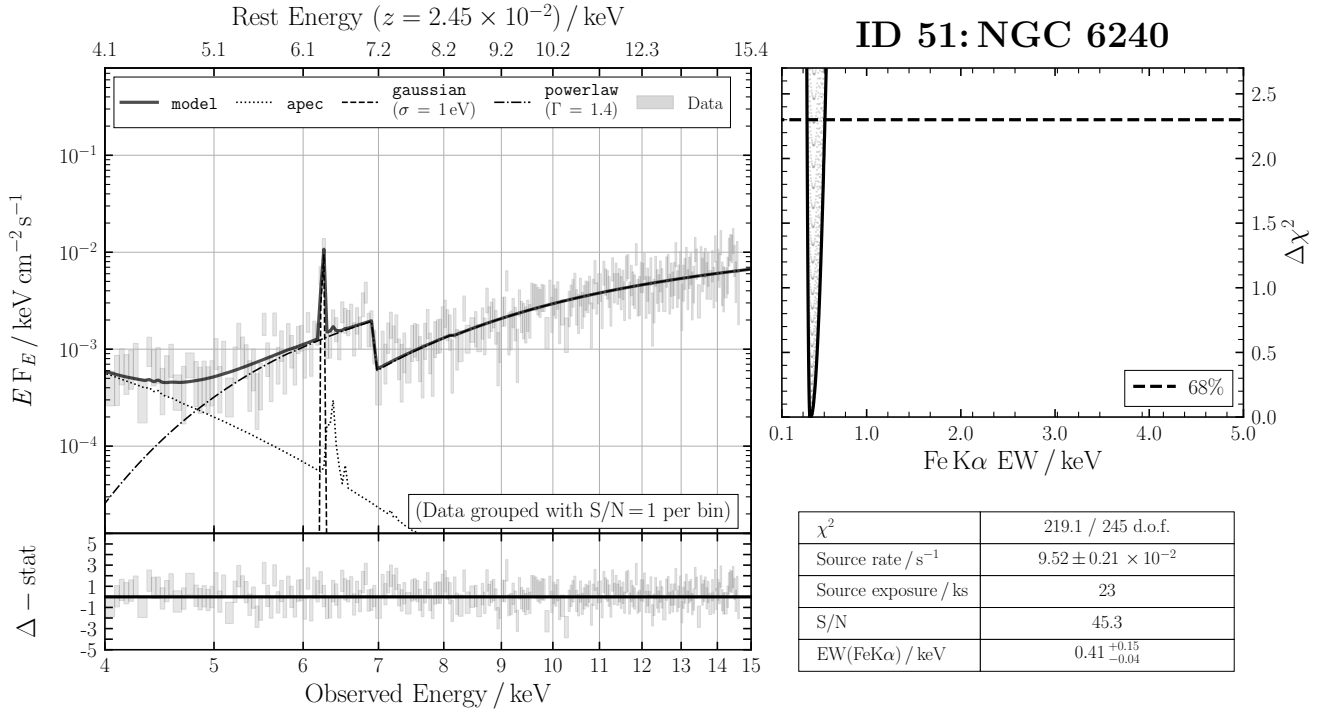
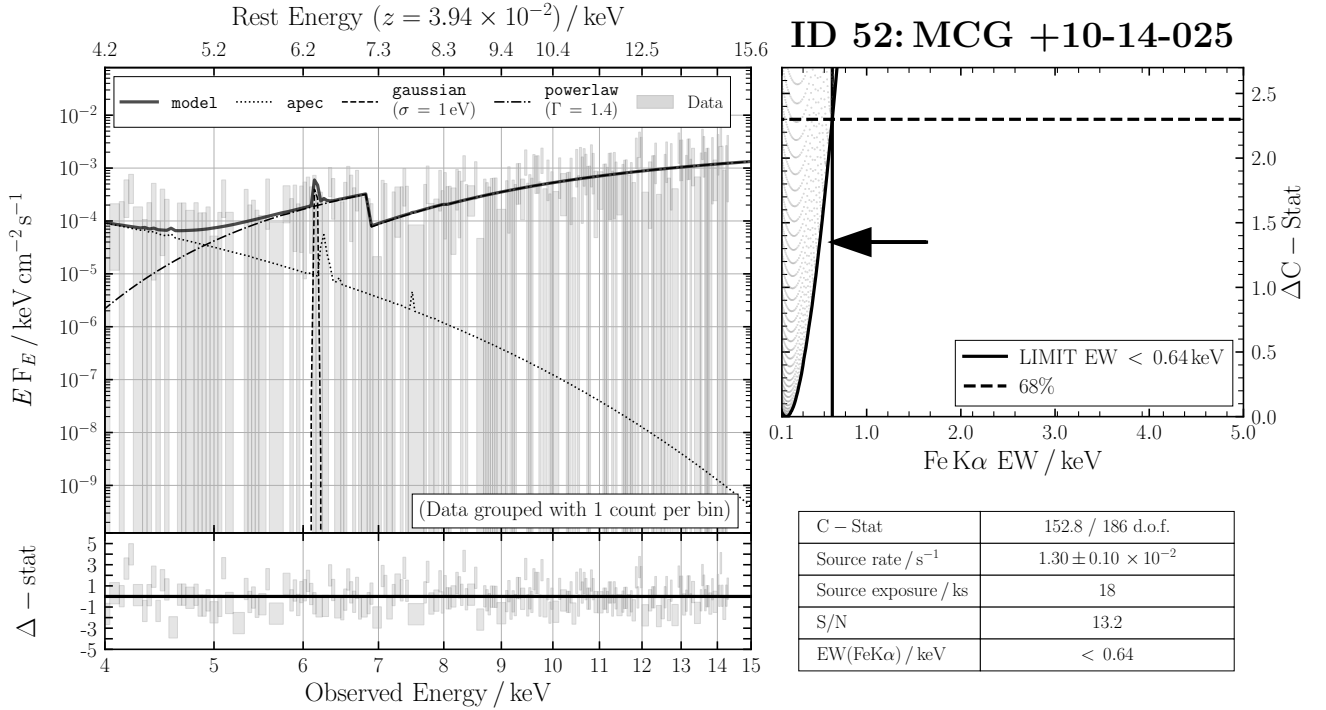


Figure B47. ID 50: NGC 7674

**Figure B48.** ID 51: NGC 6240**Figure B49.** ID 52: MCG +10-14-025

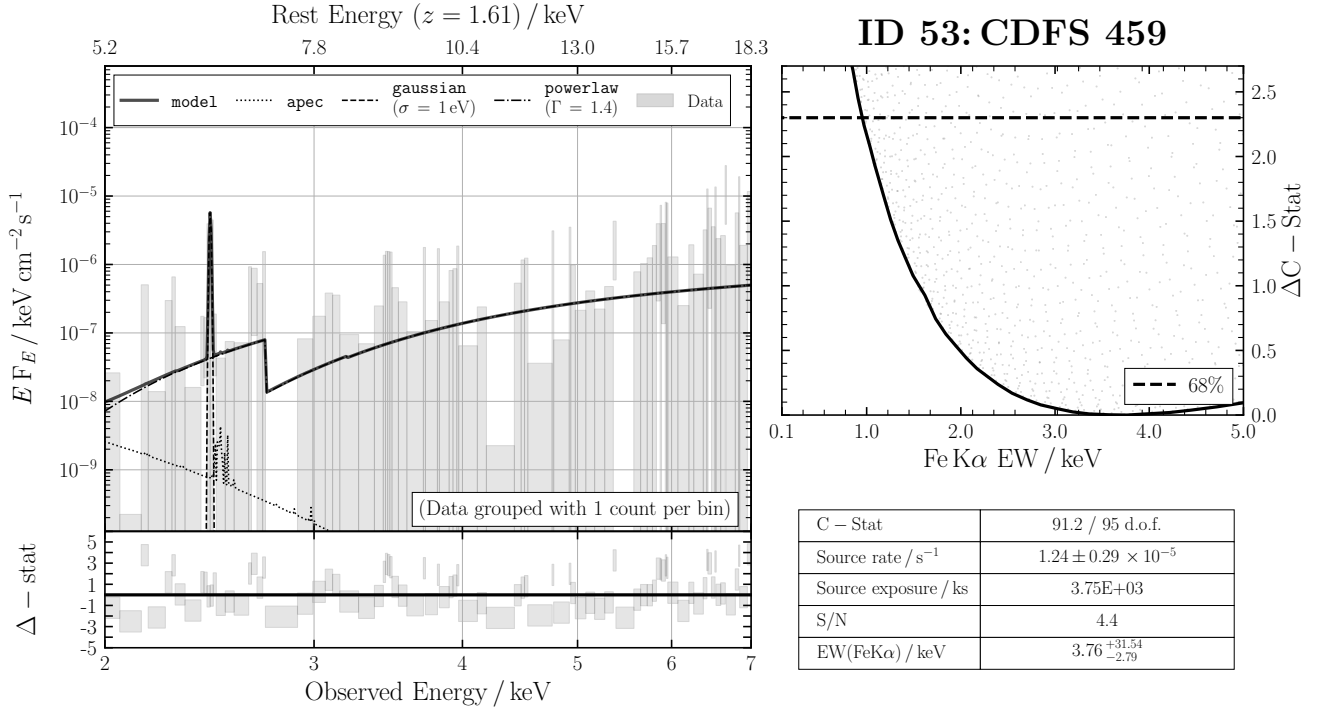


Figure B50. ID 53: CDFS 459

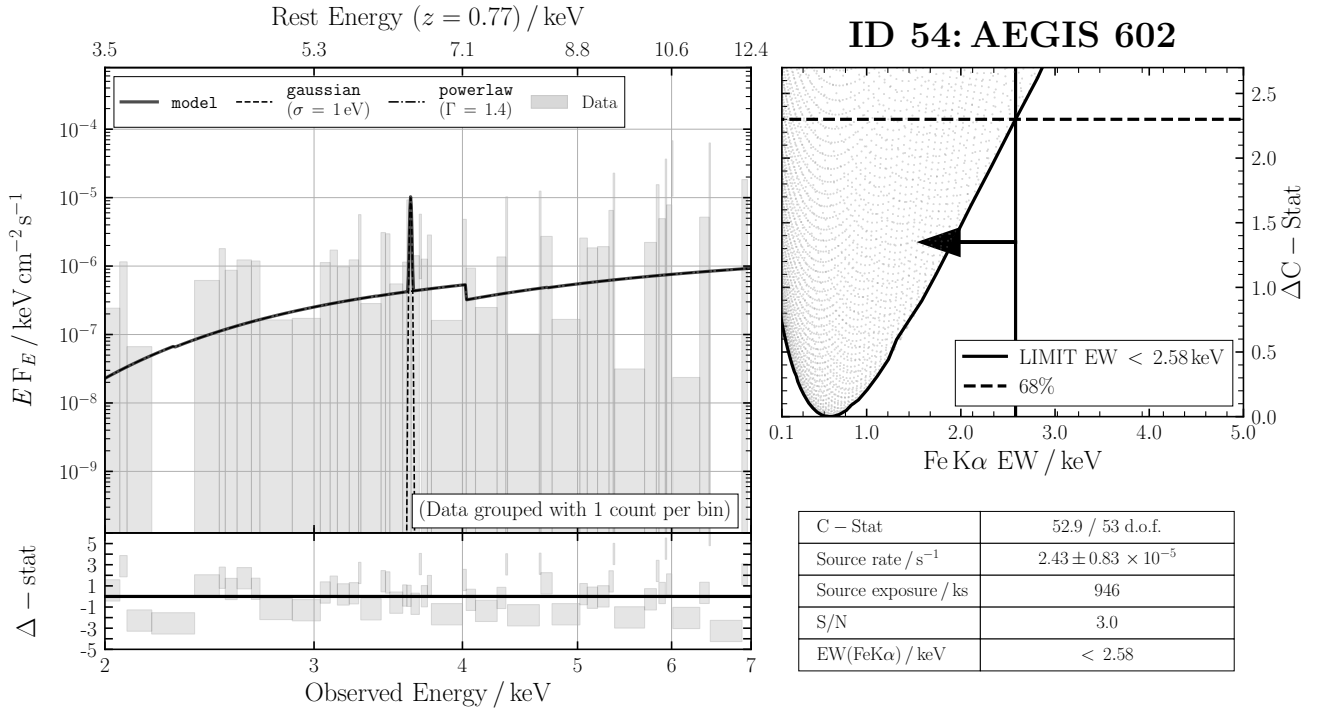
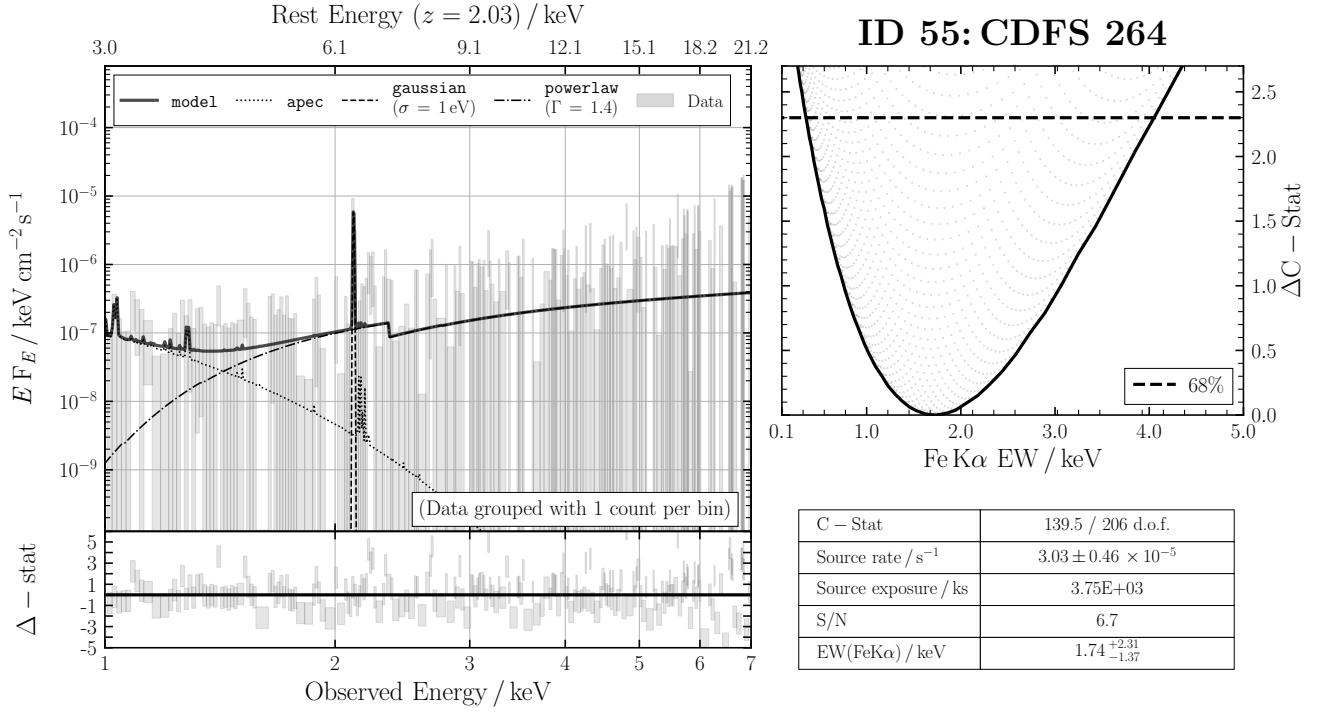
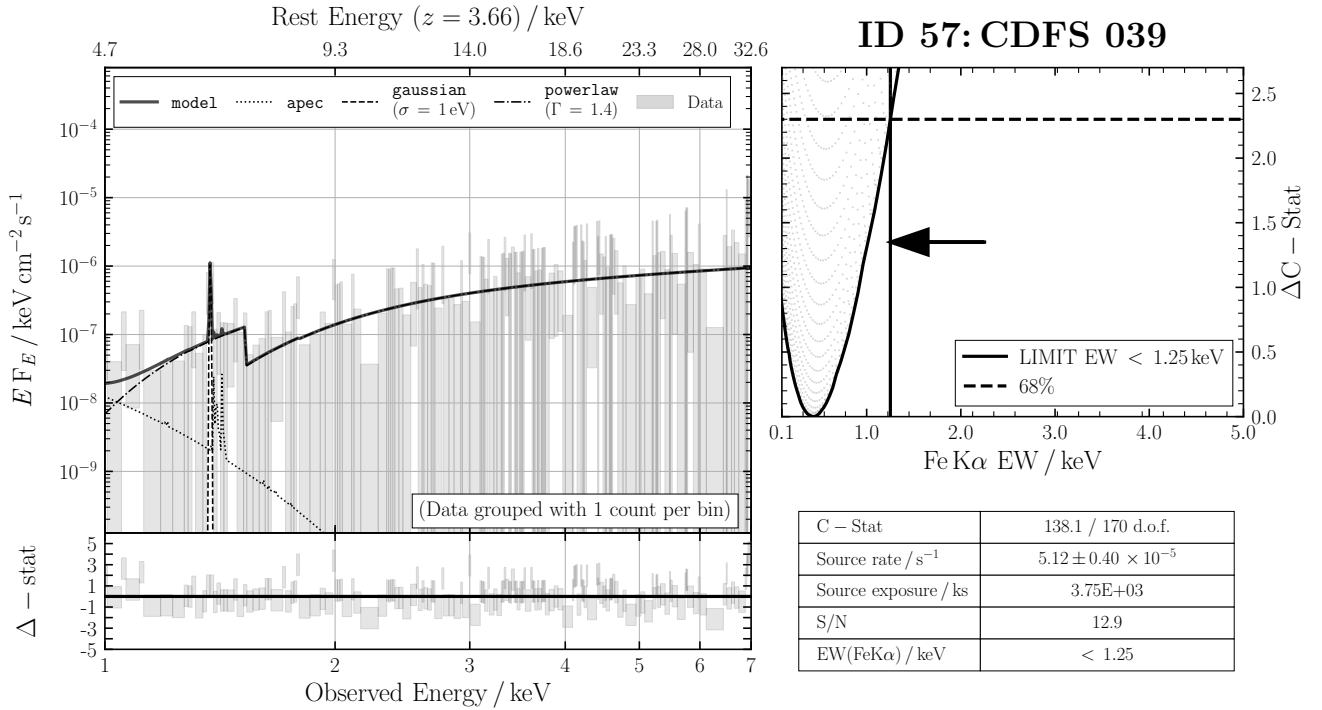


Figure B51. ID 54: AEGIS 602

**Figure B52.** ID 55: CDFS 264**Figure B53.** ID 57: CDFS 039

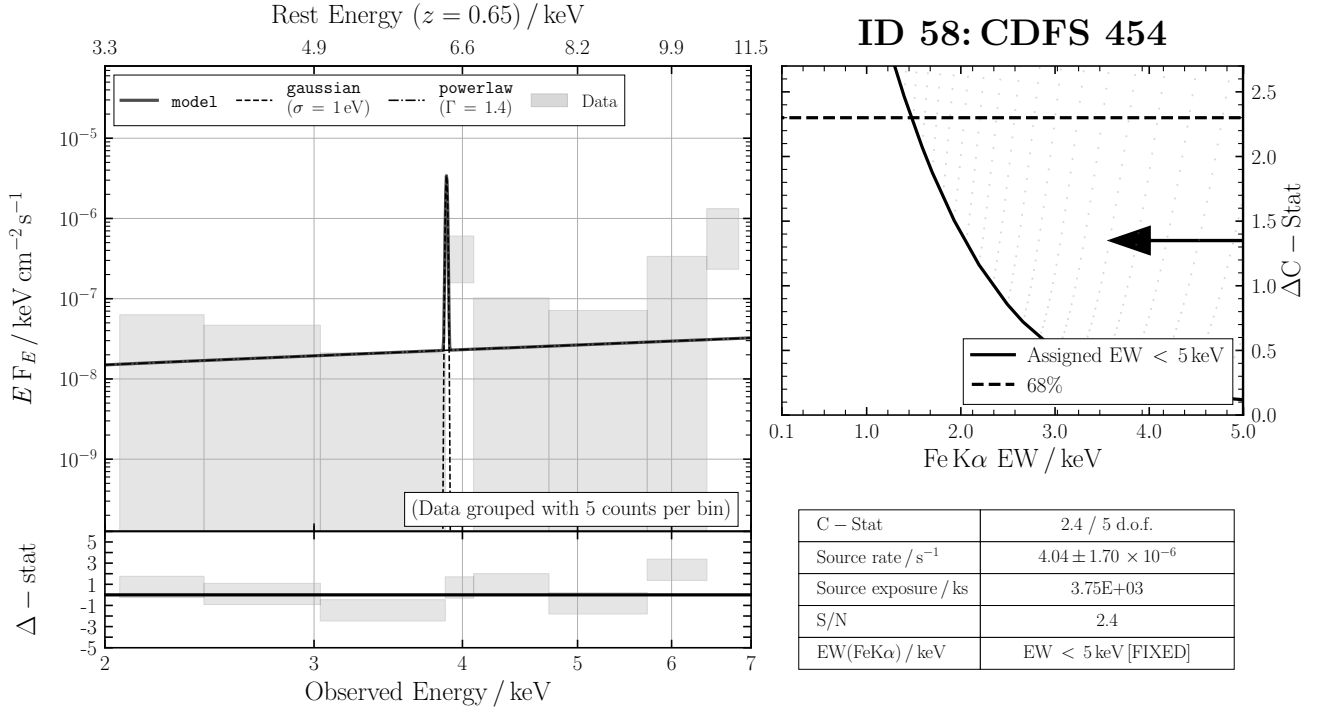


Figure B54. ID 58: CDFS 454

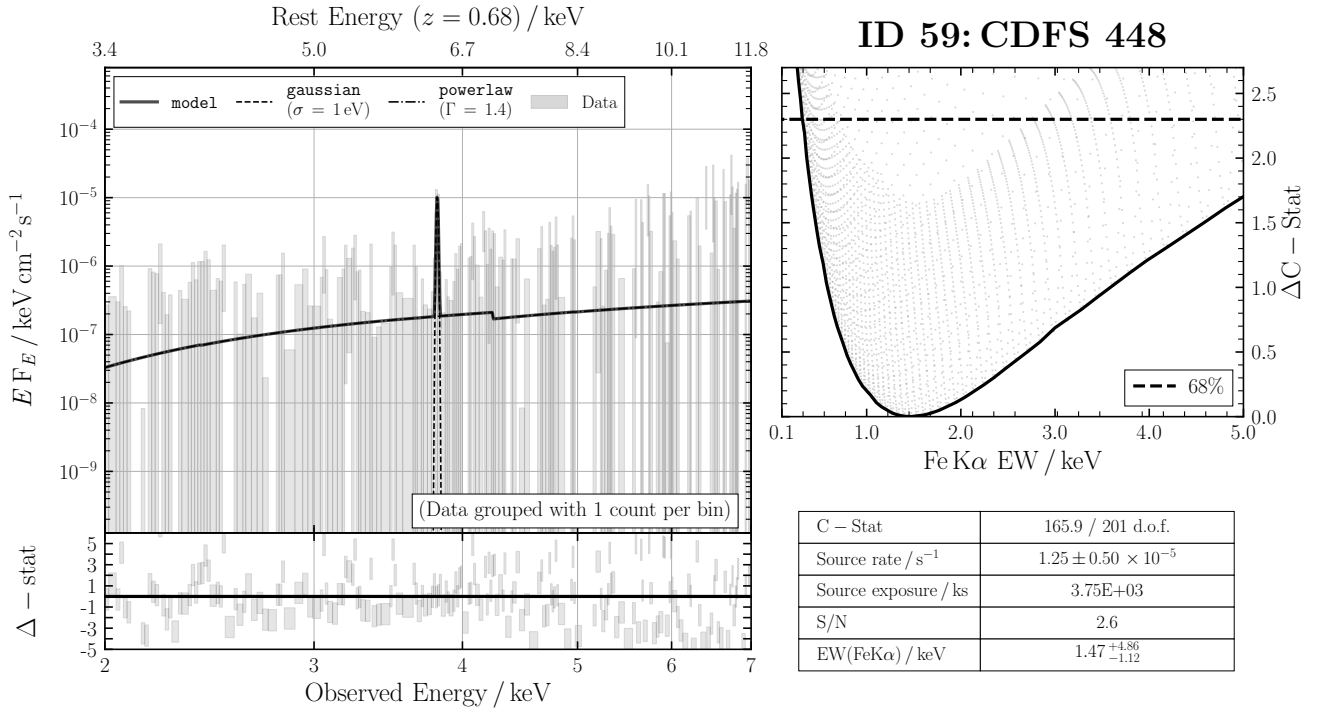
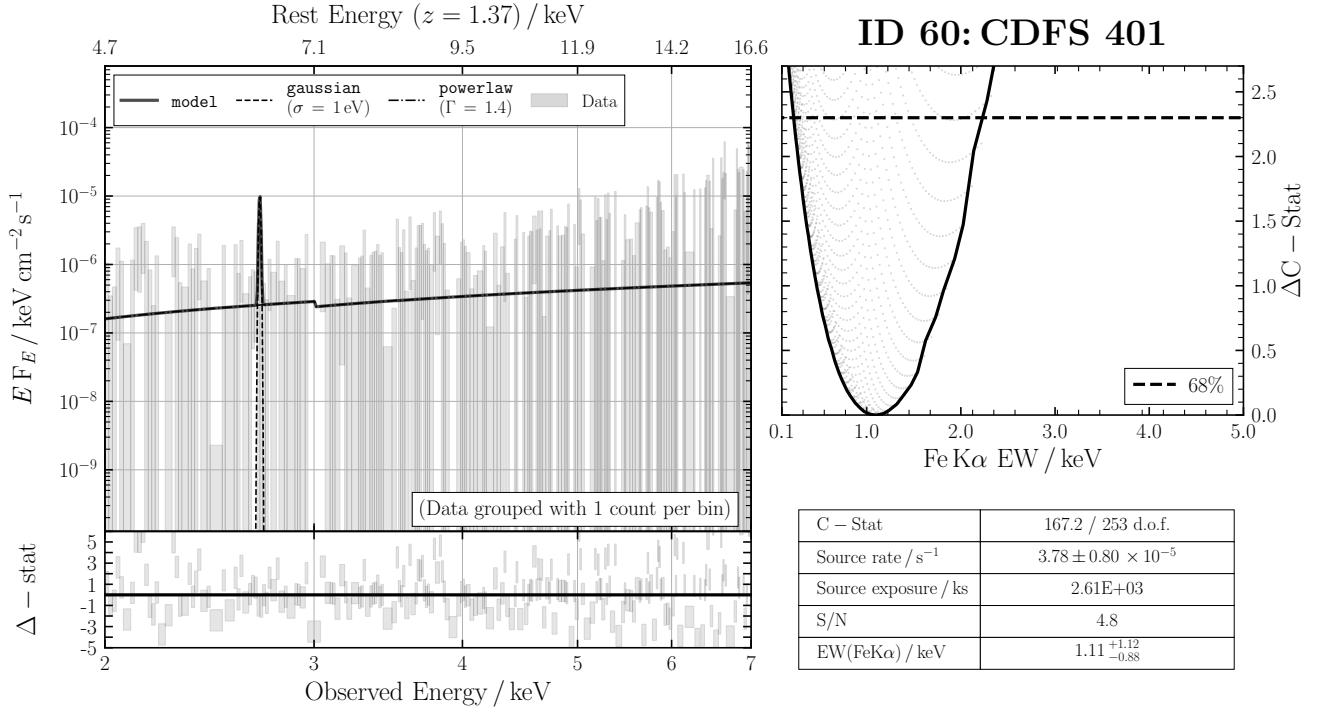
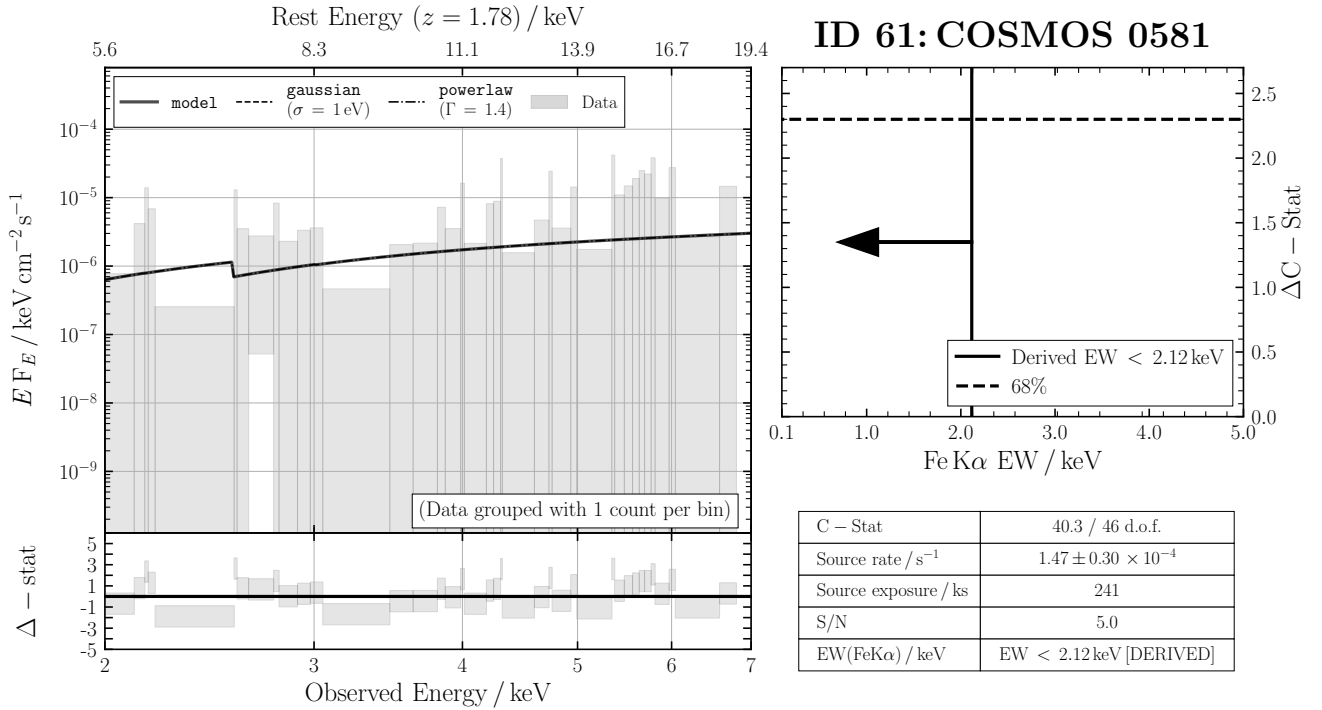


Figure B55. ID 59: CDFS 448

**Figure B56.** ID 60: CDFS 401**Figure B57.** ID 61: COSMOS 0581

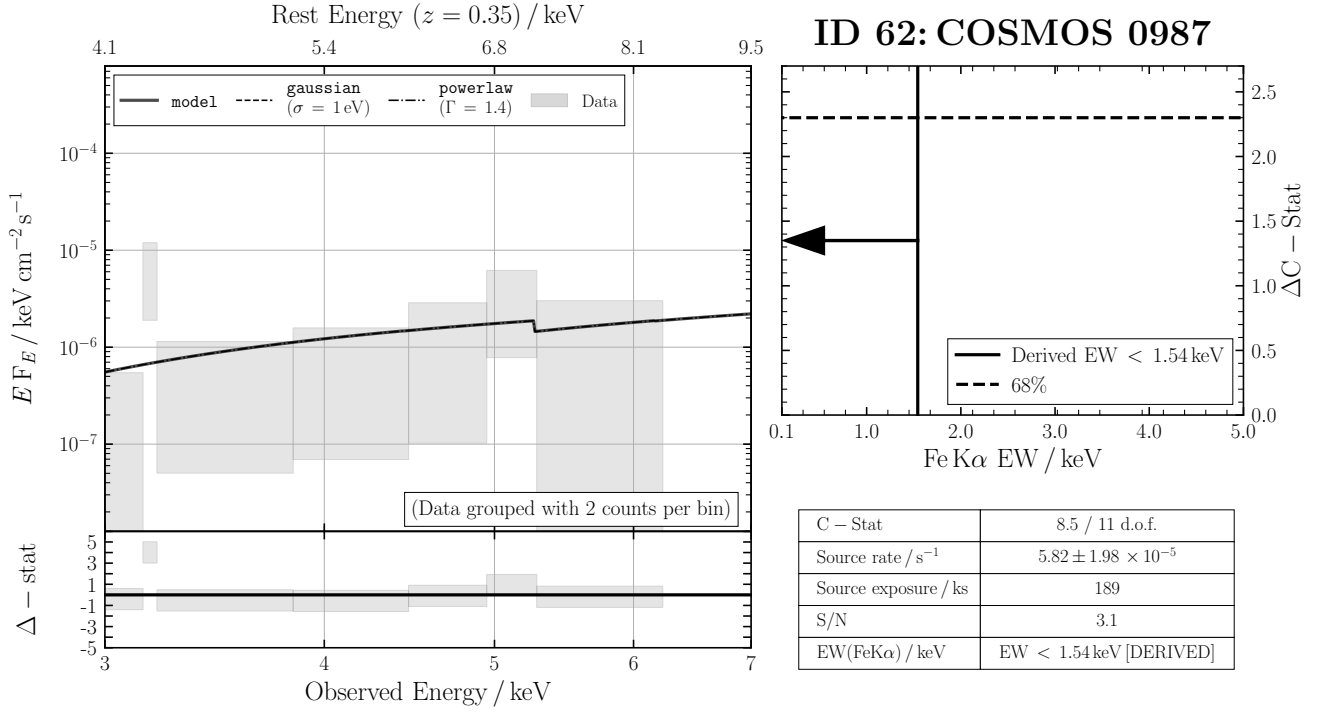


Figure B58. ID 62: COSMOS 0987

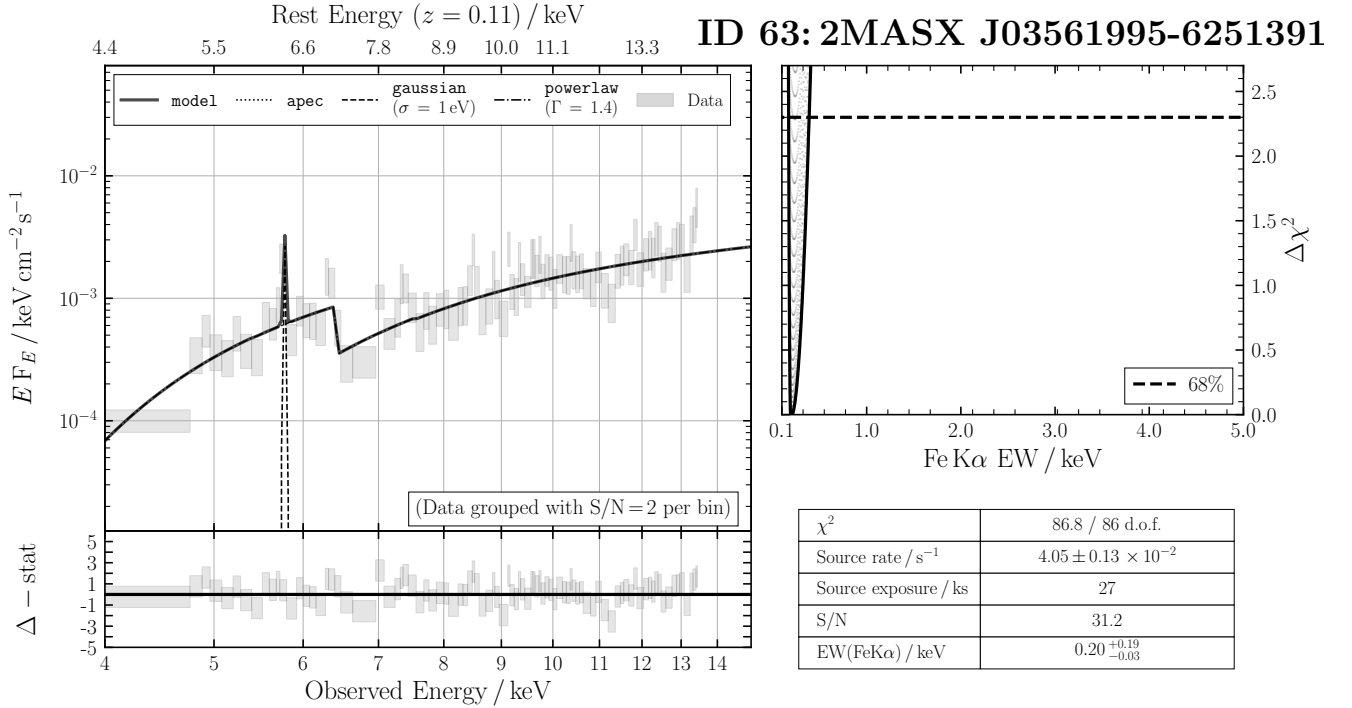
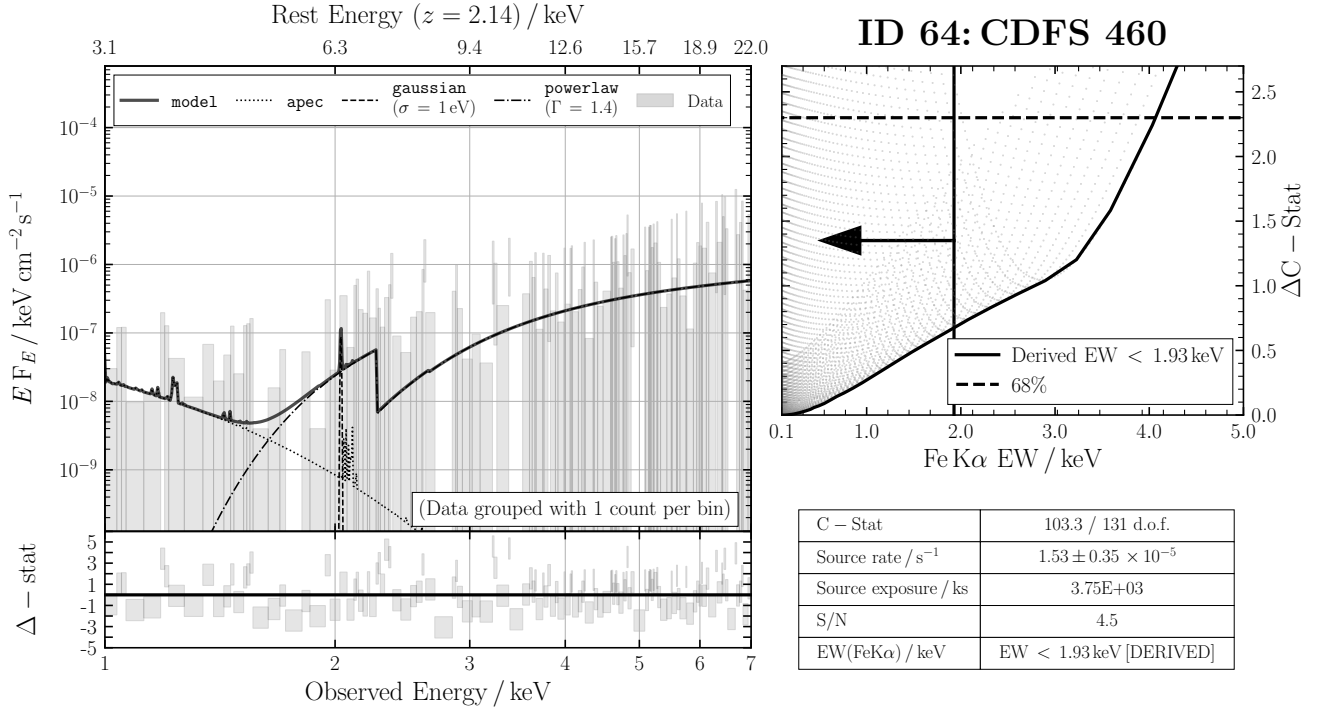
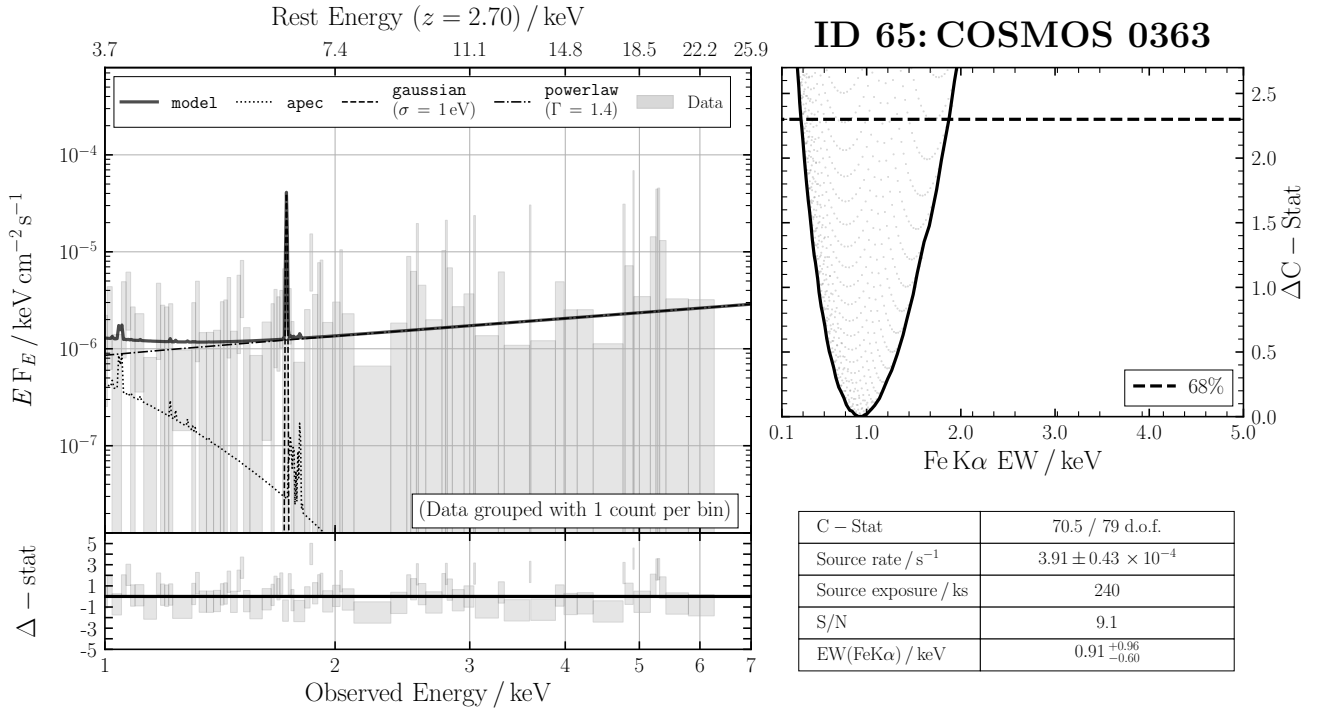


Figure B59. ID 63: 2MASX J03561995-6251391

**Figure B60.** ID 64: CDFS 460**Figure B61.** ID 65: COSMOS 0363

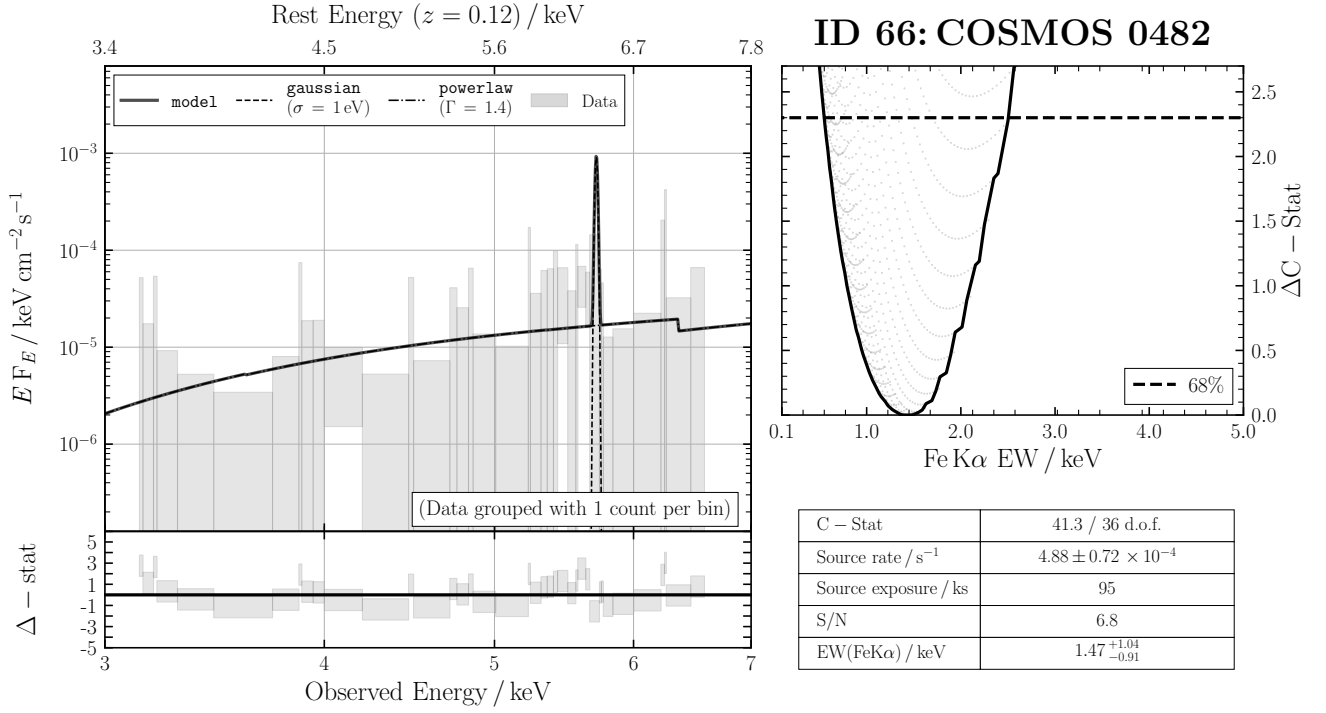


Figure B62. ID 66: COSMOS 0482

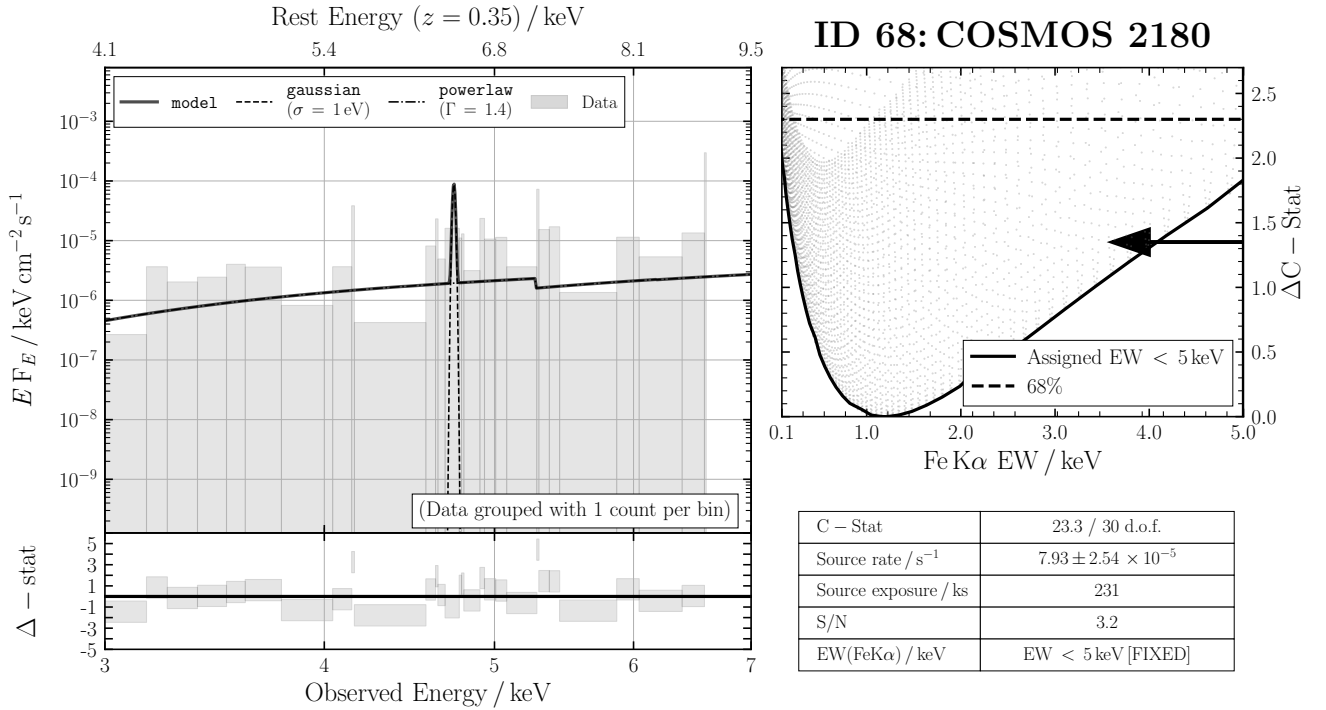
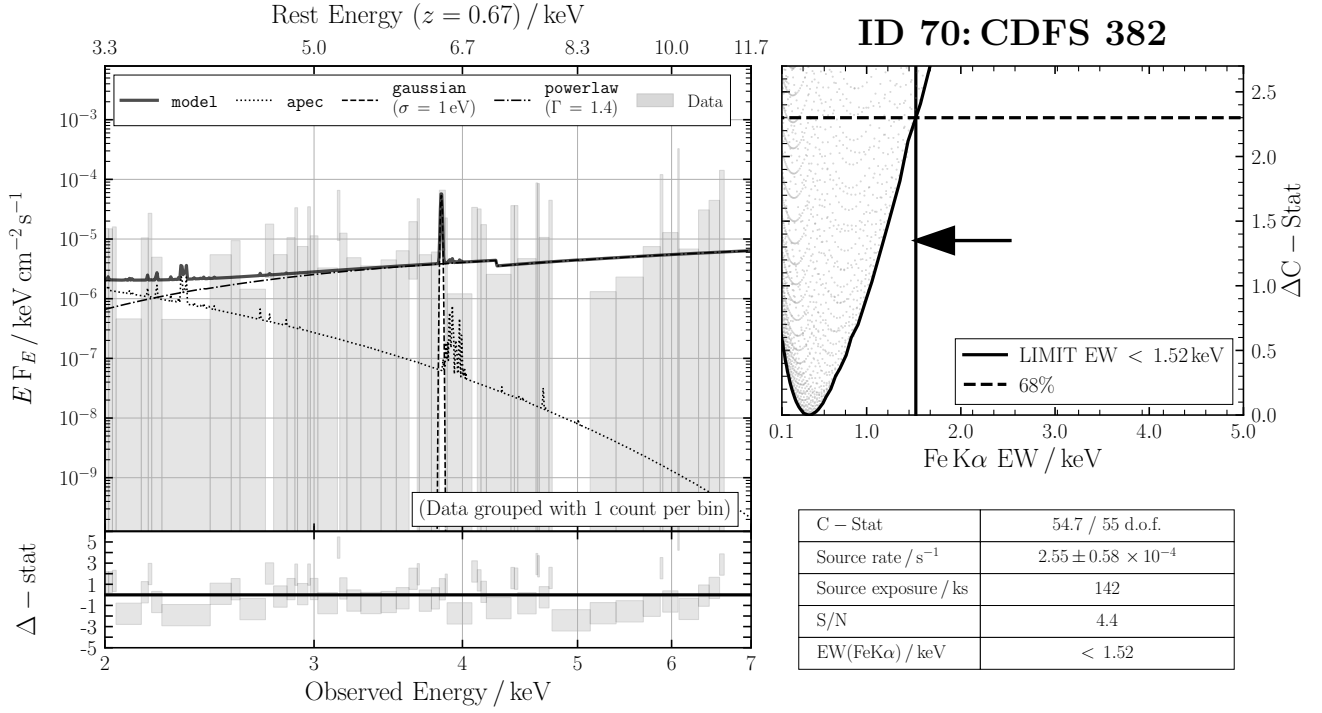
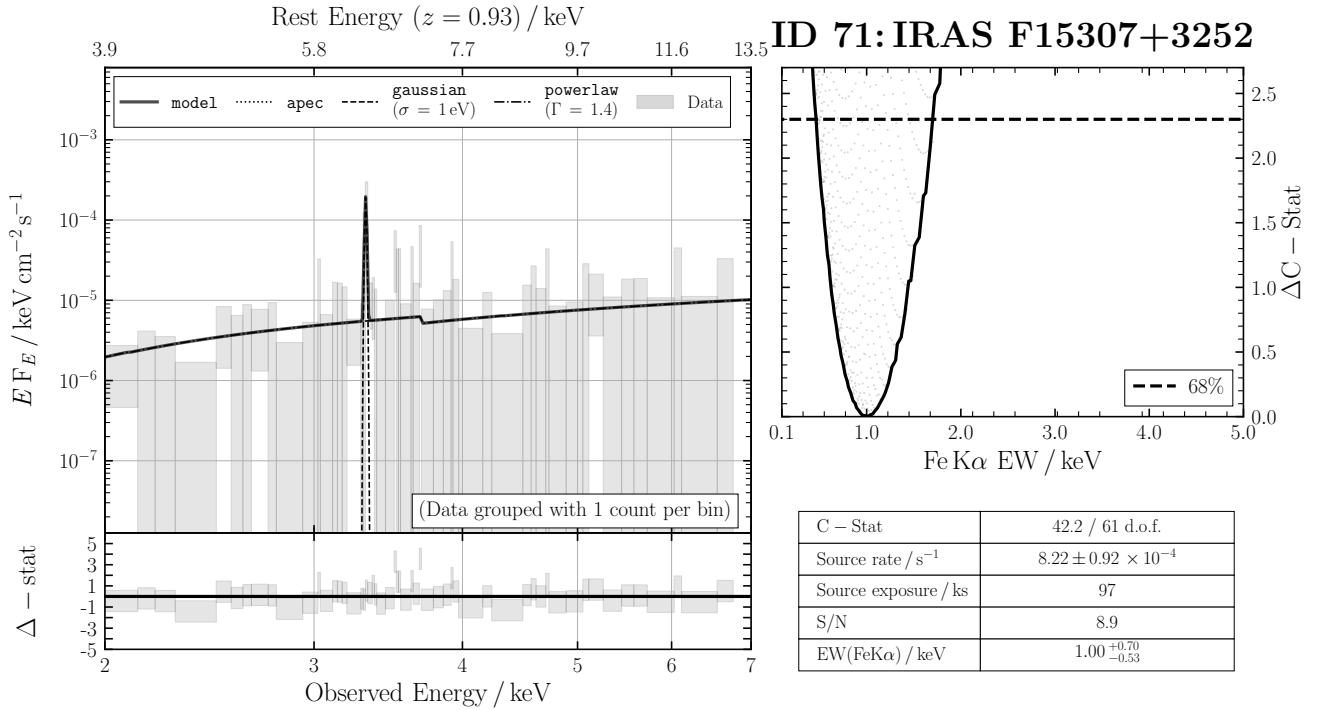


Figure B63. ID 68: COSMOS 2180

**Figure B64.** ID 70: CDFS 382**Figure B65.** ID 71: IRAS F15307+3252